Airfoil Boundary-Layer Control through Pulsating Jets

Vom Fachbereich Maschinenbau
an der Technischen Universität Darmstadt
zur
Erlangung des Grades eines Doktor-Ingenieurs (Dr.-Ing.)
genehmigte

D i s s e r t a t i o n

vorgelegt von

M. Sc. Álvaro Pereira Coppieters

aus São Paulo, Brasilien

Berichterstatter:	Prof. Dr.-Ing. B. Stoffel
Mitberichterstatter:	Prof. Dr.-Ing. C. Tropea
Tag der Einreichung:	03.05.2010
Tag der Mündlichen Prüfung:	16.06.2010

Darmstadt 2011
D 17

Hiermit versichere ich, die vorliegende Doktorarbeit unter der Betreuung von Prof. Dr.-Ing. B. Stoffel nur mit den angegebenen Hilfsmitteln selbstaendig angefertigt zu haben.

Álvaro Pereira Coppieters Darmstadt, den 18.04.2010

Acknowledgment

I would like to thank the people that have been involved in making this work possible.
My parents, Isabel and Percival who gave me the motivation to go for things in life I think have to be done. My wife Alice, who have been always on my side and gave me the support I needed along this way.
My advisor Professor Dr.-Ing. Bernd Stoffel, for giving me this opportunity. His motivation and patience have proved invaluable in helping me complete this work. I would like to mention Mr. B. Matyschok and Professor Dr.-Ing. P. Peltz from FST and Mrs. S. Wallner for her goodwill. I would also like to thank Mr. U. Trometer and Mr. A. Schuler from the workshop, whose ability permited to implement the concepts developed during this work.
My friends at TU-Darmstadt, Michael Heß, Kai-Henning Brune, Sven Koenig, Pascal Schuler, Matthias Puff, Nuri Hamadeh, Valérie Bischof, Christian Müller and Anandarajah Mariadas.
Lastly, the support of the CAPES (Brazil) for the scholarship.

This achievement is dedicated to my wife Alice and our children André and Ana Júlia.

Contents

Nomenclature

Symbols

A	m^2	projection of an area in a plane paralel to the flow
b	m	width of slot for air injection
c	m	airfoil chord or general body characteristic length
C_μ	-	momentum coefficient
c_μ	-	steady component of C_μ
c'_μ	-	unsteady component of C_μ
C_D	-	drag coefficient
C_f	-	skin friction coefficient
C_L	-	lift coefficient
C_p	-	pressure coefficient
d	mm	distance from slot to trailing edge
F_D	N	total drag force
f	Hz	frequency
f^+	-	non-dimensional actuation frequency
f_c	-	characteristic frequency
H	-	shape factor
l	mm	slot length
Ma	-	Mach number
Nu	-	Nusselt number
p	Pa	static pressure
p_0	Pa	total pressure
pr	-	ratio of compressed air line pressure and ambient pressure
Re	-	Reynolds number

Re_{crit}	-	critical Reynolds number
Re_{δ^*}	-	Reynolds number based on displacement thickness
$Re_{\theta t}$	-	Reynolds number based on momentum thickness at the transition onset
Re_x	-	Reynolds number based on a general position
Re_{tr}	-	Reynolds number at the transition onset
s	m	airfoil span
t	s	time
Tu	-	turbulence level
u	m/s	velocity
u'	m/s	unsteady component of u
u^+	-	nondimensional velocity
$\bar{u}$	m/s	mean velocity
u_A	m/s	amplitute of the unsteady jet velocity cycle
u_∞	m/s	velocity of main stream
u_e	m/s	flow velocity at the boundary layer edge
u_j	m/s	velocity of air jet from the actuator slot (instantaneous)
$\bar{u}_j$	m/s	mean velocity velocity of air jet from the actuator slot
v	m/s	component of velocity in the y-direction
x	m	general position
y^+	-	wall unit

Greek Letters

α	$grad$	angle of attack
δ	mm	boundary layer thickness
δ^*	mm	displacement thickness
η	-	nondimensional wall distance
γ	-	intermittency factor
γ_p	-	fraction of forward flow in the viscous sublayer
λ	-	Pohlhausen pressure gradient parameter
λ_θ	-	Thwaites pressure gradient parameter
μ	kg/ms	dynamic viscosity

ν	m^2/s	kinematic viscosity
ϕ	m/s	fit coefficient used for the calibration of the actuator
ρ	kg/m^3	density
τ	-	duty cycle of the solenoid valve
τ_{ij}	N/m^2	shear stress in the ij plane
τ_w	N/m^2	wall shear stress
θ	mm	momentum thickness
ζ	m/s	fit coefficient used for the calibration of the actuator

Abbreviation

AFC	Active Flow Control
DNS	Direct Numerical Simulation
IA	Interrogation Area
IGV	Inlet Guide Vane
LDA	Laser Doppler Anemometry
LPT	Low Pressure Turbine
NACA	National Advisory Committee for Aeronautics
PIV	Particle Image Velocimetry
PFC	Passive Flow Control
RANS	Reynolds Average Navier-Stokes
RMS	Root Mean Square

List of Tables

List of Figures

Chapter 1

Introduction

1.1 Introduction

Boundary-layer separation is a physical phenomenon with harmful consequences for engineering applications. Airfoils, turbomachine blades, diffusers and flow passages are some machine elements affected by its negative effects, such as pressure and mixing losses, blockage and vibration. In this work, boundary-layer separation is addressed exclusively in turbomachinery context, as described below.

To illustrate the role of boundary-layer separation, a few words about its effects over compressors, turbines and diffusers: to achieve the highest efficiency compressors have to operate close to stall. However, a margin from stall must to be kept to guarantee a safe operation, forcing the machine to run at design points of lower efficiency than technically possible. Turbines are subjected to flows at very high temperatures coming from the combustion chambers, well above 1100 °C. Under such conditions, boundary-layer separation may lead not only to a lower capacity of work extraction but also to the development of hot-spots that may cause material failure and interruption of operation. In diffusers, separation reduces pressure recovery and causes flow blockage. These are examples of how turbomachinery are affected by boundary-layer separation.

The evolution of thrust-to-weight ratio of gas turbines in the last decades is depicted in the figure 1.1. Since the 80's the thrust-to-weight ratio did not experience significant increase, which demonstrates that conventional design practices reached its limit and that further performance gains demand efforts using unconventional approaches. Active boundary-layer control is likely to permit a further jump in performance that would not be possible using conventional aerodynamic modifications.

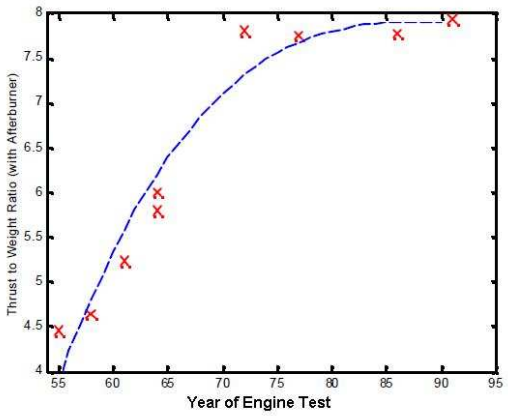

Figure 1.1: Evolution of aeronautical turbine thrust to weight ratio [1].

Simultaneous to the presentation of the boundary-layer concept in 1904, Prandtl also demonstrated the effectiveness of active control for flow separation around a cylinder by suction through a slot. Since then, however, passive methods prevailed in usual engineering practice.

Passive control methods are geometrical modifications that do not require power expenditure and usually are physically fixed, e.g. surface topology optimization and riblets. However, when flow control is not necessary or when the machine operates at its design point, passive control techniques usually cause extra mixing losses and increased drag - the advantage of active control is that it operates only under specific flow conditions.

In recent years research has been conducted to make the implementation of active control in real applications feasible. Active control can be implemented through different technologies such as air injection, air suction and acoustic excitation [2, 3, 4].

Intensive research have been conducted with zero net mass flow actuators, also known as synthetic jet actuators [5, 6, 7, 8] and with pulsed injection [9, 10, 11, 12]. Synthetic jets actuators aspirate the low momentum boundary-layer flow through slots or holes placed at strategic positions over surfaces and subsequently inject the air back into the boundary-layer with a higher momentum level without addition of mass. Pulsating jets, also called modulated injection, adds both momentum and mass. The main advantage is the reduction of the necessary power for the active control system by orders of magnitude, when compared to steady air injection and suction.

Active control methods are classified as either open-loop or closed-loop. In the former, the control mechanism is switched on when certain predetermined operation points are

matched by the actual operation regime, independent of the real condition of flow. For example, in a turbomachine, when a specific combination of rotational speed and mass flow is matched, the active control is turned on, but it does not unconditionally mean that the flow is separated and that control is thus necessary. For this reason an open-loop scheme requires careful machine testing and system calibration to guarantee that the activation occours at the correct flow condition.

On the other hand closed-loops are equipped with sensors and data processing hardware to interpret the actual flow condition. According to the aquired flow information the control mechanism is switched on and the pertinent parameters are adjusted. McAuliffe [13] designates open and closed-loops as pre-determined and reactive control schemes, respectively.

The importance and applicability of active control methods are not restricted to compressors and turbines; also wings, airfoils, flow passages and combustion chambers may profit from it. A compromise must be sought between benefits, complexity and costs of the added mechanisms. Aerodynamic characteristics of stealth surfaces, due to their flattened design, are not aerodynamically optimized but can be improved since active control creates virtual shapes and minimize the need of moving parts without loss of stealth characteristics [5]. Small unmanned aerial vehicles (UAVs) have flight envelopes at low Reynolds numbers and are hence prone to experience laminar separation. Active flow control can be suitable to improve their performance. Reduction of aircraft engine size, while keeping the same thrust, can be realized if transition ducts, connecting high and low pressure turbines, have their length shortened and their radius increased. That would increase the blade tip speeds and consequently increase the extracted work per stage [1]. Tighter duct bends, however, are often followed by flow separation, increased losses and blockages. Inlet Guide Vanes (IGV) can also profit from active control if the existing anti-ice subsystems could be adapted for this application.

The examples mentioned above suggest possible application fields for active control methods and are the motivation for present work.

1.2 Previous Research - Literature Review

A compilation of current research in the field of active flow control (AFC) is presented in this section. Some terms and concepts are introduced here and a deeper explanation is found in Chapter 2. AFC finds a number of potential applications in fluid dynamics as mixing enhancement, transition control, separation management and separation control. Though AFC can be realized using different techniques, this review focuses on air injection, air suction and a combination of these, although others are also cited.

Hsiao et al. (1989) [14] tested experimentally the effect of internal acoustic excitation on a NACA $63_3 - 018$ airfoil in a wind tunnel at Reynolds number between $6,3 \times 10^3$ and $5,0 \times 10^5$. Loudspeakers were installed in the left and right side of a hollow airfoil. A slot near the leading edge connected the hollow cavity and the speakers with the exterior and therefore with the outer flow. The loudspeakers induced an air stream through the slot, whose intensity and frequency could be controlled with the power and frequency of the signal supplied to the speakers. Flow separation could be well managed when two conditions were achieved: first, when the disturbance frequency matched that of the separated shear-layer instability and second, when the position of actuation was suitably chosen. In their experiments the excitation level (amplitude of disturbance) played a less relevant role.

Chang et al. (1992) [4], from the group of Hsiao cited above, noticed that increments of excitation level extend both the effective forcing frequency range and the angle of attack without separation. Bar-Sever (1989) [15], using an oscillating-wire to increase transversal velocity fluctuations in a LRN(1)-010 airfoil at $Re = 1 \times 10^6$, asserted that the optimal excitation frequency is 40% higher than the separated shear-layer instability frequency.

Seifert et al. (1993) [16] employed pulsated jets in a flapped NACA 0015. The flap corresponded to 25% of the airfoils' total chord and was equipped with a blowing slot at the hinge. The power expenditure with the pulsated injection was one order of magnitude lower than that with constant injection for the same performance improvement. The optimal nondimensional actuation frequency was of order of unity.

Smith and Amitay (1998) [5] used a single modified NACA series 4 airfoil to study the influence of excitation position and magnitude. They adopted a double-slotted synthetic jet actuator. The leading edge of the airfoil was replaced by a cylinder, which could be rotated over its axes to change the circumferential position of the slots. They found that the closer the slots were to the separation point, the more effective the AFC was.

That resulted in a reduction of two orders of magnitude in the necessary energy input, given by the non-dimensional *momentum coefficient* C_μ [1]. However, when the slots were distant from the separation point, a steep decrease of effectiveness [2] took place when the momentum coefficient was below a minimum value.

McCormick (2000) [6] introduced the *Directed Synthetic Jets*, made with internal acoustical excitation - similar to the one used by Hsiao - and a curved neck or slot in the streamwise direction. He demonstrated the technique in a two dimensional diffuser and in an airfoil. The diffuser was designed with a half angle of 13°, thus at the limit of flow separation. The power of the loudspeakers was varied from 0,2 W to 20 W. About 1 W was consumed only to achieve the diffuser nominal performance, since the presence of the slot disturbed negatively the flow. Increasing the power from 1 W to 5 W a monotonical recovery was realized; above this level the separation on the upper surface of the diffuser prevented further improvement. He argued that the AFC employed performed better than a vortex generator tested previously because of its parasitic drag penalty. The most effective nondimensional actuation frequency was around unity, however it could be related to the decrease of the magnitude of synthetic jet oscillation as the frequency was increased - a particular characteristic of this actuator design. In the second demonstration a slot was placed at 4% of an airfoil chord, just before the separation point. The majority of tests were conducted at $Re = 5 \times 10^5$ and $Ma = 0{,}05$ but also at $Re = 10 \times 10^5$ and $Ma = 0{,}10$. In both cases the presence of the slot reduced the stall angle by 1° but the actuation displaced the stall margin up to 6°. A systematic investigation did not show a connection between C_μ and the nondimensional actuation frequency (f^+), when the last was varied between $0,25 \leq f^+ \leq 3,5$, where $f^+ = fc/u_i nfty$ - further details about f^+ are presented in the section 2.2.

Bons et al. (2001, 2002) [9, 10] investigated pulsating jets in a linear cascade with a single low-pressure turbine blade profile (Pak-B) in a low Reynolds number range, 25.000 $\leq Re \leq$ 100.000. The injection was performed using vortex generators - holes made in the airfoil's suction surface with pitch angle of 30° degrees [3] and skew angle of 90°, [4] air jets were then injected through these holes in the boundary-layer. The vortex generators'

[1] C_μ is a measure of injected momentum, composed of two components: c_μ, which corresponds to the mean flow injected while c'_μ corresponds to the unsteady component of the injection - see chapter 2.

[2] specified as the ratio of C_l and C_d

[3] Pitch angle is the angle between the jet axis and the surface.

[4] Skew angle is the angle between the projection of the jet in surface and the mean stream angle.

rows were placed at two positions, at 43% and 65% of the chord length. They suggested that the flow management achieved obeyed different physical mechanisms: at the most upstream position the control was due to free-stream entrainment to the boundary-layer, bringing high momentum flow; while at 65% of the chord the flow management was due to boundary-layer transition. Compared with steady blowing, unsteady injection resulted in a reduction of one order of magnitude of the necessary injected air mass flow - as observed by Seifert et al. [16] and Smith et al. [5]. They proposed that the unsteady flow generated at the start and at end of the pulsing cycle was responsible for the achieved effects and not the injected air jet itself. Furthermore no preferable nondimensional actuation frequency in the range $0{,}1 \leq f^{+} \leq 10$ was observed, in accordance with McCormick [6]. In a more recent work (2008) the group of Bons et al. continued to investigate the hole of vortex generating jets (VGJ) used the same Pak-B low pressure turbine airfoil at Re = 20.000 with 3% free-stream turbulence level. They stressed that the unsteady injection (pulsed jet) reduces the air mass flow to an almost negligible fraction - about 0,01% of the core mass flow of a turbine. They noted that the VGJs create a premature transition, which is responsable for bringing high-momentum flow into the boundary-layer.

Volino (2003) [8] used the same blade profile as Bons et al. in a linear cascade composed of two hollow blades operating at $Re = 25.000$. Synthetic jets were generated by connecting loudspeakers to the blade's internal cavity. He noted that calmed regions arose as the disturbances caused by the vortex generators, located in a spanwise row at 51,4% of the chord, convected downstream. Therefore AFC disturbances had an effect similar to that of turbulent spots. Boundary-layer separation persisted even within the calmed region but remained very thin.

Culley et al. (2004) [11] implemented AFC in two stator blades of a low-speed multi-stage compressor. The blades in the stator row were restaggered to intentionally promote flow separation. Three different actuator configurations were used: slot-vanes, hole-vanes and embedded fluidic devices (Fig. 1.2). The vanes covered from 60% to 90% of the blade span. Both steady and unsteady air injection were examined. The actuation position was the same as the separation point, located at 35% of the chord, which was asserted after testing a single airfoil in a low speed wind tunnel. Pulsated injection was generated either by a motor-driven valve, installed outside the compressor case, or by the fluidic device installed in the blades. The three designs were tested using constant air injection and pulsated injection. The most effective combination was the slotted vane with pulsated

injection. They reduced the losses by 25 % injecting an equivalent of 1% of throughflow mass flow. Loss reduction was calculated by the conventional loss coefficient given by $\omega = p_{01} - p_{02}/p_{01} - p_1$ corrected by the injected mass. Again, unsteady injection reduced the necessary air mass addition through injection for a given performance improvement. When steady injection was utilized, a minimum level of C_μ had to be kept to avoid flow deterioration due to injection of low momentum fluid. A weak dependence on actuation frequency was noticed but Culley et al. stated that it was not related to the coupling of shear layer instability frequency and actuation frequency but rather due to the resonance of the injection system. Another relevant point is that saturation of C_μ was noticed, probably due to the increase in mixing losses, pointing out a upper limit for the benefits of momentum injection. They also related pulsation efficiency to a high c'_μ/c_μ ratio.

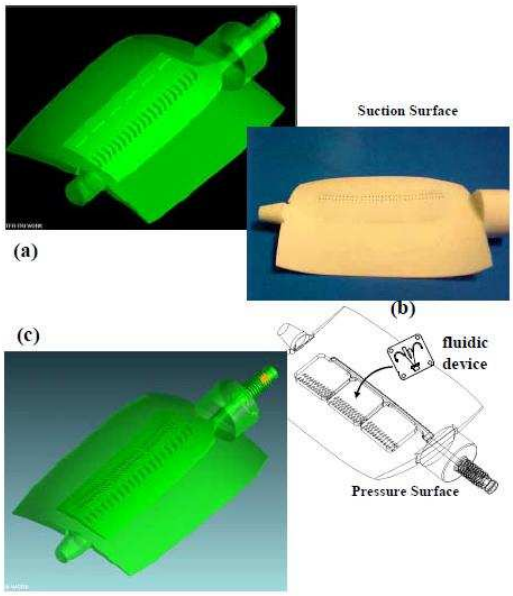

Figure 1.2: AFC vane designs: a) slot vane b) embedded fluidic device c) hole vanes [17].

In a subsequent investigation, Culley et al. [12] used the same machine but now restricted to the slot-vanes, which covered from 10 % to 36 % of the blade span (hub region). Four blades were restaggered in 4° degrees (positive) to promote early separation and pulsated injection was employed in the two central blades. The actuation system was improved to avoid resonance issues and a high speed solenoid valve was adopted as a replacement for the siren valve. Although air was injected only in the hub region, the effect could be noticed in the whole span, because low momentum flow from hub was kept away from the rest of the blade. Regarding the nondimensional actuation frequency, they

noted that f^+ around unity was the most efficient. However, once a certain minimum valve "open-time" was fixed (in this case 1,2 ms) the frequency could be reduced and the system efficiency remained almost constant in the range $1 \leq f^+ \leq 3,1$.

Wang (2003) [7] conducted a numerical investigation based on the work from Hsiao [3]. A synthetic jet slot was first modelled at the leading edge of a NACA $63_3 - 018$ and thereafter in a compressor stage made up of the same NACA profile. She concluded that the amplitude of the perturbation had minor influence on the effectiveness of the control scheme but the range of effective frequency was extended for higher inputs. Wang proposed that the optimal actuation frequency shall lie between 1,5 and 2,0 times the characteristic frequency, given by $f_c = u_\infty/(c\cos\alpha)$. Subsequently, this correlation was extrapolated successfully to the compressor stage simulation. The drag of stator and rotor were reduced by 50 % and the pressure losses by 66%.

Supporting the conclusions from Wang, the numerical simulation from Xin-qian et al. (2005) [18] in a compressor cascade pointed out that the optimal frequency of actuation lies around the frequency of vortex shedding within a relative wide range while the best position to implement the excitation lies directly upstream of the separation point. They mentioned the need to maintain the synthetic flow amplitude within some limits (in accordance with the observation from Culley [12]).

Yarusevysch (2005) et al. [19] investigated the relation between shear layer instability frequency and separation control. A thick NACA 0025 airfoil was used in a wind tunnel at $Re = 100.000$ and 150.000. The shear layer formed a separation bubble at the higher Re but failed to reattach at the lower Re. Acoustic excitation improved the airfoil performance when the actuation frequency matched that of natural instabilities in the shear layer.

Ortmanns and Kähler (2004) [20] analysed the interaction of air injection and a turbulent boundary-layer. They used vortex generators, which were designed to affect the flow similarly to conventional fixed vortex generators, to bring high momentum flow into the boundary-layer. They found out that skewed injection was more effective to produce vortices and to transport momentum to the boundary-layer. They stated that the effect of pulsation occurs during the instants of opening and closing of the valve, as noted by Bons et al., and that between the opening and closing the air injection behaves like a constant injection. Kähler et al. (2007) (in [21]) examined the interaction of AFC with vortex generators. Adopting the ratio of the injected jet velocity and free-stream velocity, u_j/u_∞, to measure the extension of effectiveness of their system, they stated that with

low ratios the injection does not interfere with the flow and that when the ratio is too high, the generated vortices are formed too far away from the surface and are therefore not able to promote mixing in the boundary-layer. The actuation frequency did not show a major influence, while duty cycle (τ) [5] had to be adjusted according to the distance between actuator and separation - larger τ being generally more adequate for far fields and shorter τ for near field control.

From the current literature review there are some points and conclusions that can be asserted: no agreement exists regarding the most effective nondimensional actuation frequency f^+. Some authors argue that f^+ must couple with the shear layer instability frequency [19] or with the vortex generation frequency, while others did not detect any connection between f^+ and the effectiveness of the system or at most only a weak dependence on f^+. In the cases where the actuation frequency seems to play a role, the value $f^+ = 1$ is often reported as an efficient one. The amplitude of injected air, given by the momentum coefficient, seems to be kept within a certain range - below this range, it may impact negatively the flow while above this range it does not contribute any further. The mechanism related to this fact is not completely clear. Regarding the actuation position, most authors point out that AFC shall be positioned upstream of the separation point and that the actuation intensity has to be determined appropriately to not deteriorate the flow.

1.3 Problem Statement and Purpose of Present Work

Low Reynolds number flows prevail in turbomachinery applications like first stages of axial compressors, first stages of high pressure turbines and low pressure turbines. However, operation within a low Reynolds number range leads to highly stable laminar boundary-layers, which are more susceptible to separation than transitional or turbulent boundary-layers. This statement corroborates the significance of research on active control at low Reynolds number.

Volino [8] refers to open questions that should be further investigated: the effect of pulsation frequency and intensity (amount of injected air) and also cites the need for a more detailed description of boundary-layer development under active control using experimental methods.

[5] Duty cycle (τ) is the ratio between the open-time and the period of a solenoid valve cycle.

The present work continues the efforts made at the *Technische Universität Darmstadt* related to boundary-layer control, such as the experimental work from Werden (1998) [22] and the numerical simulations from Wang (2003) [7].

In the present work an open-loop scheme is implemented in an airfoil to control leading-edge stall at low Reynolds number. A symmetric NACA $63_3 - 018$ is used to simulate laminar separation over a blade operating at low Reynolds number, as adopted by Wang. Reynolds number is kept at 90.000 - representative of a real machine - while the pressure gradient is varied as the angle of attack is changed. Both steady and unsteady (pulsed) air injection are implemented to investigate the influence of the control parameters and to figure out how to reduce the necessary energy expenditure while keeping the flow attached under conditions where the flow would be otherwise detached.

The interaction between the pulsed jets and the boundary-layer/separated flow is measured using three experimental methods: static pressure distribution measured with pressure taps, particle image velocimetry (PIV) and hot-wire anemometry. The main effort was to characterize the development of the boundary-layer during different control conditions. The interaction between separated boundary-layer, injection and main flow is presented and discussed. The results may be used to evaluate the feasibility of such an active control design and to supply information to further research in the subject.

1.4 Structure

The relevance of flow separation in industrial applications, in particular related to aeronautical and turbomachinery utilisation, was presented in the introduction. The chapter is followed by a compilation of the current works engaged with the development of active flow control and its physical understanding. The illustration of the current work's objectives closes the first chapter. Chapter 2 depicts how boundary-layer separation occurs and which is the actual state of flow control theory. The experimental techniques employed are described in chapter 3 as well as the test rig, airfoil and actuator used. Estimatives of experimental uncertainty is addressed in the same chapter. The most relevant results are presented and discussed in chapter 5. The work closes with the conclusions and proposal for future works in the Chapter 6.

Chapter 2

Boundary-Layer Theory and Separation Control

This chapter presents theoretical concepts for the discussion of experimental results presented later in the current work. Flow separation is discussed in the section 2.1 with the support of an extensive literature review. A review of flow control approaches is presented at section 2.2.

2.1 Flow Separation

The subject of flow separation is vast and complex and a classification of the different separation process is useful to clarify the subject. Independently of the separation process, it is always necessary that viscous effects and adverse pressure gradient are present simultaneously. This section addresses incompressible laminar and turbulent separation and separation modes typical of airfoil sections. Due to the importance of separation bubbles, special attention is given to this phenomenon.

2.1.1 Laminar Separation

A flow subjected to adverse pressure gradient may detach since pressure forces are applied in the opposite direction and momentum is lost due to the viscosity in the boundary layer. If the separation occurs before transition, the separation is called laminar separation. The classical theory defines the laminar separation point (or separation line) as the location where wall shear stress vanishes $\frac{\partial u}{\partial y}|_{y=0} = 0$ Just downstream of detachment reversal flow

takes place with subsequent thickening of shear layer, as shown by figure 2.1.

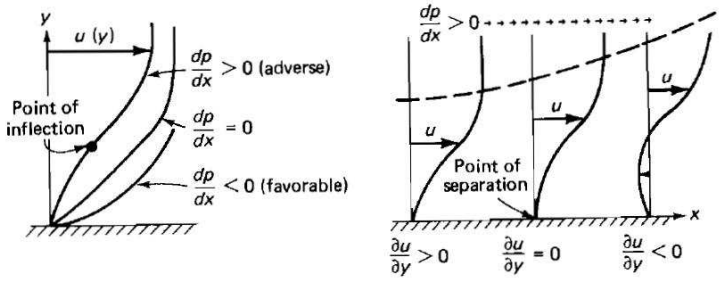

Figure 2.1: Boundary layer profiles due to pressure gradient before (left) and after separation (right) [?].

Analytical methods are available to predict the position of laminar separation, among them are the methods from Pohlhausen, Thwaites and Karman-Milikan [?]. The Pohlhausen's is based on a dimensionless velocity profile expressed by a fourth order polynomial and the separation occurs when the parameter $\lambda = (\delta^2/\nu)(\mathrm{d}u/\mathrm{d}x) = -12$. The method of Thwaites adopts the separation criteria $\lambda_\theta = 0{,}082$ and $H = 3{,}7$.

An unusual kind of separation occurs when the surface is in motion. This is likely to occur in compressor blades during acceleration, for instance. If the surface moves downstream the separation is characterized by singular velocity profile presented in the figure 2.2 (A), the separation takes place actually away from surface and is not very sensitive to pressure gradient. If the surface moves upstream the velocity profile becomes very flat as shown by figure 2.2 (B). If the surface movement is downstream an extension of the Pohlhausen method can predict laminar separation, but for upstream movement no theoretical treatment can be made [?].

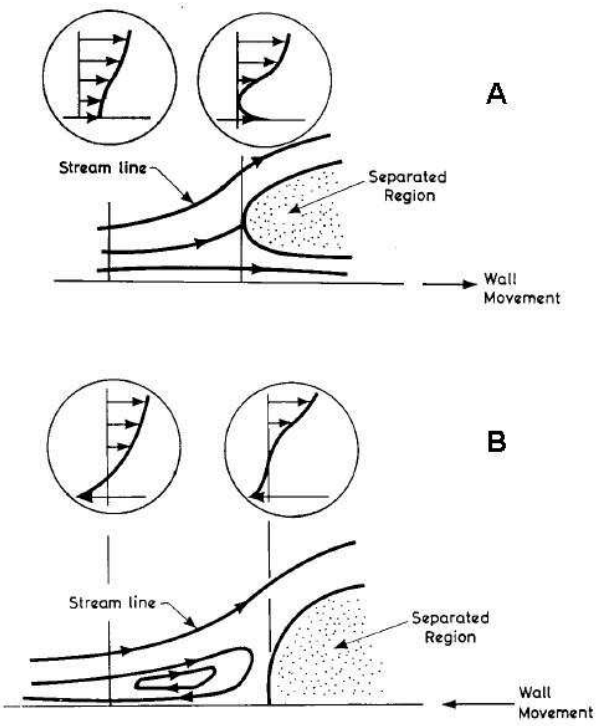

Figure 2.2: Flow field around an unsteady laminar separation with moving wall [**?**].

2.1.2 Separation Bubbles

Boundary-layers are more stable in low Reynolds number regimes and resist longer to transition, however once a positive pressure gradient is imposed to the flow, laminar separation may occur and originates a separated shear-layer above the surface. At a certain distance downstream the shear layer completes the process of transition becoming turbulent (separated transition). Since turbulent flows are efficient momentum conductors momentum entrainment from the main flow to the separated shear layer may yield to reattachment downstream of the separation place. The region between detachment and the reattachment is called separation bubble. As displayed by figure 2.3, the upstream section of the bubble is demarcated by laminar separation and the formation of a separated shear layer, where the transition takes place and reattaches further downstream. The inner region is marked by a very slow flow movement. The transition increases drag and causes premature turbulent separation with negative impact on aerodynamic performance of blades and airfoils, it may, however, prevent a more prejudicial laminar separation that could take place otherwise. Hence the formation of separation bubble may be wisely used to improve performance in off-design operation.

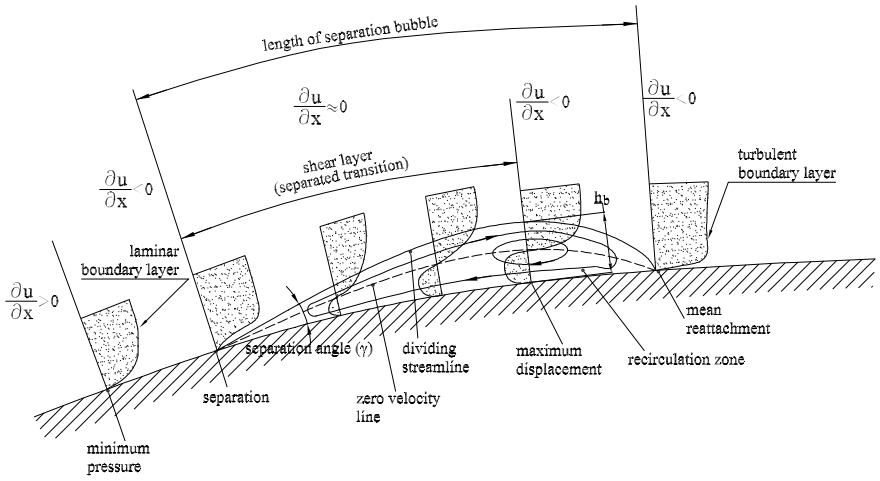

Figure 2.3: Scheme of a separation bubble [?].

The bubbles are classified according to disturbance caused on the static pressure distribution. The so called *short bubbles* are small relative to surface length (a few percentage of an airfoil's chord) and practically don't affect the pressure distribution. However, when the Reynolds number decreases and the pressure gradient is high the momentum exchange within the separated shear layer may be insufficient to promote reattachment and the bubble is said to burst. If the shear layer reattaches close to the trailing edge a large recirculation zone is created and the pressure distribution is strongly affected, in this case the bubble is classified as a *long* separation bubble [?]. Figure 2.4 compares the impact on the pressure distribution of an airfoil caused by long and short bubbles.

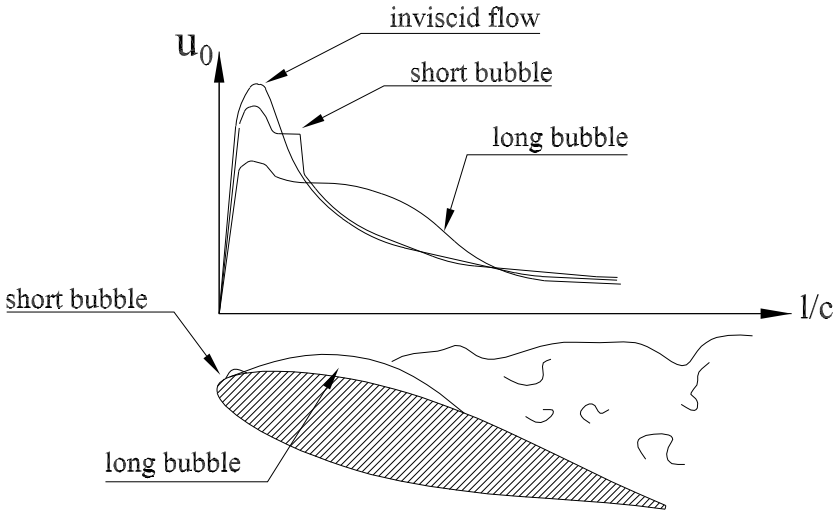

Figure 2.4: Impact of separation bubbles on velocity distribution over an airfoil.

Although a short bubble doesn't seem to be a major issue, a slight change in the oper-

ation condition, e.g. small change of angle of attack or reduction in the actual Reynolds number, may be enough to transform it in a long bubble. A worse case is when the shear layer doesn't reattach at all, causing a massive separation. A criterion to determine whether the shear layer will reattach or not is the Reynolds number based on the displacement thickness at the laminar separation, in spite of scatter in experimental data a reasonable value for reattaching shear layer is $Re_{\delta^*} \approx 350$ at the separation point [**?**]. Bubble burst is the origin of the hysteresis in airfoil lift curves because setting the conditions as before the bubble burst does not result in bubble recovery instantaneously; e.g. if the bubble bursts after an increase of 1° in the angle of attack decreasing the angle of attack by 1° is unlike to be enough yielding to different behaviour of lift curve when increasing and decreasing the angle of attack.

From the above discussion one concludes that performance prediction of airfoils and blades is closely related to the capacity of predicting bubbles onset and flow separation. The available prediction methods are almost all semi-empirical: Horton [**?**] provides a separation bubble method, which is based on the pressure distribution and Reynolds number to determine if the shear layer reattaches and to calculate the momentum thickness growth above the bubble. An exception is the correlation from Redford and Johnson [**?**] who modified an existing transition model for attached transition to account for separation based on the physics of separation, however it is semi-empirical since an existing semi-empirical model was used as a starting point.

2.1.3 Turbulent Separation

Turbulent flows feature a greater momentum exchange between boundary-layer and main flow than laminar flows, resulting in a wall shear stress 10 to 1000 times higher than that of laminar flows. For this reason turbulent boundary layers resist better to separation. That fact is used in some airfoil and blades designs aiming to expose the boundary-layer to adverse pressure gradient only after transition onset or transition completion - for instance the lift of a turbulent airfoil is four times greater than the lift of its laminar boundary-layer airfoil counterpart, the penalty is the increased drag. Therefore, to be able to make good performance prediction a reasonable estimation of turbulent separation process is necessary and demands sound knowledge of the turbulent separation process. In the literature there is a number of works treating this topic; extensive reviews are due to Simpson [**?**, **?**, **?**, **?**]. The prediction of turbulent separation is addressed by Chang [**?**],

Kline et al. [?], Castillo et al. [?] and Houtermans et al. [?].

What distinguishes the laminar and turbulent separation modes is that for the latter separation is not a single event, which is often addressed as *separation point* but rather the turbulent separation is an unsteady *process* with forward and backward flow movement around the detachment position. There is no clear separation line as in laminar separation but rather small "packages" are ejected from the viscous layer and flow upstream, after being mixed out the flow back downstream. In a steady laminar separation the wall shear stress vanishes at separation point, while wall shear stress in turbulent separation results from an average over three-dimensional, unsteady, backward, forward and up and down motions [?].

The research groups that study flow separation do not use an unified terminology since separation and detachment are often used as synonyms. Effort has been made by Simpson [?, ?] and Kline et al. [?] to define a unified nomenclature, to describe turbulent separation processes more precisely. It shall first be stressed that the concept detachment represents a process or location where the boundary-layer departs from the surface while *separation* refers to the region that comprises flow detachment, reverse flow zone and a possible reattachment zone. To describe the turbulent separation the variable γ_p is introduced to explain the modern conception of turbulent separation. It represents the fraction of time the flow moves downstream, equivalent to the intermittency factor. The upper drawing of figure 2.5 shows the old concept of separation, very similar to the concept of laminar separation, in which the separation takes place at a point or line (for two dimensional flows). However, the measurements sensitive to the flow direction of Simpson with Laser Doppler Anemometer pointed out that the process of turbulent separation is more complex than this simple idealization. As one sees in the lower drawing of figure 2.5 in the region called *incipient detachment* (ID) the flow moves backward 1% of the time ($\gamma_p = 0{,}99$); in the *intermittent transitory detachment* (ITD) zone backward flow comes out 5% to 20% of the time ($0{,}80 \leq \gamma_p \leq 0{,}95$) and *transitory detachment* (TD) when backflow takes place 50% of the time ($\gamma_p = 0{,}50$). *Detachment* (D) itself is defined as the location where the *mean* wall shear stress is zero ($\tau_w = 0$). From this observation one concludes that the laminar model of separation is not suitable for turbulent separation since it is rather a gradual process and not a suddenly one. The correlations developed using the oversimplified turbulent separation mode have considered the incipient detachment point predicting an earlier detachment than it actually occurs.

Therefore adopting the complete description turbulent separation yields to more precise separation and performance prediction methods.

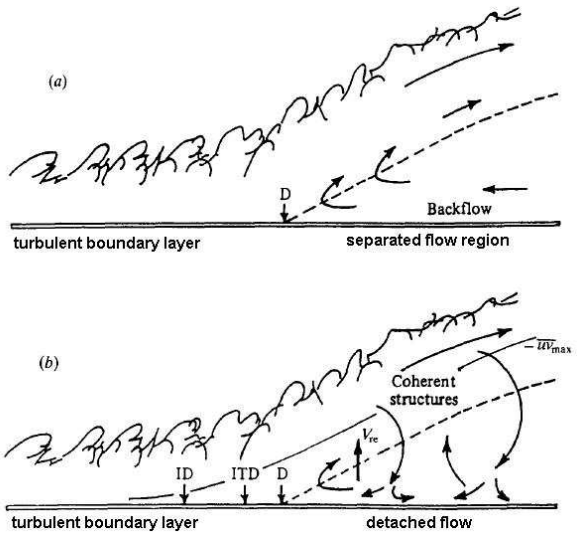

Figure 2.5: Old and modern definitions of separation process [?].

Many methods developed so far to predict turbulent separation are based on the integral momentum equation and in the outer region of boundary-layer and are expressed as a function of shape parameter H, which lies around 2,7 at ITD, and 4,0 at the detachment [?, ?].

2.1.4 Airfoil Stall

Stall is the flow condition after the first peak in the lift versus angle of attack curve ($C_L \times \alpha$) and is intrinsically linked to boundary-layer separation. In the specific case of airfoils separation occurs according to one of three modes: leading-edge stall, trailing-edge stall or thin-airfoil stall, it is possible that more than one mode occurs at the same time. An extensive review of those separation modes can be found in McCullough and Gault (1951), they tested the NACA $63_3 - 018$, 63-0012, 63-009, 64A006 airfoils and a sharp-edged section to analyze the stall modes [?].

Typical of thicker airfoils, the trailing edge stall features turbulent separation at the rear section of the airfoil that moves upstream as the angle of attack is increased. This separation mode results in a rounded lift peak in the $C_L \times \alpha$ curve with a gradual and continual change in the separation position and aerodynamic forces. The slope of lift-curve starts to decrease as the turbulent separation moves upstream, where the maximum lift

is achieved when the detachment takes place at 50% and 60% of the chord. An indicative of turbulent separation is the shape parameter in the range 2,6 $\leq H \leq$2,7. Airfoils such as the NACA $63_3 - 018$ used in the current work, may feature a small laminar separation bubble at the leading edge that at first sight is irrelevant but may boost the turbulent separation onset.

Leading-edge stall is characterized by a sudden boundary-layer separation that extends over the surface reattaching close to the trailing edge. This is typical of airfoil with moderate thickness, between 9% to 15% of the chord length. The lift curve is very sharp because it reflects the sudden separation. McCullough and Gault did not notice reattachment for their 12% thick airfoil, while in the 9% thick airfoil laminar separation occurred close to the leading edge and the shear layer reattached after transition at 20% of chord length forming a long separation bubble. In both cases, however, H attained the critical value of 2,6 at detachment.

The thin-airfoil stall mode takes place after the flow faces a very sharp leading edge and thus a strong adverse pressure gradient. The separated shear-layer passes the front part of the surface and reattaches downstream without further separation.

2.2 Separation Control

Separation control may be classified as active or passive methods. Well established in fluid dynamics design, passive flow control is performed through changes in boundary conditions, such as changing the pressure gradient or free-stream turbulence level, through modifications in a body's aerodynamic shape/configuration or through implementation of passive devices as riblets, spoilers or large break-up devices (LEBO). However, passive flow control methods seem to be at their limit in improvement capability, while even more economically efficient aerodynamic devices are being demanded by the market, e.g. wings, blades, combustion chambers and transportation vehicles. Active flow control is probably the most promising alternative to meet high demands of aerodynamic efficiency. The advantages and shortcomings of active and passive methods are presented in the tables 2.1 and 2.2, from [**?**].

Table 2.1: Aspects of Passive Flow Control methods.

Advantages	**Disavantages**
Easy to implement	*Re* dependent
No external energy source	Off-design sensitivity
No mechanical or electro-mechanical parts	Often associated drag penalty

Table 2.2: Aspects of Active Flow Control methods.

Advantages	**Disavantages**
Adjustable	Technically more complex
Adaptability to variable flow conditions	External energy source necessary
Separation management for off-design performance	
Closed-loop feedback possible	

In opposition to passive control, active control manipulates the flow only when necessary. Thus it avoids that the aerodynamic properties of a device are negatively impacted due to the use of a feature in an inappropriate moment, an example of such case is the extra drag and boundary-layer thickening caused by riblets due to its presence when the boundary-layer is attached and not prone to separate.

In addition, active control demands external energy input, it is thus kept off when not necessary, saving energy and improving a device's efficiency. The goal of a successful active flow control design is to expend less energy than the savings resulting from its implementation. Gad-el-Mak [21] does some rough calculations to demonstrate the economical feasibility and states that the future of active control of turbulent flows relies

on fast improving technologies: chaos control, micro-fabrication and new computational tools.

The adopted classification of active control methods is made according to the scheme proposed by Gad-el-Hak [**?**]: active methods are divided in two groups: open-loop (predetermined) and closed-loop (reactive) control modes (Fig. 2.6). The first is implemented after previous extensive calibration of the system formed by the actuator and the flow to be controlled, previous calibration allows determining the optimal control parameter adjustment for specific operating points. Although open-loop schemes are simpler to implement they are more likely to fail if the real flow condition does not match a previously examined case considered during calibration. To overcome this limitation closed-loop schemes are proposed. They feature sensors to identify flow structures or to measure disturbances to provide information about the real flow condition to a controller in order to determine the optimal control setting.

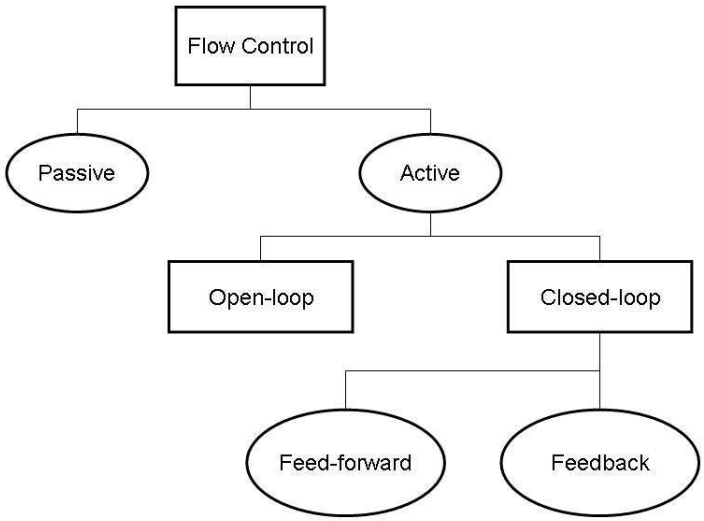

Figure 2.6: Classification of flow control methods [**?**].

2.2.1 Passive Flow Control Strategies

According to the convention adopted, passive flow control (PFC) schemes don't require external energy input. PFC is a vast field with different possible approaches. The current review addressed PFC through geometrical disturbances only. Other strategies are available, such as compliant coating and aerodynamic shaping.

Geometrical Disturbances

Geometrical disturbances are classified as turbulators, riblets, vortex generators or large-eddy break-up devices (LEBUs).

Turbulators are physical obstructions designed to accelerate or modify the transition process, changing a natural transition or a separated transition process to a by-pass transition. Steady or unsteady disturbances can be used for this purpose, they may affect either the free-stream flow or directly the boundary-layer if the surface roughness is modified for instance: an established approach is to place roughness elements on the surface. The difficulty in doing so is to avoid an excessive thickening of the boundary-layer, otherwise the gain obtained from separation control can be offset by the increase in skin-drag. Airfoils operating poorly at low Reynolds number can have their performance enhanced using turbulators, however this technique may not be adequate for airfoils with low drag in this regime.

LEBUs are designed to break-up the large vortices formed at the edge of turbulent boundary layers. Their typical configuration is formed by a pair of small airfoils or flat surfaces placed in tandem about 10δ apart from each other and $0{,}8\delta$ away from the surface. Chord and thickness in the order of δ and $0{,}1\delta$ respectively are typical [**?**].

Riblets are formed by wall channels aligned with the flow direction, they can be V-shaped, fin-shaped or valley-shaped. A remarkable feature of riblets is that even with the increase in area and thus in skin drag, net drag reduction is reported to lie between 4% and 40%.

Vortex generators are small airfoils with low aspect-ratio fixed perpendicular to the surface, they are usually mounted in pairs and generate either counter-rotating or co-rotating vortices. The resulting vortices bring high momentum flow toward the surface energizing the boundary-layer. They are employed in airfoil surfaces, aircraft fuselages and compressor blades. Guide lines to design are given by Taylor [**?**] and Pearcey [**?**], roughly speaking they should have the height equal to the boundary-layer thickness, a yaw angle lower than 15° and the distance between them may be set depending on the type of vortex pair to be generated.

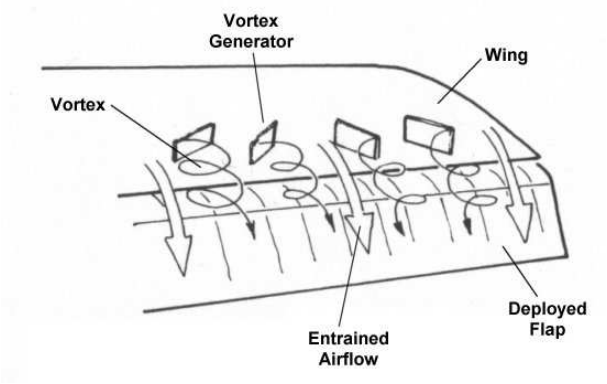

Figure 2.7: Vortex generators: co- and counter-rotating vortices.

2.2.2 Active Flow Control Strategies

In the present section some of the available active control methods are presented. Emphasis is given on the explanation of wall jets, which is the actually method adopted in the experiments conducted.

Heat Transfer

Flow control through heat transfer is based on the principle of Reynolds number manipulation by changing the viscosity and density heating or cooling a surface. Heat extraction from compressible gases and heat addition to liquids reduces the dynamic (or absolute) viscosity μ and increases the density ρ - in the case of liquids the heat transfer has a minor effect on density. The first consequence is that the boundary-layer velocity profile becomes fuller because of the shear stress gradient, second the increase in density results in a greater momentum transport.

Although conceptually simple, the heat transfer method finds limited applications because the necessary temperature difference to be imposed has to be very large requiring a significant heat transfer ratio. Cryogenically-fuelled vehicles are the most natural application field, since they can easily provide significant temperature differences.

Moving Walls

An indirect way to energize a boundary-layer is using a moving surface. It is usually accomplished with rotating cylinders or moving belts installed at the surface level. Moving surfaces transfer momentum to the boundary-layer, which in turn has its separation delayed or suppressed. This method is constrained by the complex mechanical implemen-

tation, the pay off is that it was already successfully used in small sections of airfoils and flaps with increase in lift and postponement of stall up to 48° and also in blunt bodies such as trucks, with drag reduction in the order of 27% [**?**].

Suction

Removal of low momentum fluid through slots on the surface "pushes" the velocity profile toward the surface and it becomes fuller. As explained for the heat transfer method, this profile is less prone to separate. Prandtl used the Pohlhausen method and the integral equation to determine the necessary suction coefficient, $C_q = v_w/u_0$, where v_w is the suction velocity (normal to the surface) to prevent boundary-layer separation on a cylinder: $C_q = 4,36Re^{-0,5}$. Turbulent boundary layers require semi-empirical calculations, to prevent separation C_q in the range 0,002 and 0,004.

Wall Jets

Air suction, Air blowing, combination of air blowing and air suction, acoustic excitation and plasma generation are some actuating approaches on flows and on boundary-layer separation. The air suction method, presented for the first time by Prandtl in 1904, consisted in removal of the low-momentum flow through suction slots located at a cylinder surface. Air blowing, on the other hand, supplies extra momentum to the flow so that it is able to withstand the positive pressure gradient without detaching from surface. Plasma actuators impose body forces to control the flow, Grundmann and Tropea used this technique to delay transition by altering the development of Tollmien-Schlichting waves [**?**].

A zero-net-mass-flux actuator, or synthetic flow actuator, does not need plumbing lines as the blowing, suctioning and pulsated jets do. It needs small electrical devices, e.g. piezo actuators, with the capacity of producing excitation at high velocities, high response and high reliability. The restriction to this approach is that high robustness is required from those electrical devices limiting the fields of application (Petz and Nitsche [21].

A combination of air blowing and air suction, called pulsated jets, proved to be more efficient than simply steady blowing or suction - reducing the necessary energy input by 2 orders of magnitude [16, 12]. It occurs because steady blowing relies only on momentum addition, while synthetic and pulsating jets exploit the instabilities of the flow to enhance

the momentum transfer from the main flow to the boundary-layer when large coherent structures are accelerated and regulated [**?**].

The actuator parameters have to be scalable, i.e. it must be possible to estimate if their effects in one test condition would be transferable to others. There are different nondimensional parameters in the open literature used to characterize the frequency and amplitude of the actuation, the adopted definitions and nomenclature follows: the nondimensional actuation frequency f^+ is calculated in a straightforward manner, expressed by equation 2.1.

$$f^+ = \frac{fc}{u_\infty} \tag{2.1}$$

Poisson-Quinton (1948) demonstrated that separation control is done by momentum addition rather than mass addition. From dimensional analysis the momentum coefficient (C_μ) results as an adequate parameter to measure the added momentum and the amplitude of actuation [**?**]. The momentum coefficient is the injected momentum normalized by the dynamic pressure of free stream. It shall be stressed here that in the literature some divergence exists in representation of C_μ for unsteady flow. Usually, C_μ is decomposed in a steady (c_μ) and an unsteady term (c'_μ). Culley et al. [11] present C_μ as an addition of both terms ($C_\mu = c_\mu + c'_\mu$), Greenblatt [**?**] presents both terms separately ($C_\mu =< c_\mu, c'_\mu >$) while Smith et al. use only the steady term ($C_\mu = c_\mu$). Also the definition of the steady and unsteady terms is discrepant, while Culley et al. use the root-mean-square (RMS) of the jet velocity oscillation, Greenblatt et al. use the amplitude of the oscillation. This scenario makes it difficult to compare different experimental results, demanding conversions between the different definitions to be performed at first.

In the present work the definition used by Greenblatt et al. is adopted because the mean and unsteady terms have different effects on the flow: the first adds momentum, while the later interacts with flow instabilities. If the terms are simply added or the oscillatory term is ignored, it is not possible to assert if both instabilities and momentum are been affected by the active control and at which level. It is thus preferred to express the steady and the unsteady terms separately; that enables also to assert the ratio of the terms. The definitions of momentum coefficient and its steady and unsteady components are expressed by equations 2.2, 2.3 and 2.4, respectively.

$$C_\mu =< c_\mu, c'_\mu > \tag{2.2}$$

$$c_\mu = \frac{\rho_j \, u_j^2 \, b}{\frac{1}{2} \, \rho_0 \, u_\infty^2 \, c} \approx \frac{2 u_j^2 \, b}{u_\infty^2 \, c} \tag{2.3}$$

$$c'_\mu = \frac{\rho_j \, u_A^2 \, b}{\frac{1}{2} \, \rho_0 \, u_\infty^2 \, c} \approx \frac{2 \, u_A^2 \, b}{u_\infty^2 \, c} \tag{2.4}$$

Where u_A is the jet amplitude; b and c are the jet slot width and chord length, respectively.

Basic Principles

Synthetic jets are generated by oscillating diaphragms installed in cavities, which are connected to the surface through orifices or slots. Air is suctioned and then expelled forming a shear layer at the orifices or slots edges originating vortex rings or vortex sheets that propagates into the flow breaking down a certain distance downstream and originating a turbulent jet [5].

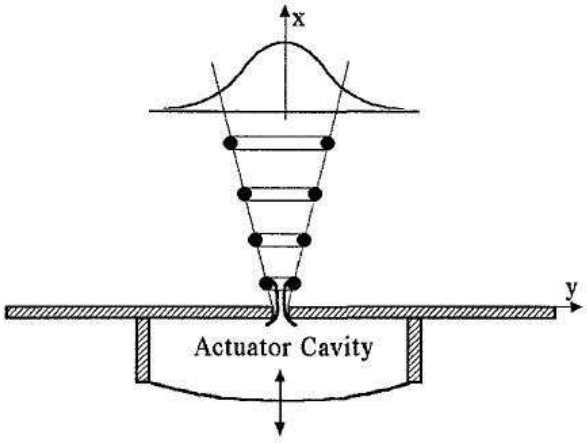

Figure 2.8: Schema of a vortex ring type synthetic jet.

There are two basic principles for separation control: incitement of natural instabilities and the enhancement of turbulent mixing. The first is efficient but not effective when the flow is stable. The second brings high momentum fluid from outer layer improving the turbulent mixing [21].

Influence of Actuator Position

Smith et al. [5] varied the double slotted actuator installed in a rotatory cylinder placed at an airfoil leading edge. They asserted that the magnitude of the minimum C_μ input necessary for a significant separation control decreases by an order of 2 if the slots are positioned close to but a bit upstream of separation; if placed further upstream the control can still be effective but less efficient, due to the cost of higher C_μ expense. In this last case an abrupt decrease in the perturbation efficiency is noticed once a minimum level of input is not supplied - the curves "pos.2" and "pos.3" in figure 2.10 depicts the efficiency decrease if not enough C_μ is supplied by an actuator placed at an unfavorable position. Actuation on the pressure side also showed a global effect in the flow field as it was performed in the pressure side of the airfoil, well below the stagnation point, resulting in lift increase.

The geometry of the actuator exit was investigated by Werden [22] and Kähler et al. [21]. Werden tested a series of different orifices distributions and slots exits and concluded that slots are the most efficient. Kähler et al., on the other hand, suggest that orifices inclined in the range 45°-55° can be the most appropriate configuration.

Actuation Frequency

Greenblatt et al. [**?**] performed a survey of available experimental data from airfoil tests in the range $150.000 \leq Re \leq 900.000$. Most of the investigations addressed thick airfoils and in the majority of cases actuation was placed between the leading edge up to 10% of the chord. Expressed in terms of f^+, the most efficient actuation frequencies were found in the range $0{,}1 \leq f^+ \leq 4$. The wide range can be justified by a C_μ supply above the minimum necessary one, widening the efficient f^+ range. In some cases the most efficient non-dimensional frequency is about $f^+ \approx 10$ [5]. The compilation of results for a NACA 0015 airfoil are presented in the figure 2.9, despite the data scatter a tendency of better efficiency can be identified in the range $0{,}5 \leq f^+ \leq 1{,}5$.

Wang [7] derived a correlation from numerical investigations to determine the optimal actuation frequency based on a characteristic frequency f_c calculated by Eq. 2.5, and found out that it lays in the range $1{,}5f_c \leq f^+ \leq 2{,}0f_c$. This correlation and the range proposed in the open literature serve to determine the range of f^+ to be used in the experiments of the current work. Bons et al [9] were not able to relate a specific f^+ with turbine blade performance improvement, on the other hand, the air mass injected could be reduced by one order of magnitude by using unsteady injection in comparison to steady

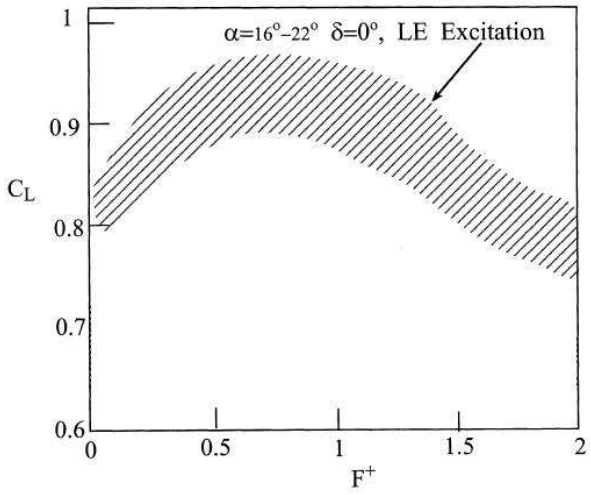

Figure 2.9: Effect of f^+ on C_L of a NACA 0015 [**?**]).

injection for the same performance improvement.

$$f_c = \frac{u_\infty}{c \cos \alpha} \tag{2.5}$$

Actuation Level

A survey from Greenblatt and Wygnanski [**?**] shows that excitation frequency between $0{,}01 \leq f^+ \leq 3$ are the most efficient when the ratio jet amplitude/free-stream velocity lies between $10 \leq u_A/u_\infty \leq 300$ and the slot width is smaller than 5% of the chord $b \leq 0,05c$ [**?**]. They noticed that once a certain excitation level is reached only minimum improvement, given by the ratio C_L/C_D, can be accomplished by further increasing C_μ. For instance increasing C_μ by one order of magnitude resulted in only 10% increase in the C_L/C_D ratio of a NACA 0012 and a NACA 0015 airfoil.

A similar fact was reported by Smith et al. [5] and depicted by figure 2.10, here the improvement obtained from actuation in 3 different positions is drawn as a function of the excitation level: it is ascertained that actuation in an appropriate location (1) yields to a smooth rise of C_L/C_D in the whole C_μ range compared with those not optimized actuation positions. However, once the threshold levels in the other positions are reached the gain jumps abruptly and remains almost constant from this level on. No clear explanation was found for this phenomenon. This question is addressed in the PIV results discussion.

Culley et al. observed from their compressor test rig that steady or pulsated injection performed below a critical level can lead to performance deterioration due to the injection

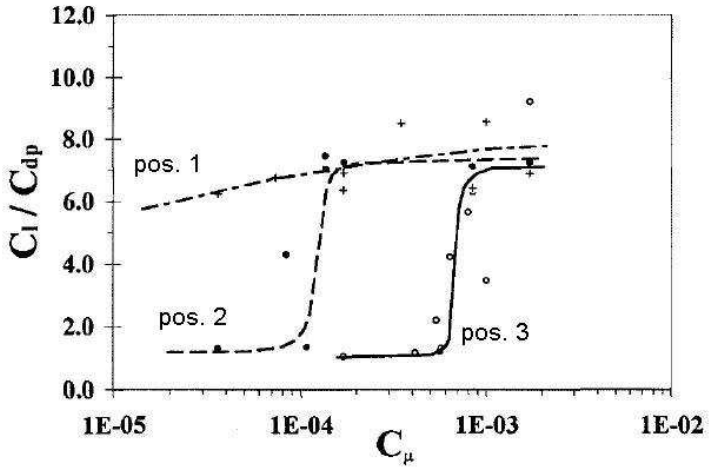

Figure 2.10: Influence of C_μ on performance improvement of a modified NACA 0015 [5].

of too low momentum fluid [11]. Therefore, for every flow/body configuration not only an adequate position must be sought but also the minimum and maximum limits for both the actuation level and frequency.

Influence of Reynolds and Mach Number

Seifert et al. [**?**] analysed the influence of two-dimensional active control (slots) on a NACA 0015 in very low and very high Reynolds number regimes, namely $30.000 \leq Re \leq 150.000$ and $2 \times 10^6 \leq Re \leq 4 \times 10^7$. They tested first passive control using turbulators (tabs) with different diameters at different positions over the airfoil surface. They realized that for very low Reynolds numbers passive control is almost unfeasible while oscillatory excitation at $f^+ = 1{,}0$ postponed the separation and increased the lift by a factor of 4. However, reducing the Reynolds number down to 30.000 the necessary momentum coefficient had to be quadruplicated to achieve the same performance the airfoil had at $Re = 50.000$. This is related to the fact that laminar boundary-layer at low Reynolds number are very stable and less susceptible to perturbations.

At high Mach numbers, $Ma > 0{,}3$, compressibility effects begin to play an important role as shock waves occur. They cause abrupt pressure increase, thickening the boundary-layer - the pressure increase works as an adverse pressure gradient - what may yield to separating. Seifert et al. examined the effect of compressibility and noticed that for Mach numbers above $Ma > 0,4$ the form drag increases with the use of active control and that the lift was reduced at pre-stall angles of attack.

Chapter 3

Experimental Methods and Facility

This chapter describes the facility and the experimental methods used in the present work. First, the wind tunnel, the airfoil and the development of the actuation system are described. Second, the experimental methods are presented, namely Static Pressure Measurement, Hotwire Anemometry and Particle Image Velocimetry. Last, data reduction and uncertainty analysis are discussed.

3.1 Facility

3.1.1 Low Speed Wind-Tunnel

The low speed open wind tunnel used for the current experiments was reported by Schröder [**?**], Pfeil and Orth [**?**] and Orth [**?**]. Air is supplied by a 620 kW radial compressor, delivering a volume flow of up to $20 m^3/s$. The test section is 0,95 m high, 0,45 m wide and 1,0 m long. The flow velocity can be adjusted between 2,0 m/s and 38,0 m/s - whereas a by-pass is available to achieve lower velocities. The turbulence level changes slightly with speed in the 0,6% to 1,0% range. To monitor the air flow during the experiments a Pitot-static tube is mounted in the entrance of the test section as well a thermometer. The figure 3.1 presents the wind tunnel dedicated for boundary layer research at the Technische Universität Darmstadt, shown are: 1) Airfoil and lateral transparent window, 2) Hot-wire traversing rod, 3) Particle Image Velocimetry (PIV) laser head, 4) Settling Chamber, 5) Seeding Section for PIV and 6) By-Pass opening to reduce the mass flow in the test section. The wind tunnel has a rotating wake generator located immediately upstream of the test section, which permits bars or wires to be mounted on it to simulate

the effect of incoming wakes from rotating rows present in real turbomachinery stages.

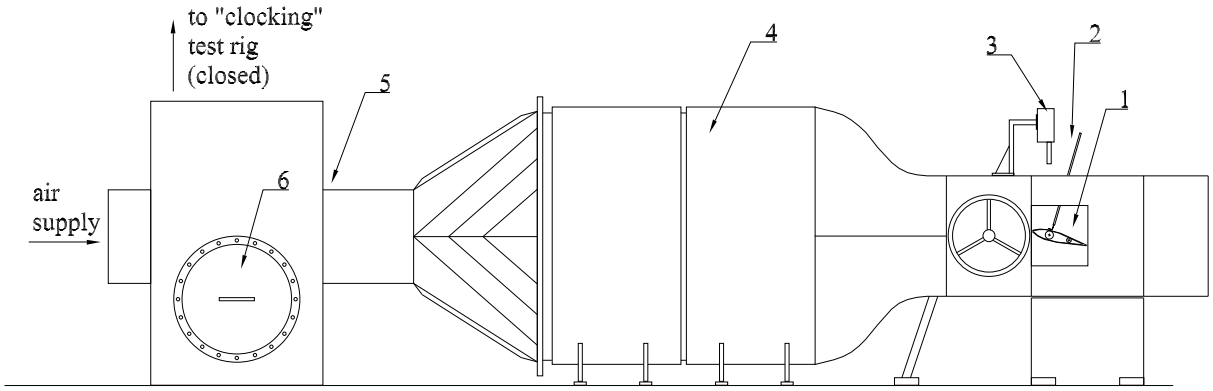

Figure 3.1: Low Speed Wind Tunnel at TU-Darmstadt.

3.1.2 NACA 63_3-018

A modified NACA 63_3-018 airfoil was adopted to investigate the active flow control (AFC) system. The choice was based on the work from Wang at the institute [7] and on available data from open literature [3]. The optimal set-up pointed out by Wang was adopted as the starting point for the current pulsating jet system configuration. The airfoil span and chord were $s = 0{,}45$ m and $c = 0{,}37$ m, respectively. The relative great size of the airfoil resulted in a high spatial resolution for boundary layer traversing. However, due to its low aspect-ratio ($s/c = 1,2$) it is a good practice to limit the flow study to the mid-span region in order to avoid the perturbances caused by the growing of the boundary-layer on the wind-tunnel walls around the airfoil fixation. Seventeen pressure taps are located on the suction surface and 20 on the pressure surface, they were placed in a "zig-zag" fashion in two parallel rows distant 15 mm from each other. This positioning minimizes the influence of taps on the measurement taken by taps placed downstream. The alignment of the airfoil with the flow ($\alpha = 0°$) was indicated when the pressure difference from two symmetric taps was zero. More details about the actuator are presented in the next section.

3.1.3 Actuator

The actuation system is a set of elements dedicated to disturb the flow in a controlled manner. It consists of an actuator, a solenoid valve, a function generator, a manifold and a compressed air supply. The manifold distributes compressed air into the actuator, which is than injected through a slot located at the airfoil's suction surface into the boundary layer. A high speed Festo MHE-4 solenoid valve was built in the system to promote the pulsating jet effect as the valve closes and opens continuously. A function generator permitted a stepless adjustment of the actuation frequency from 0 Hz (valve fully open) to 280 Hz. The mass flow was controlled indirectly using a spherical valve and a Keller pressure sensor series 23 PAA-23/8465.1 installed in the air line, the pressure sensor reading is directly and linearly proportional to the air line static pressure. The opening of the spherical valve raises the air line pressure and air jet velocity at the slot exit. During the solenoid valve operation resonance waves propagate in both directions; to the actuator and to the pressure sensor. To avoid disturbance in the pressure sensor reading a sealed tank was installed between the solenoid valve and pressure sensor to serve as a resonance damper (see Fig. 3.2).

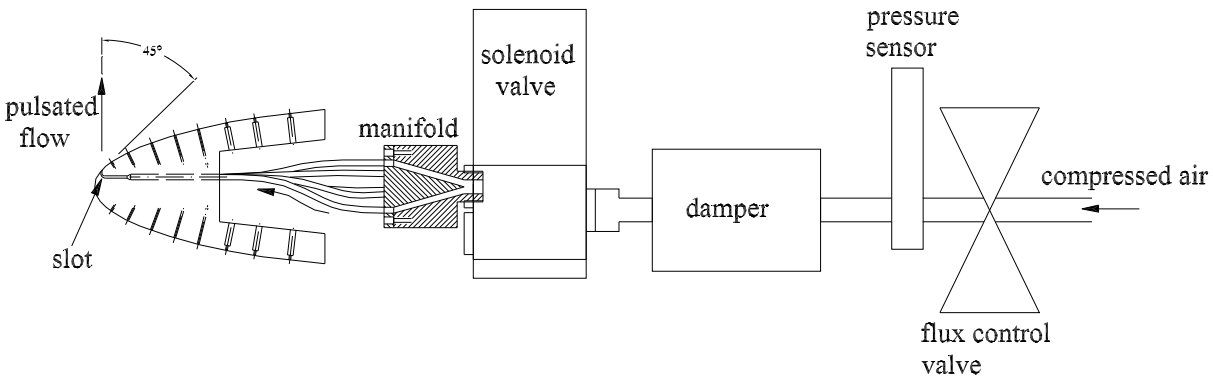

Figure 3.2: Components of the actuator system.

During the development of the actuator a prototype was first built and tested to optimize its internal design and to ensure that the air flow pattern would be adequate. The primary concern was to guarantee a homogeneous air flow distribution along the slot

length and that the air jet had components only in the X and Z directions (see Fig. 3.3 for wind tunnel coordinate definition).

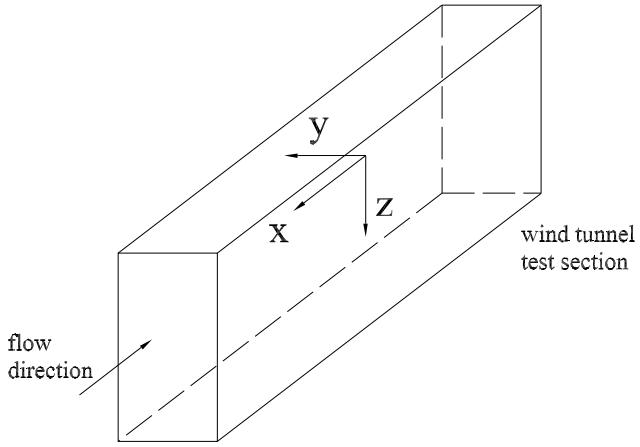

Figure 3.3: Wind tunnel coordinate system.

The prototype's slot had a yaw angle of 20°, width $w = 0{,}5$ and length $l = 100{,}0$ mm. The prototype allowed 3 different types of air supply connections (see Fig. 3.4). First an air hose was connected laterally directly at the first mixing chamber (B) from which the air was directed through small internal passages (not shown) to the slot (A). The purpose was to use the smallest mixing volume to minimize the pulsation attenuation. When the air hose is connected to port (C) the air flows through both chambers, maximizing the flow mixing, however with greater pressure loss penalty.

The air flow pattern could be checked using cotton tufts at the slot exit, which indicated a strong component in the Y direction. Closing port B and connecting the air hose to port C, improvement was gained but the presence of a Y component in the air jet outflow still evident. It is important to stress that at this point the ports D did not exist.

To solve the air maldistribution an air manifold was fabricated (see Fig. 3.5) and the ports D were opened at the rear part of the prototype. The manifold consisted of a cylinder with the air hose supply connection at one side and 15 small tube connections at the other side. Internally a cone was included to minimize the damping of the pulsation effect, since it forms an annular channel and the air flows smoothly. Visualisation with cotton tufts has shown that the Y component was supressed. At this point a definite internal design was chosen for the actuator. As the great difference was due to the insertion of the air manifold and to the more convenient air supply from the rear side and not due to the presence of two internal chambers, one chamber was eliminated in the definitive geometry

to avoid unnecessary pressure loss.

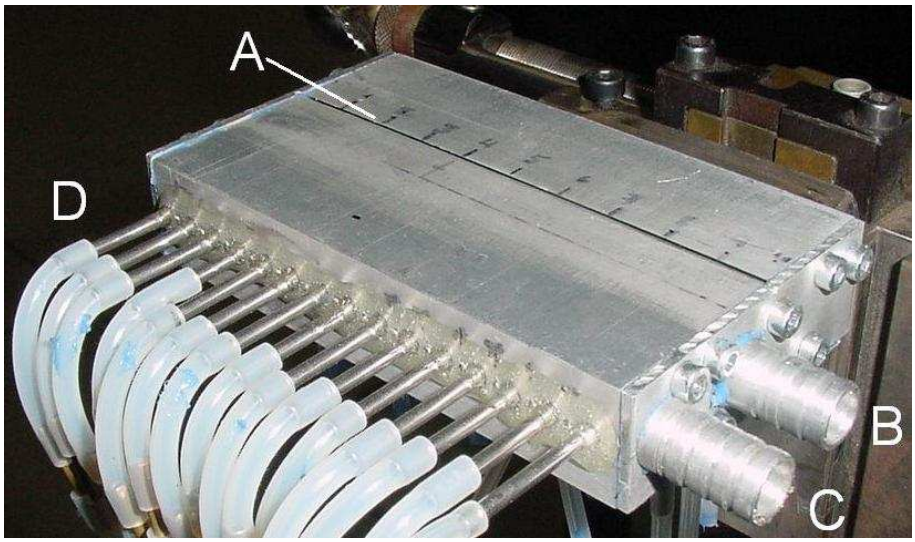

Figure 3.4: Actuator prototype.

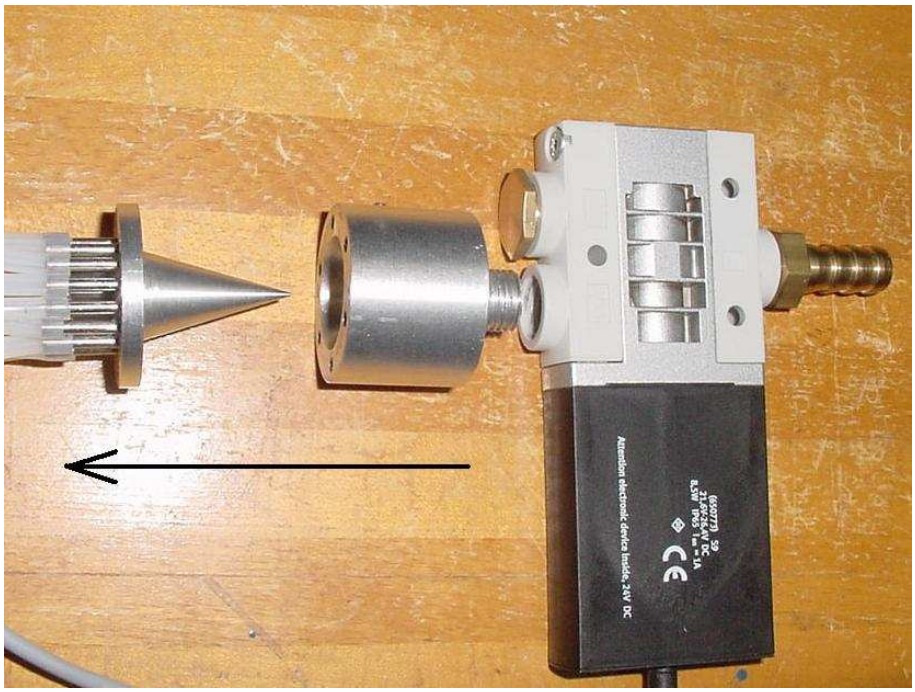

Figure 3.5: Air manifold and solenoid valve - arrow indicates flow direction.

The actuator assembly in the airfoil is shown in the figure 3.6. Considerations were taken regarding the slot position and dimensioning. As pointed out in the literature review, the closer the injection is to the separation, less energy is necessary to control the flow - consequently a more efficient system is built up [5, 7]. Experiments with China

clay were conducted to study the formation and the development of separation bubbles, and the formation of a small separation bubble between 1% and 2% of the chord (see Fig. 3.7) was perceived. Therefore, it was decided to place the injection slot at 0,7% of the chord, just before the bubble. Rapid prototyping permitted the manufacturing of an actuator with complex internal geometry. However, to keep the dimensional tolerances within an acceptable level, the actuator covered only 1/3 of the airfoil span (150 mm), the air injection outlet (slot) dimensions are $l = 100$ mm (length) and $b = 0{,}5$ mm (width) (Fig. 3.6). The main consequence of a limited slot length is that the air injection effect is restricted to the central area of the airfoil surface. For this reason, all measurement were made only at the vertical plane situated at the airfoil midspan.

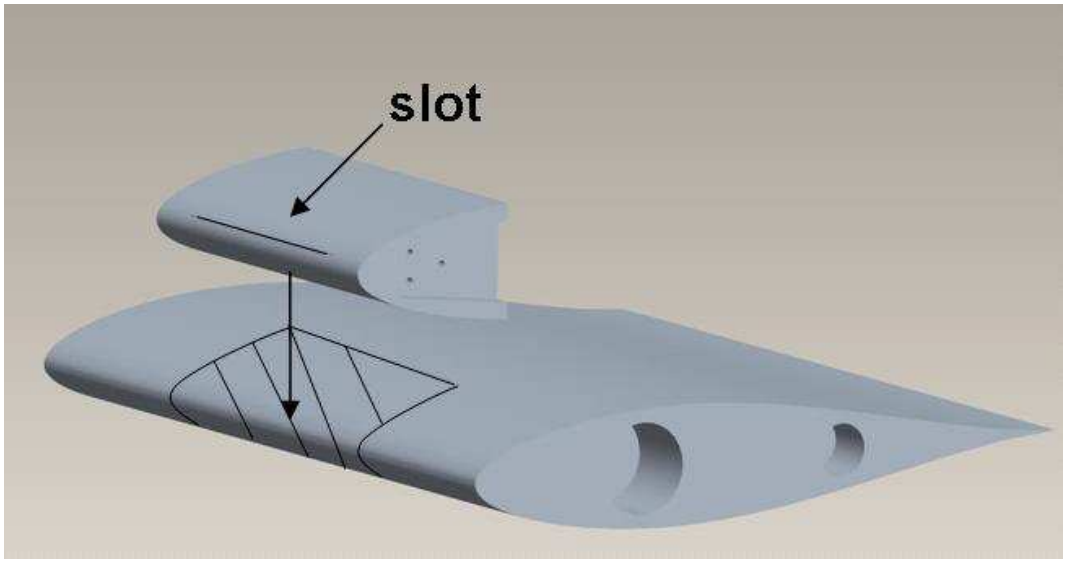

Figure 3.6: Schema of the installation of actuator in the airfoil.

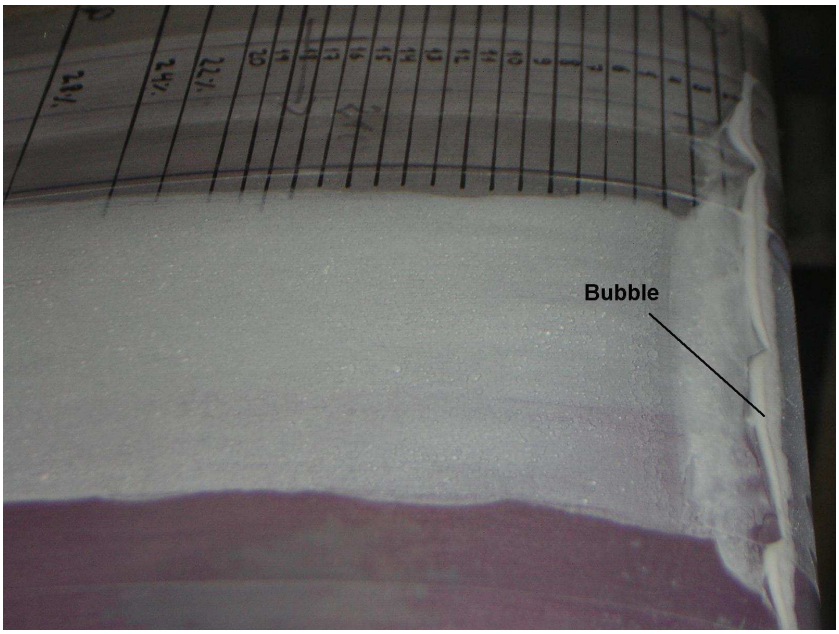

Figure 3.7: China clay visualisation, $Re = 100.000$, $\alpha = 16°$.

3.2 Experimental Methods

The experimental methods used in this work complement each other: measurement of static pressure distribution, hot-wire anemometry and particle image velocimetry. The principles of the measurement techniques employed are described below to corroborate their applications.

3.2.1 Hot-Wire Anemometry

Hot-wire anemometry (HWA) is widely used to measure flow velocity and temperature fields, concentration and phase changes in multi-phase flows [**?**]. HWA works by capturing the variation of electrical resistance of one or more fine tungsten wires exposed to a flow, due primarily to the effect of convective heat transfer. Assuming that pressure and temperature are kept constant, flow velocity is the only responsible for affecting the heat transfer and therefore the electrical resistance of the wire. Thus it is possible to set up a relationship between electrical current and flow velocity through a controlled calibration process.

Low cost, high frequency response and small size, thus less interference, are some of the characteristics that permit HWA to survive until the present days. In terms of accuracy it is equivalent to LDA, about 0,1-0,2% in well controlled experiments to 1% in most

experiments.

There are two basic modes of HWA operation: constant current anemometry (CCA) and constant temperature anemometry (CTA). In CCA the electrical current through the sensor is kept constant and the voltage variation is recorded. In this mode the velocity sensibility is negligible and the system is used to measure temperature variation. In CTA mode the probe is connected to an electrical circuit with a build-in feedback differential amplifier that keeps the wire resistance and the temperature constant - CTA mode is used for velocity measurements. Temperature variation during flow measurement is a significant source of errors. One can correct for this variation either by keeping the overheat ratio (a) constant, i.e. a is kept constant during calibration and during data acquisition. A third alternative is to connect an special type of probe called *Temperature Compensation Probe* to the CTA bridge to provide automatic compensation in nonisothermal flows.

HWA has restrictions as well; a wire is not sensitive to the flow direction, it is therefore not possible to capture reversal flows without the use of some special technique. Bruun [**?**] presents some alternatives to overcome the flow reversal measurement limitation by using shielded single-sensor, the cylinder-wake sensor or the flying wire technique. Additionally a single wire is only able to capture flow magnitude; if the components of the velocity are to be measured a composition of wires is necessary. Hence, a single wire is useful mainly when the direction is known beforehand or when the magnitude itself is the important parameter.

During an experiment the probe can be contaminated by small airborne particles, that modify the relation established during the calibration. It requires a repeated process of calibration and is often time-consuming. The fine tungsten wires break very easily if the particles are too heavy or simply due to wire material fatigue. In boundary layer measurements with hot-wires the most critical handicap of this technique is the increase of heat transfer ratio due to the approximation to conducting surfaces - in those cases, correlations may be used to correct the measured values [**?**] and/or a less conductive material should be used in the surface. Those issues are addressed below and the system used in the laboratory is described.

Hot-Wire Probes

A wide range of hot-wire and hot-film probes types is available, each suitable for a certain application. Wire probes are more fragile than film probes and are used for air and gas flow, the later type withstands better more aggressive ambients and liquid flows as well. The probes have usually one, two or three wires (see Fig. 3.8), their direction sensitiveness is proportional to the number of wires: probes with two wires, called *X-probes*, capture two-dimensional flow within +/- 45° range relative to the probe axis, tri-axial probes measure all velocity components inside a 70° cone around the probe axis.

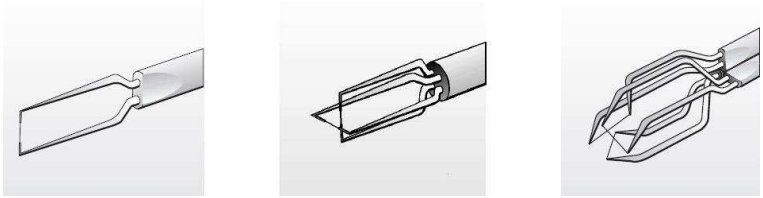

Figure 3.8: Probe types: single-sensor, X-probe and tri-axial probes (Dantec Catalogue).

To avoid aerodynamic interference on the prongs the probe axis shall be placed parallel to the flow direction. In the cases where space is limited or in boundary layer measurements, other types of probes may be necessary. The figure 3.9 shows a perpendicular sensor (Dantec 55P14) and a boundary layer sensor (Dantec 55P15), the former was used in all boundary layer measurements in the current work.

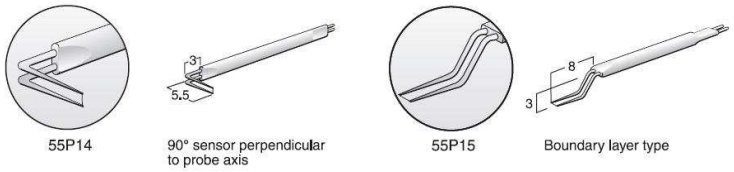

Figure 3.9: Boundary layer probes (Dantec Catalogue).

Hot-Wire Acquisition System

A Dantec 55P14 sensor was used for boundary layer surveys connected to a DISA Anemometer (55M01) and a DISA signal conditioning unit with a filter and amplifier built-in. The hot wire was positioned in the measurement section using a computer controlled 3-axis traversing system. The smallest vertical step (perpendicular to streamwise direction) is

0,1 mm with +/- 0,01 mm accuracy. A RSF-Eletronik encoder provided the actual position after the move command and the probe travelling, in this way all the uncertainty due to mechanical system gaps and looseness vanished and only the encoder uncertainty remained. To exemplify: suppose the probe was sent to a virtual position "10.2 mm", due to the above mentioned mechanical uncertainties the true position does not really matches 10.2 mm and one has to consider the uncertainties. But if the position was read again after the movement, only the encoder uncertainty has to be considered: a command "read" would result e.g. in "10.32 mm". Then one knows that due to the mechanical gaps the probe did not travel to 10.2 mm but one knows it is at 10.32 mm ± 0,1 mm, what greatly reduces the final uncertainty.

A fine conductive metal pin installed parallel to the hot-wire probe was used to detect the surface approximation and avoid collision. Over the airfoil surface a strip was painted with conductive material to short-circuit the traversing system when the metal pin touches the surface. A careful adjustment was performed to set the distance between the metal pin tip and the tungsten wire, that was the smallest distance the wire could come close to the surface, in the current experiments the distance was set to 0,10 mm.

The same function generator that controls the solenoid valve of the actuation system was used to trigger the HWA measurements. Hence all hot-wire data recording was synchronised with the valve, since the recordings started when the valve was at the very same position. It permitted the computation of ensemble averages from HWA data (section 3.3).

Heat Transfer Model

All heat transfer types are present in HWA; radiation, conduction and convection, however radiation contributes with only 0,1% of the heat loss while conduction with approximately 15%; both types are neglected in the modelling of heat transfer process in hot-wire and hot-film probes. Convection is quantified by the Nusselt number Nu, which for air flow application at moderate velocities between $0,02 < Re < 44$ can be simplified to $Nu = f(Re)$. The relationship given by equation 3.1 is known as King's law, where A and B are empirical constants derived form probe calibration, $n = 0,45$ provides a good fit for most applications [**?**]. The relationship assumed by the King's law can be converted to correlate the probe output voltage with the magnitude of flow velocity, Eq. 3.2.

$$Nu = A + B\,Re^n \tag{3.1}$$

$$E^2 = A + B\,u^n \tag{3.2}$$

Hot-Wire Calibration and Data Conversion

The hot-wire probe was calibrated in the wind tunnel at the inlet plane of test section where all measurements were performed. This approach brought two main advantages: first, it avoided great time expenditure from mounting the probe in a calibration rig and afterwards in the wind tunnel - it would require also that the HWA bridge and all the cables to be transported from one rig to the other. Second, and most important for the results accuracy, no errors were caused due to misalignment between the probe and flow, resulting from changing the flow direction and probe axis when the probe is mounted in two different rigs. In the particular case of the present laboratory, the calibration rig is not suitable for the present measurements because it does not blow at low speeds, necessary for boundary layer measurements. At the calibration section in the wind tunnel a Pitot-static tube was placed very near the hot-wire probe, but far enough to not disturb the flow. Both hot-wire and Pitot-static signals were acquired simultaneously as the flow velocity was varied in the wind tunnel. The flow velocity at the calibration section was calculated directly from the difference of total and static pressures using equation 3.3 so that it was possible to correlate hot-wire output voltage with flow velocity. For every calibration at least 15 points were acquired at different flow velocity, each one recorded data during 16 s.

$$u = \sqrt{\frac{2(p_0 - p)}{\rho}} \tag{3.3}$$

Bruun compared different fit curves for hot-wire calibration data and recommended King's law, third-order polynomials in terms of E^2 and fourth order polynomials in terms of E; the accuracy lays between 0,1 and 0,15% [**?**]. The last fit, equation 3.4, was adopted to calculate the calibration curves in the present work.

$$u = A + BE + CE^2 + DE^3 + FE^4 \tag{3.4}$$

Boundary layer measurements require special care during calibration at low velocities. In the current test rig velocities down to about 2 m/s were achieved opening the wind tunnel by-pass, so that part of the air flow blown by the centrifugal compressor vented

directly to atmosphere. In order to include lower velocities in the calibration curve and to correct for heat transfer due to proximity to the airfoil surface, the hot-wire probe (Dantec 55P14) was placed 0,1 mm from the surface and a circular cap surrounded it to protect from air streams. Under this condition the "velocity zero" probe output voltage was recorded. The figure 3.10 presents a typical calibration fit and the points recorded, the calibration was performed from low to high flow velocity and vice versa to take any hysteresis into account.

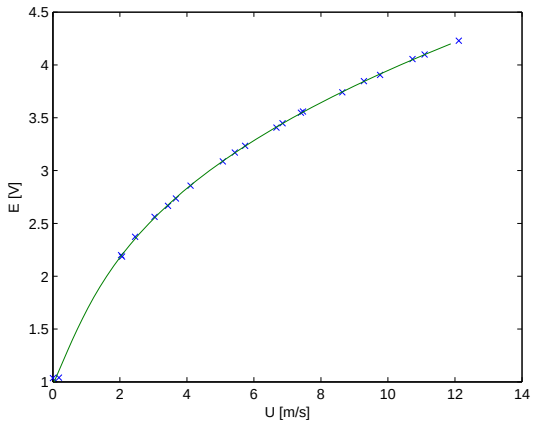

Figure 3.10: Hot-wire calibration points and a 4th order polynomial fit.

Before the continuous analogical signal from the hot-wire probe was converted to discrete digital values by the 12-bit A/D card, adjustments were made in order to use the whole range of the digital card: from 0 to 4095. The output of the probe was typically in the range 3,0 V to 4,5 V while the input of the A/D card was 0 to 10 V. If the small amplitude signal from the probe would be supplied directly to the card, it would result in a signal resolution limitation, since only about 600 integer values of the card would be used. To overcome this issue, the signal-conditioning unit amplified the signal with an offset adjustment, so that the originally 3,0 V probe output signal corresponded to about 0 V input to the card and the 4,5 V corresponded to about 10 V.

3.2.2 Particle Image Velocimetry

Particle Image Velocimetry is a non-intrusive technique that acquires information from a whole flow field in an instant of time. A laser sheet forms a measurement plane while particles carried by the flow reflect the laser, which in turn is captured by a digital camera placed in the perpendicular direction of the plane. Typical modern PIV capture

two consecutive laser beams, the second beam flashes after a pre-determined time interval Δt form the first beam. The particles reflexions (in other words, the particles positions) are recorded in two instants of time and the velocity can be calculated. Since PIV is not a particles tracking system, a mathematical algorithm is used to estimate the velocity magnitude and direction.

Modern digital PIV systems are composed of a dual-cavity Nd:Yag laser [1], a digital CCD- or CMOS-camera and a computer unit that synchronises laser and camera. The figure 3.11 depicts how the PIV devices are placed in a test rig, this one is identical to the one installed in the wind tunnel.

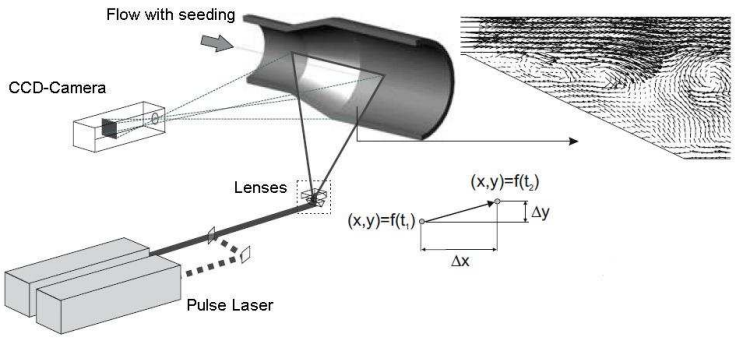

Figure 3.11: PIV system and the calculation of velocity [**?**].

The way the digital camera records the images generated by the laser pulses (bursts) determines how the images will be analysed; either by autocorrelation or by cross-correlation. Autocorrelation is performed when a single frame is exposed twice (double-exposure). In this case temporal information is not available and it is not possible to determine the exposure sequence, thus only the velocity magnitude can be calculated. This technique became obsolete with the introduction of faster and more affordable digital cameras that permit double exposure to be recorded in two distinct frames. With the chronological information available a cross-correlation algorithmic is able to determine both velocity magnitude and direction.

The main constraint of PIV systems is temporal resolution limited by the laser cavity pulsation frequency. The dual-cavity Nd:Yag laser used provided 50 mJ pulses with wave length of 532 nm (green laser) at 15 Hz in each cavity, resulting in a maximum acquisition rate of 30 Hz. Copper lasers provide pulsing frequencies of up to 50 kHz with only fractions of mJ, it can be used for faster acquisition rate records but limited to very

[1] neodymium-doped yttrium aluminium garnet crystal, $Nd : Y_3Al_5O_12$

small measurement planes. Modern neodymium-doped yttrium lithium fluoride (Nd:YLF) lasers are likely to overcome the limitation of PIV, allowing frequencies of few kHz, which combined with modern fast speed CMOS-sensor cameras form the *Time-Resolved* PIV, permitting higher temporal resolution in a large measurement field [**?**].

The camera sensor (PIV's measurement probe) is subdivided in small rectangular fields called interrogation areas (IA), where M_{int} and N_{int} are the number of pixels from each side (usually $M_{int} = N_{int}$). The spatial resolution of PIV depends on the ratio between the real measurement field and camera sensor, known as "scale factor" (S), on the CCD-sensor design (distance between pixels) and the interrogation area. The IA can be set as squares with sides of 16 $\times$ 16 pixels up to 128 $\times$ 128 pixels, always in multiples of 16 pixels. Once the field of view is selected and the camera is fixed, the dimensions of the IA have to be defined, seeking a compromise between signal-to-noise and the desired range of velocity to be captured: smaller IAs increase the spatial resolution while greater IAs increase the measurable range of velocity.

Autocorrelation and cross-correlation are statistical tools and have two pre-requisites to provide valuable results: first, a minimum number of samples, i.e. a minimum number of "record pairs" each resulting in a flow field. Once a significant number of pairs are recorded by the camera an average mean can be derived resulting in the final flow field. Second, it is necessary to have enough particles in an IA to keep a high signal-to-noise ratio (usually 5 to 12 particles, depending on processing method). The larger the IA, the higher the maximum velocity possible to be captured, because a particle will be able to travel a longer path in a given Δt. However, increasing the IA area, decreases the spatial resolution and a compromise has to be found.

The first verification criterion of the chosen IA area is that the particles images displacement shall not be greater than 1/4 of IA's side (S). The equation 3.5 was used to verify this requirement. A PCO Sensicam CCD-Camera with 11,520 mm $\times$ 9,216 mm sensor with 1280 $\times$ 1024 pixels resolution was employed, whose pixels' size d_{pixel} = 9,0 μm. A maximum velocity of u_{max} = 18 m/s was assumed, while the IA dimensions were set to 16 $\times$ 16 pixels and the time between two consecutive bursts was Δt = 0,25 μs. The maximum permissible displacement would be 0,036 mm but at the assumed u_{max} it would not exceed 0,022 mm, permitting in fact to measure velocity of up to 29,5 m/s to be captured with reliability.

$$d_{max} = \frac{u_{max}\, t}{S} \leq \frac{N_{int}\, d_{pixel}}{4}, \tag{3.5}$$

Every pixel displays grey levels (a 8-bit sensor has $2^8 = 256$ levels), according to the grey level the position of a particle is identified. The cross-correlation algorithm compares the grey levels of two consecutive frames, resulting in the figure 3.12, whereas the displacement is represented by the highest peak.

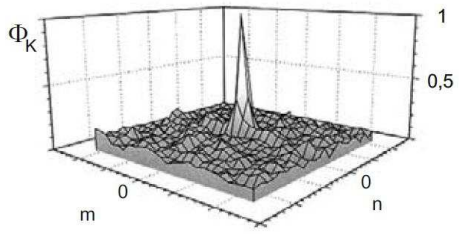

Figure 3.12: Result of a cross-correlation calculation algorithm [?].

There are some pre-requisites on particles in order to PIV to work: an sufficient quantity of particles has to be seeded, the particles must have a density similar to the one of the flow media and its size must adjusted in order to reflect enough light to at least 2 pixels of the camera sensor, on the other hand it has to be small enough to avoid buoyance and inertia effects.

A standard Safex fog fluid and a Safex fog generator 2001 were used to seed particles with 1,07 μm mean diameter. The particles were supplied in the seeding section (Fig. 3.1) so that the travel distance inside the wind tunnel was enough to diffuse the particles in the air providing an uniform particle distribution at the PIV measurement plane. The laser head was placed on the top of the tunnel to project a vertical laser plane, whose normal vector was perpendicular to the tunnel axis. Through the transparent lateral window the scattered light reflected by the particles reached the CCD-camera.

As it can be seen in the PIV results, only part of the airfoil was covered as the measurement field; the frames were limited to cover from the leading edge to 60% of the chord. A compromise had to be found, since projecting the laser across the whole airfoil resulted in weak laser power density that did not sensitize the sensor's pixels.

Similar to the HWA, the PIV was triggered by the same function generator that controls the actuator's solenoid valve. It was possible to capture multiple records of the interaction of the flow field and the pulsating air jet at pre-determined time instants, relative to the start pulse sent to the solenoid valve. Within an actuator cycle, 5 time

instants were recorded, namely at $t/T = 0$; 0,20, 0,40, 0,60 and 0,80. For each one a total of 30 double-exposures were acquired and average cross-correlations provided the definitive flow field picture.

3.2.3 Static Pressure Distribution

Static pressure distribution is an important information for the design of devices that interact with flows, e.g. wings, fuselages, blades, cars, oil platforms, bridges, etc. It provides means to calculate forces and velocities and to assert the condition of boundary layers.

Pressure taps are widely used to measure static pressure distribution, though its simplicity, it is a reliable and established method. There is a much more sophisticated method, called pressure sensitive paint (PSP), which consists in covering the model with a paint layer that changes the wave length of reflected light according to the local pressure. Data acquisition is performed by CCD cameras, whose images have to be carefully calibrated to correlate the colours with the corresponding pressure level. This method provides continuous information of pressure distribution in opposition to pressure taps and suppresses all tap-cabling necessary, what can be inconvenient in larger wind tunnel models.

From the pressure distribution one asserts the probable type of boundary layer flow, the location of maximum and minimum pressures and their strength, the maximum velocity, the position of highest velocity and also the centre of pressure location [**?**]. The pressure is normalized by the dynamic pressure of the free-stream as shown in equation 3.6, therefore $C_p = 1$ means that at this location the pressure has the same value as the total pressure and is thus a stagnation point.

$$Cp = \frac{p - p_0}{1/2\,\rho\,u_\infty^2} \tag{3.6}$$

Pressure taps are installed in the present model to obtain the pressure distribution, the tap-cabling in shown in the figure 3.13. The orifice diameters must be small and free of imperfections and burrs to keep the interference with the boundary layer at acceptable levels. A rough rule is to drill the orifices with approximately 1/5 of the local boundary layer thickness to reduce the distortion on the flow streamlines. Depending on the size of the model the orifice diameters usually range from 0,25 mm to 2,5 mm. Orifices with 0,8 mm diameter were drilled in two parallel rows (distribution is presented in section 3.1.2) and were conected to a Scanivalve.

Figure 3.13: Pressure taps cabling of the NACA $63_3 - 018$ airfoil.

The technique is suitable for steady flows because the time response is slow and unsteady phenomena cannot be resolved. Therefore the unsteady flow caused by the use of active control (pulsed jets) can not be captured by this technique, however a mean value of the pressure distribution results if the pressure is recorded for long period of time relative to the time scale of the pulsation, which is 0,1 s for the slowest pulsation frequency adopted (10 Hz). Therefore, the pressure was acquired for 16 s at every tap. Due to the long hoses of small diameter that connected the taps to the Scanivalve, the pressure took about 3 s to stabilize when the Scanivalve changes the taps, hence a 4 s time interval was waited before acquisition starts.

3.3 Data Reduction

Experimental data may be either of periodic or random nature, though a pure periodic event is very unlike to occur. A practical example is the wake impingement from a rotor in steady operation over a stator; the wakes itself have periodic nature because the machine operates at constant frequency. But if the time interval between the wakes and their duration were measured, a variation would be noticed, even if small. The random component is thus twofold: this occurs due to rotor frequency oscillation and the uncertainty in the measurement chain. In this section the so called *phase-locked ensemble average* is presented as a tool to separate the periodic from the random component of a

signal. In the next section the uncertainty of the measurement chains are determined, whereas the uncertainties of the free-stream velocity, HWA and pressure distribution are determined.

All data acquisition was triggered by the function generator that controls the solenoid valve of the actuation system. This allows that signals captured at different instants to be superposed, so that data from different sample records can be correlated in respect to the time instant within the signal period. The figure 3.14 exhibits how data is divided in the ensemble average technique using a typical velocity run.

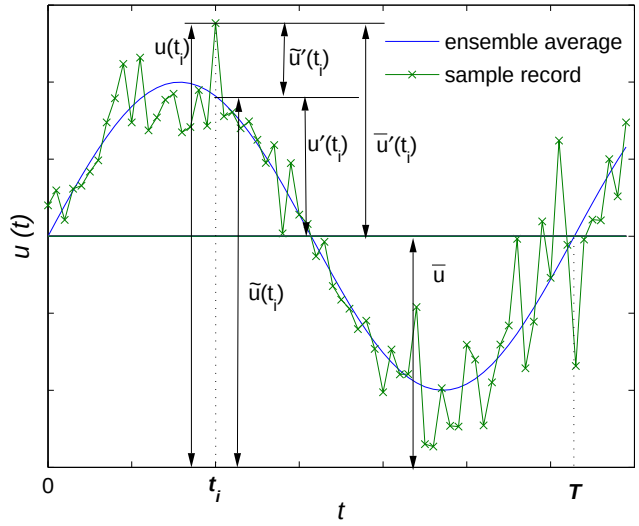

Figure 3.14: Description of a general experimental data component.

Signals are presented in two different forms: either from a single record sample or from an ensemble average. From a simgle record sample, the velocity *u(t)* is divided in mean value $\bar{u}$ plus the random component $\bar{u}'(t)$ (Eq. 3.7). However, this representation is not appropriated for signals containing an oscillation because it will be confused with turbulence and the resulting turbulence level will be wrongly too high.

For this kind of signals the ensemble average technique is more suitable. Assuming an event that occurs cyclically every 1 s a series of sample records are measured, for instance from time 0 to 30 s thus 30 samples. The 30 samples are then superimposed as if it where a single event but now 30 records are available for each time instant, what permits statistical analysis for each time instant to be performed. As indicated by figure 3.14 the oscillation can be clearly distinguished and the signal can be appropriately divided in ensemble value $\widetilde{u}(t)$ plus the corresponding random value $\widetilde{u}'(t)$, Eq. 3.8.

$$u(t) = \bar{u} + \bar{u}'(t) \tag{3.7}$$

$$u(t) = \widetilde{u}(t) + \widetilde{u}'(t) \tag{3.8}$$

The time-mean $\overline{u}$ is calculated using all data available in a sample record and is therefore a time-independent value. The equation 3.9 presents the calculation of mean value for a sample record (a discrete collection of data) with N values.

Ensemble mean is a time-dependent value that uses a series of M sample records each with N samples values, in other words there will be M measurement series each with N discrete values. The ensemble mean is calculated for each one of the N time instants using M values, as expressed by Eq. 3.10. To illustrate this procedure the data run presented in Fig. 3.14 can represent a typical flow velocity disturbed by the pulsating jet in one fixed point within the flow field. The continuous line represents the ensemble average, which is a time dependent mean value.

However, for the current data reduction the suggestion from Orth [**?**] is followed, whereas a "smoothening" is performed by averaging the ensemble mean of 4 neighbour points. The need of such procedure lays in the impossibility of perfectly synchronise the sample records due to instrumentation imprecision. The equation 3.11 expresses how the calculation is performed. The drawback of smoothening is the reduction of time resolution by a factor equal the number of neighbour points used; in the current work reduction is reduced by a factor of four.

$$\bar{u} = \frac{1}{N}\sum_{j=1}^{N} u_j \tag{3.9}$$

$$\widetilde{u}(t) = \frac{1}{M}\sum_{j=1}^{M} u_j(t_i) \tag{3.10}$$

$$\widetilde{u}(t) = \frac{1}{4M}\sum_{j=1}^{M}\sum_{k=4i-3}^{4i} u_j(t_k),\ i = 1, ..., N/4 \tag{3.11}$$

It must be clearly stated that ensemble average was performed only for HWA data. The number of samples was fixed to 20.000 and the HWA rate was set to 5 kHz resulting in a 4 seconds acquisition time. Therefore, the number of cycles used in the calculation of ensemble average quantities was related to the pulsating frequency *f*, table 3.1 presents the number of cycles recorded for each pulsation frequency used during the experiments.

Table 3.1: Actuation cycles recorded for each actuation frequency (f_{acq} = 5 kHz)..

f **[Hz]**	**M (cycles)**	**N (samples)**	t_{acq}
10	40	20.000	4 s
25	100	20.000	4 s
50	200	20.000	4 s
100	400	20.000	4 s

3.4 Uncertainty Analysis

Data acquisition is performed through a measurement process and is prone to errors since it is the physical realization of an ideal process or measurement method.

The observed value of a variable will probably differ from its true value, the difference of the observed value and true value is the error, which is of course never known in advance. However, the error can be statistically estimated through the determination of inaccuracy or uncertainty of a measurement [**?**]. The uncertainty can be decomposed in bias (B) and imprecision (I). Bias is the systematic error, which is part of the measurement process and is always present in the read value as a repeating error. Imprecision it the random part of error, it is responsible for the non repeatability of measurements. The measure of imprecision is given by the *precision limit* P. The estimate of uncertainty U is calculated by

$$U^2 = \underbrace{P^2}_{random\ error} + \underbrace{B^2}_{systematic\ error}$$

An appropriate form to present uncertainty of a variable x is to present a composition of its mean value $\overline{x}$, the uncertainty interval U and the probability ξ that a variable falls within the given interval

$$\overline{x} \pm U(\xi\%)$$

Assuming a Gaussian distribution as an appropriate distribution around the mean value the uncertainty bonds can be expressed as multiple of the estimate of the standard deviation s (Eq. 3.12). The bonds determined by the multiples of s are: $\pm s$, $\pm 2s$ and $\pm 3s$ which correspond to probabilities of 68%, 95% and 99,7%, respectively.

$$s \triangleq \sqrt{\frac{\sum_{i=1}^{n} [x(i) - \overline{x}]^2}{n-1}} \tag{3.12}$$

In the estimation of uncertainty bonds, one has to consider whether a *single-sample* or a *multiple-sample* experiment will be performed. A simple-sample experiment is the one that is performed only once. Multiple-sample tests are constituted of series of samples acquired from repeated tests performed under the same conditions. The bias error is calculated in the same way for both single-sample and multiple-sample tests, whereas the precision limit is calculated by a particular procedure for each type of test.

A measurement system consists of a series of instruments, procedures for data acquisition and data reduction and operational environment. The result r of an experiment is obtained using data from m variables: $r = r(x_1, x_2, ..., x_m)$. A meaningful estimate of the result uncertainty has to consider the propagation of uncertainties related to each variable involved in the calculation of r, the figure 3.15 shows the propagation of individual uncertainties until they collapse in the general uncertainty of the result (originally from AIAA (1995), see Stern et al. [**?**]).

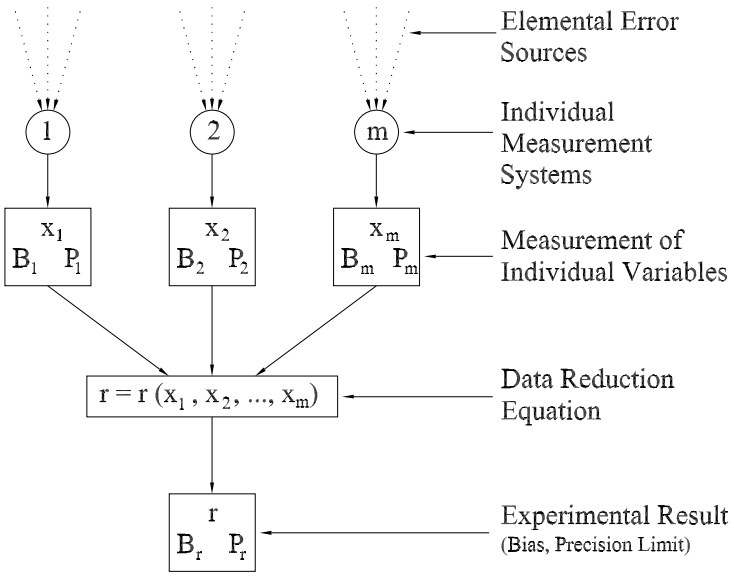

Figure 3.15: Propagation of uncertainty in the calculation of an experimental result [**?**].

The error due to bias is determined from calibration and can thus be eliminated [**?**], however in certain circumstances it is not possible because the calibration is performed in one calibration rig and afterwards the instrumentation is displaced to the test rig, where the data will be acquired. In this case the bias errors shall be estimated with the best available information and through analytical estimates and previous experience.

Kline and McClintock [**?**] compared three methods for the determination of the uncertainty limits resulting from the propagation of imprecision limits in a measurement system (U_r) and concluded that the root-sum square formula (Eq. 3.13) provides the best results for the calculation of random errors.

$$U_r = \sqrt{\left(U_1 \frac{\partial r}{\partial x_1}\right)^2 + \left(U_2 \frac{\partial r}{\partial x_2}\right)^2 + ... + \left(U_m \frac{\partial r}{\partial x_m}\right)^2} \tag{3.13}$$

The values U_i are the uncertainties from each individual variables used in the data reduction to calculate a result. It should be stressed that the statistical limits, i.e $\pm s$, $\pm 2s$ and $\pm 3s$, must be the same for every component in equation 3.13. In the current work the uncertainty is estimated for free-stream velocity and Reynolds number, and hot-wire

uncertainty is assumed to be a composition of the following sources [**?**]:

- Instrumentation Error
- Calibration or Fit Error
- Measurement Error
- Miscellaneous Errors

The Instrumentation Error corresponds to those inherent to a specific measurement technique, usually the uncertainty limits related to those errors are declared by the instrumentation manufacturer or may be determined by a fine calibration [2]. The corresponding uncertainty is given by U_{inst}.

Calibration or Fit Error stems from curve fittings used to express the relation between true values and the read values. The uncertainty limits can be estimated using the least-square procedure. The corresponding uncertainty is given by U_{cal}.

Measurement Error corresponds to the variation of the true value during the measurement but inherent to the physical phenomenon. A typical example is the oscillation of flow velocity within a region of separation. This source of error is assumed to be absent during calibration of instruments. The corresponding uncertainty is given by U_{meas}.

Miscellaneous Errors are related to other sources of errors. They can be of systematic or of random nature and contribute to bias and/or to precision errors. The transfer of a hot-wire probe from a dedicated calibration rig to the test rig is a typical type of error source. Operator mistakes or change in the ambient pressure are both of random nature and are also included in this group. Estimate of those errors, i.e. the uncertainty limits, are often derived from previous results and experience. The corresponding uncertainty is given by U_{misc}.

The complete uncertainty is then asserted by root-sum square of the above mentioned sources:

$$U_{total} = \sqrt{U_{inst}^2 + U_{cal}^2 + U_{meas}^2 + U_{misc}^2} \tag{3.14}$$

The uncertainties of free-stream velocity, Reynolds number, pressure coefficient and velocity obtained from HWA are derived in the following sections, but before that it is necessary to determine the uncertainty associated with primary variables that are used to

[2] A calibration standard at least 10 times more accurate than the instrument been calibrated is necessary.

derive the above cited. In the next section the uncertainty of temperature and pressure are estimated.

Temperature

Temperature error was caused by two sources: 1) instrument error and 2) temperature variation within the wind tunnel during the experiments. A mercury thermometer was placed in the test section to measure the static temperature, whose uncertainty is assumed to be half of the smallest scale reading, $U_{inst} = \pm 0{,}5$ K (95%).

Once the instrument uncertainty is known, it is necessary to evaluate if the temperature variation is relevant because depending on the type of measurement it can be significant. Hot-wire calibrations took approximately 15 minutes, during this period of time no remarkable temperature change could be figured out. However, typical boundary layer measurements were performed at 7 stations along the airfoil and took about 2 hours. During the data aquisition in the wind tunnel the temperature varied usually by 4 K. Thus an uncertainty limit due to temperature variation was asserted to be $U_{meas} = \pm 2,0$ K, resulting in an uncertainty of $U_{temperature} = (0,5^2 + 2^2)^{1/2} = \pm 2,1$ K (95%) for boundary layer traversing and $U_{inst} = \pm 0{,}5$ K (95%) for hot-wire probe calibration.

Pressure

The error in pressure measurement is estimated considering the instrument and the calibration errors. A digital manometer Digima FP from Special Instruments as employed in all experiments. It features two operation ranges: ± 199,9 Pa and ± 1999,9 Pa. The manufacturer declares an uncertainty limit of ± 0,25 Pa of the full scale (absolute error) or $U_{inst} = \pm$ 0,5 Pa and $U_{inst} = \pm$ 5,0 Pa, for the smaller and the larger sensor ranges, respectively. In order to reduce the uncertainty limits of the digital manometer, it was calibrated against a Betz manometer reducing it to ± 0,1 Pa (95%).

Since data is not read directly from the manometer digital display but rather recorded by a A/D converter, a calibration was performed for both ranges to relate input (pressure) and output (voltage). The standard deviation of pressure s_{q_i} follows from

$$s_{q_i}^2 = \frac{1}{n} \sum \left(\frac{q_o - b}{m} - q_i^2 \right)$$

where n is number of samples, q_i is the input [Pa], q_o is the output [V], m and b are the angular and the linear coefficients of the linear fit, respectively. The resulting standard

deviation for the used range is approximately $s_{q_i} = 0{,}1$ and yielding an uncertainty of $U_{cal} = \pm$ 0,2 Pa (95%). The resulting pressure uncertainty is the sum of instrument and calibration uncertainties: $U_{press} = U_{inst} + U_{cal} = 0,2 + 0,1 = \pm 0,3$ Pa. It was assumed that the barometer used to measure the ambient pressure has negligible uncertainty.

3.4.1 Uncertainty of Experimental Results

Once the uncertainties of pressure and temperature measurements are determined, it remains to calculate the uncertainty of free-stream velocity within the wind tunnel test section, of the corresponding Reynolds number, of the pressure coefficient and of the velocity measured by hot-wire probes - which is done it next sections.

Free-Stream Velocity and Experiment Reynolds Number

The free-stream velocity at the test section is calculated through equation 3.3. It has to be stressed that velocity is not an experimental variable but rather an experimental result, that carries an error propagation from the individuals variables used to calculate it. When considering those variables, some assumptions have to be made due to the wide variety of events that may take place simultaneously.

When addressing the uncertainty of free-stream velocity 3 sources of uncertainty are taken into account, namely that from the manometer (determined to be $\pm$ 0,3 Pa in the previous section), from the Prandtl-tube and from centrifugal compressor rotational speed. The Pitot-static shows 1% uncertainty for misalignment of up to 10° [**?**].

The uncertainty due to variation of rotational speed is asserted in the following way: the free-stream velocity is adjusted before data recording and again when the recording is accomplished. For a typical nominal free-stream velocity of $u_\infty = 3{,}7$ m/s, a corresponding 8,1 Pa dynamic pressure is read by the Prandtl-tube. Comparing u_∞ before and after data acquisition, a variation of 0,4 % in dynamic pressure is figured out. For calibration rotational velocity variation is neglected.

Admitting a nominal free-stream velocity of $u_\infty = 3{,}7$ m/s, which corresponds to a Re = 90.000, the equivalent dynamic pressure is 8,1 Pa (from equation 3.3). The contributions due to manometer ($U_{instr} \pm$ 0,3 Pa), to Prandtl-tube ($\pm 1/100 \times$ 8,1 Pa) and flow oscillation ($\pm 0,4/100 \times$ 8,1 Pa) results in a dynamic pressure uncertainty of $U_{p_d} = \pm$ 4 Pa.

Before the uncertainty of free-stream velocity is calculated, it is convenient to present

the uncertainty of air density for short measurements (calibration) and long measurements sessions (boundary layer traversing). Air density is calculated through the relation $\rho = p_{amb}/RT_{amb}$, R is the gas constant R = 287,1 N m/kg K. The uncertainty of the density for short and long measurements sessions are $U_\rho = \pm$ 0,004 kg/m^3 and $U_\rho = \pm$ 0,02 kg/m^3, respectively. They are therefore neglected in the calculation of the resulting propagation error for the free-stream velocity calculated using equation 3.13:

$$U_{u_\infty} = \sqrt{\left(U_{p_d}\frac{\partial u_\infty}{\partial p_d}\right)^2 + \left(U_\rho\frac{\partial u_\infty}{\partial \rho}\right)^2} = \pm 0,08 m/s (95\%)$$

The uncertainty of the Reynolds number of an experiment results directly from the above discussion if it is assumed that the temperature influence on the viscosity is negligible. Repeating the above procedure for the Reynolds number, $U_{Re} = 2,7\%$, what yields to a Reynolds number of Re = 90.000 . Since the experiments were conducted at Re = 90.000 $\pm$ 2430 (95%).

Pressure Coefficient

For the calculation of uncertainty of pressure coefficient c_p (see Eq. 3.6) the following input is used: $U_{p_d} = \pm$ 0,3 Pa, $U_{u_\infty} = \pm$ 0,08 m/s and $U_\rho = \pm$ 0,02 kg/m^3. Assuming the nominal free-stream velocity u_∞ = 3,7 m/s, the maximum pressure difference is equivalent to the dynamic pressure, thus 8,1 Pa. The pressure coefficient results from:

$$U_{c_p} = \sqrt{\left(U_{p_d}\frac{\partial c_p}{\partial p_d}\right)^2 + \left(U_{u_\infty}\frac{\partial c_p}{\partial u_\infty}\right)^2 + \left(U_\rho\frac{\partial c_p}{\partial \rho}\right)^2} = \pm 0,055 \; or \; 5,5\% \; (95\%)$$

Hot-Wire Anemometry

Hot-wire calibration is often performed using dedicated calibration rigs. Though designed for this purpose, significant error can be added to the hot-wire measurements due to the probe transfer from the calibration rig to the measurement rig because the angle between the hot-wire probe and the air stream is very likely to be different in the calibration rig and in the wind tunnel and because the equipment used in the calibration rig is not always the same as in the wind tunnel, e.g. cable and anemometer bridge, since it may be impracticable in most cases. Those are bias error causes and are avoided when the hot-wire sensor is calibrated in the wind tunnel.

Especially in the assessment of hot-wire uncertainty there are many factors of influence, e.g. presence of particles in the air stream, change in the static pressure and humidity. However, in the present assessment it is assumed that only temperature change, calibration and velocity errors are accounted for. The mean change in temperature can cause about 2% error per 1 K, however the use of a compensation sensor reduces the error by one order of magnitude, thus 0,2% per 1 K [**?**]. The error due to temperature is estimated to be in the present case about 0,8 %.

Brunn [**?**] compared the errors caused by different curve fittings, whereas the fourth order polynomial used leads to an error of 0,15 %. When the velocity uncertainty is also considered ($U_{u_\infty} = \pm 2\%$), the resulting uncertainty for the velocity measured by the hot-wire is $U_{HW} = (2^2 + 0,8^2 + 0,15^2)^{1/2} \approx 2,2\%$. Table 3.2 depicts the resulting uncertainties of the measured variables.

Table 3.2: Uncertainty of measured variables.

Variable	**Uncertainty**
u_∞	± 0,3 m/s
Re	± 2430
c_p	± 5,5 %
u (hot-wire)	± 2,2%

Chapter 4

Calibration of the Actuator

Calibration was conducted with zero free-flow velocity to characterize the actuation system. The parameters that can be adjusted by the operator are the air mass flow, controlled by pressure ratio (pr), and the actuation frequency (f). The main goal of calibration is to evaluate the ratio between c_μ and c'_μ which are related to the mean jet velocity ($\bar{u}_j$) ("jet bulk velocity") and the jet amplitude (u_A), respectively.

The calibration process yields to a correlation that provides an insight into the system behaviour, i.e. how the ratio c'_μ/c_μ varies with the actuation frequency and also a means to determine $C_\mu =< c'_\mu/c_\mu >$.

The first step to determine the ratio c'_μ/c_μ is to measure the air jet velocity and to separate the mean velocity and the oscillating velocity components. It was first tried to measure the mass flow in the air supply hose using an usual methods such as Pitot-pipe and then to calculate the mean speed at the slot exit once this area is known. However, due to the low mass flow, uncertainties would be unacceptably high for those measurement techniques. To solve a similar problem Culley et al. [12] placed and fixed a single hot-wire probe directly at the slot exit. The drawback is that due to the high gradient of the velocity profile at slot exit, the probe is very likely to measure a value that does not represent the mean value, hence the procedure is not able to assure repeatability. To overcome this issue the mean velocity at the slot exit was determined indirectly by first measuring the complete velocity profile in a vertical section downstream of the slot exit. Next, the mean velocity profiles were integrated to obtain the "bulk" mean velocity.

The integration limit of the profiles were defined according to the correlation of White for mixing jets, which establishes the free-shear layer velocity resulting from flows of different velocities [**?**]. The mean velocity at the slot exit was then calculated considering

the mass conservation law, the flow is also assumed incompressible since the Mach number is kept low. Equation 4.1 was used to calculate the velocity at slot exit, whereas k is the limit of integration derived from White's correlation and b is the slot width.

$$\bar{u}_j = \frac{b}{k} \int_0^k \bar{u}(y)\, \mathrm{d}y \tag{4.1}$$

Triggered hot-wire measurements, synchronized with the solenoid valve for the case of unsteady jets, were made as the hot-wire probe wastraversed in the normal direction from the surface up to a point where the measured velocity decreased to approximately zero. The procedure was repeated for different operating points, resulting in a comprehensive combinations of momentum coefficient and actuation frequencies. The traversing station was located directly at the pressure tap 3, approximately 11 mm downstream from slot exit (Fig. 4.1).

Following the procedure above the measurement station does not have to be the very same for each measurement because the limit of integration is automatically readjusted, i.e. if the measurement plane is closer to the slot exit, the integration limit will be lower and the velocities at each point will increase and vice-versa.

It should be stressed that the jet flow is not homogeneous along the slot, because at the slot ends vortical flow arises resulting in a three dimensional flow. The assumption in the calculation process was that the flow is bidimensional at the mid plane. It is expected that this procedure yields to more reliable results than by the use of a fixed probe at the slot exit. Last, it is important to emphasize that the assumptions taken in calibration were very strong and the real values may deviate significantly from those calculated, but the main goal is to describe the characteristics of the actuator.

Once the velocity at the slot exit was determined the next steps were:

- establishment of a correlation for c_μ using $\bar{u}_j$, the pressure ratio between the air supply hose and ambient pressure (pr) and the actuation frequency f;
- establishment of a correlation for c'_μ using u_A, pr and f;
- the momentum coefficient C_μ is then declared as a combination of c_μ and c'_μ, expressed as $C_m u =< c_\mu, c'_\mu >$.

In the next sections the experiments and analysis for this development are presented.

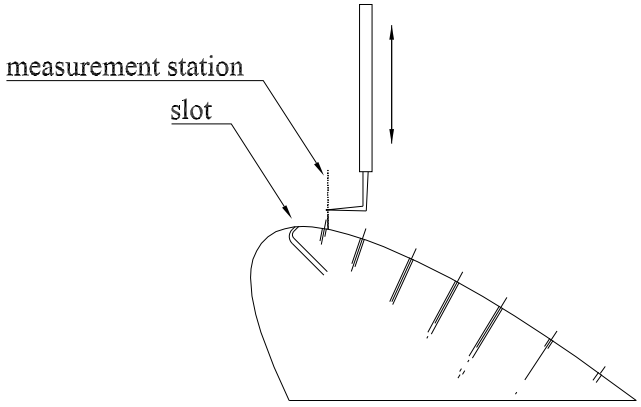

Figure 4.1: Measurement plane adopted to determine the u_j in different operation points.

Correlation for c_μ - Mean Velocity Profiles

The jets from the actuator were traversed for pressure ratio pr = 1,36, 1,63, 2,08, 2,53 and 2,98, at each one the velocity profile was acquired for f = 0, 10, 25, 50, 100 Hz; whereas f = 0 Hz means steady flow. Figure 4.2 shows the mean velocity profiles recorded.

The White's correlation estimates the interface velocity for two parallel jets; for a jet discharged in still air, at the location where the velocity corresponds to approximately 60% of the jet maximal velocity [**?**]. The calibration was conducted in still air, hence the integration limit could be identified, i.e. the point where the jet ends. Note that if the probe traversing was made from the surface up to the point where the air was completely still would have lead to a false result, since the jet entrains the surrounding air.

Once the mean jet velocity $\bar{u}_j$ was determined at the slot exit using the equation 4.1, linear fits were traced (fig. 4.3). Every curve fit has the form $\bar{u}_j(f) = \zeta(pr-1)$, see equations 4.2). If ζ is expressed as a function of *f*, $\bar{u}_j$ can be described solely as a function of f and pr.

$$\begin{aligned} \bar{u}_j(0Hz) &= 6,39(pr-1) \\ \bar{u}_j(10Hz) &= 2,91(pr-1) \\ \bar{u}_j(25Hz) &= 3,18(pr-1) \\ \bar{u}_j(50Hz) &= 3,42(pr-1) \\ \bar{u}_j(100Hz) &= 4,10(pr-1) \end{aligned} \tag{4.2}$$

In the figure 4.4 ζ is presented as a function of f together with a linear fit (Eq.4.3).

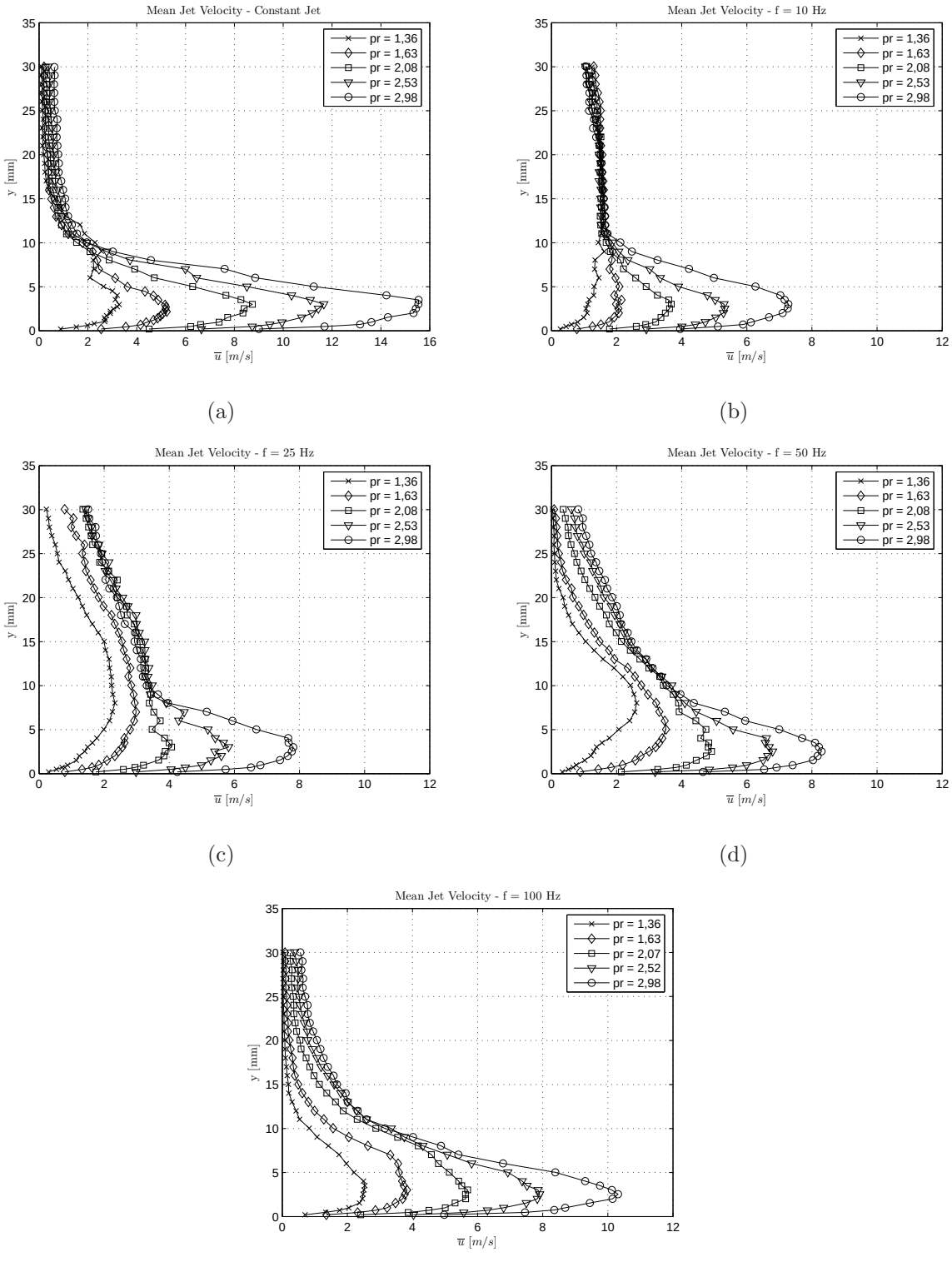

Figure 4.2: Mean velocity profiles of injected air jets.

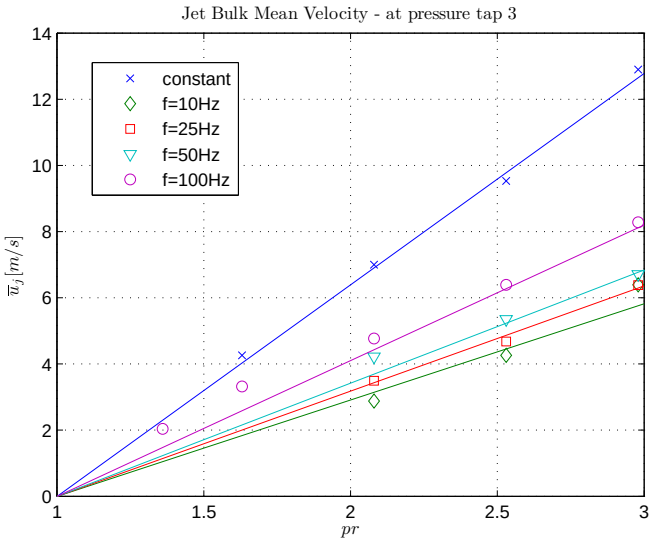

Figure 4.3: Jet mean velocity at slot exit as a function of f and pr.

Now, using the actual slot width $b = 0{,}5$ mm, airfoil chord $c = 0{,}37$ m and fixing the free stream velocity $u_\infty = 3{,}7$ m/s (equivalent to $Re = 90.000$, used in the experiments) c_μ can be calculated from its definition (Eq. 4.4). Note that the correlation is valid for $10Hz \leq f \leq 100Hz$, and since the mean jet velocity for $f = 100$ Hz. For steady jets the valid equation is the equation 4.5.

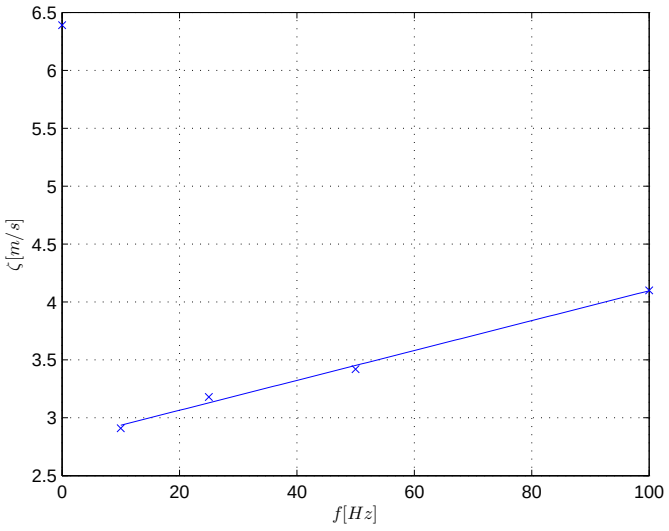

Figure 4.4: Adjustment of the ζ as a function of f.

$$\zeta = 0,0129f + 2,8068 \tag{4.3}$$

$$c_\mu = \left(\frac{2b}{u_\infty^2\, c}\right) \bar{u}_j^2 = 1,97 \times 10^{-4} \left[0,0129f + 2,8068\right]^2 (pr-1)^2 \tag{4.4}$$

$$c_\mu = \left(\frac{2b}{u_\infty^2\, c}\right) \bar{u}_j^2 = 1,97 \times 10^{-4} (6,39)(pr-1)^2 \tag{4.5}$$

Correlation for c'_μ - Unsteady Runs

A similar procedure was adopted to derive a correlation for c'_μ, whereas the jet amplitude (u_A) was used (see Eq. 2.4) instead of using $\bar{u}_j$. The unsteady component of the momentum coefficient (c'_μ) characterizes the amplitude of the jet pulsation and completes the specification for a given C_μ.

The u_A used for the calculation of c'_μ is the one recorded at the point of maximum mean velocity in the mean velocity profiles. The velocity runs at the point of maximum mean velocity are presented in the figure 4. It is noticeable that in low actuation frequencies, up to 50 Hz, the jet oscillates in a well behaved form, following very well the aperture and the closure of the solenoid valve. For higher frequencies the oscillation looses its form and its amplitude is damped. The reason for the damping is that at higher frequencies the air between the solenoid valve and slot exit don't have enough time to flow out from the hoses before the valve opens again, damping the pulsation effect.

The high frequency oscillations make it difficult to assert the amplitude, hence the amplitude adopted was the difference between the mean of the 10% higher values and of the 10% lower values. The resulting amplitudes are displayed in the figure 4.6 as a function of the actuation frequency (f) and pressure ratio (pr). Linear curves were fitted in the data, expressed by equations 4.6, which can be expressed in the form $u_A = \phi(pr-1)$.

$$\begin{aligned} u_A(10Hz) &= 8,20(pr-1) \\ u_A(25Hz) &= 7,60(pr-1) \\ u_A(50Hz) &= 4,95(pr-1) \\ u_A(100Hz) &= 3,84(pr-1) \end{aligned} \tag{4.6}$$

The correlation of ϕ with f is straightforward: ϕ is arranged as a function of f and the best fit curve is determined. A power curve was chosen to model for ϕ, the curve fit is then ploted in the figure 4.7. Substituting ϕ in the equation $u_A = \phi(pr-1)$ completely describes u_A as a function of the actuation frequency and pressure ratio (Eq. 4.7). At this

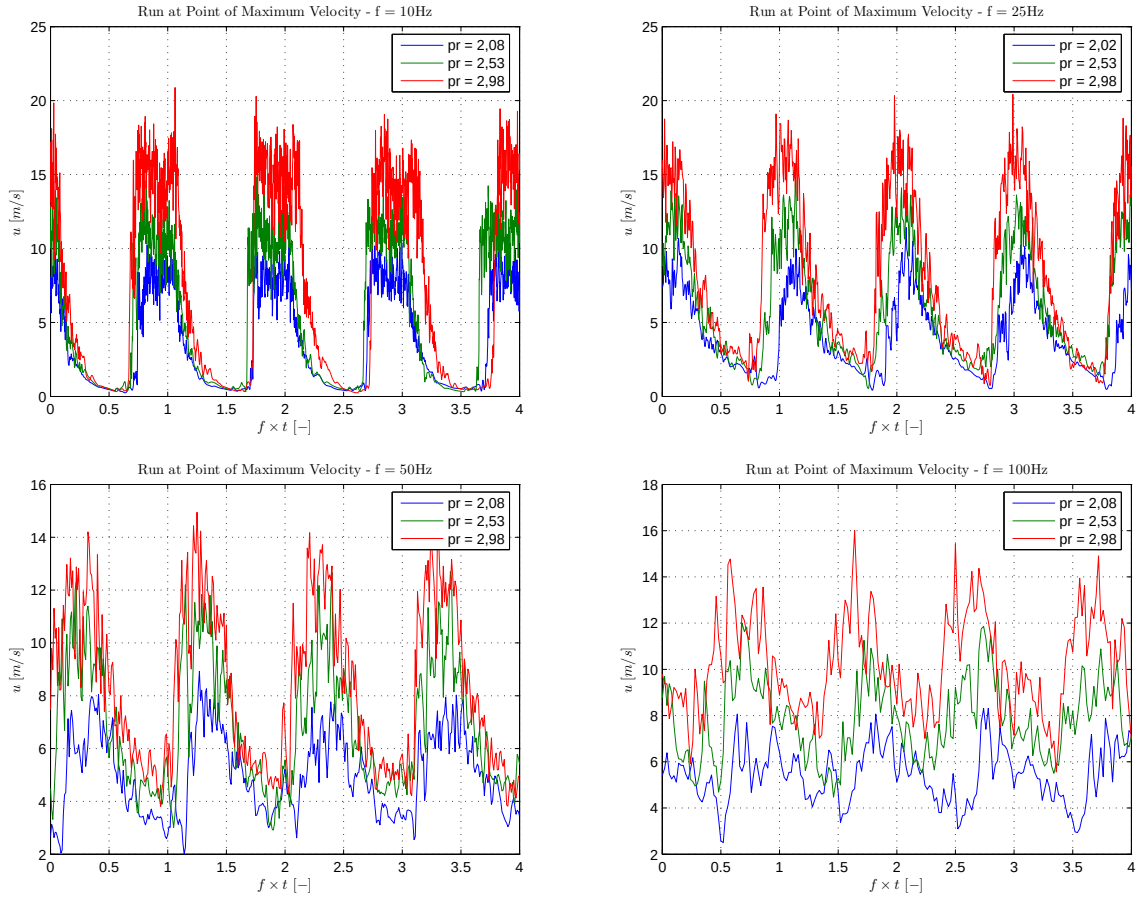

Figure 4.5: Velocity runs at point of maximum mean velocities.

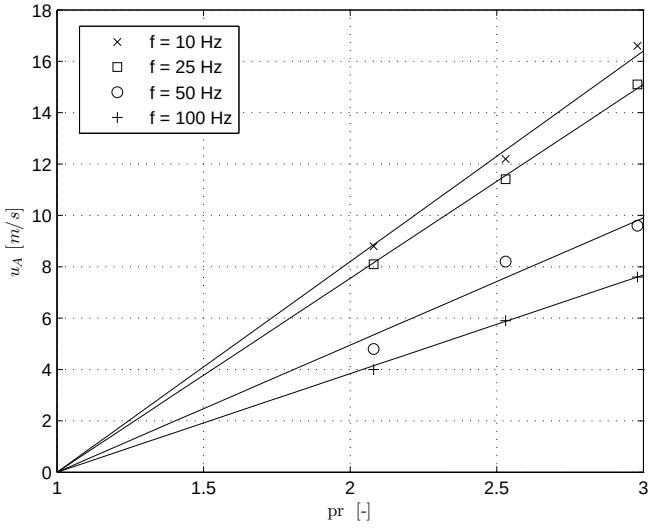

Figure 4.6: u_A as a function of pr and f.

point the unsteady component of the momentum coefficient c'_μ can be directly calculated through the expression 4.8.

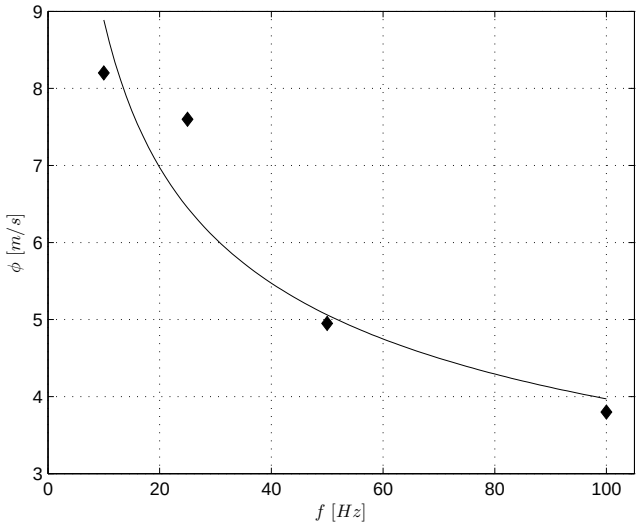

Figure 4.7: Coefficient ϕ as a function of *f*.

$$u_A = \phi\ (pr - 1) = 19,9 f^{-0,35}(pr - 1) \tag{4.7}$$

$$c'_\mu = \left(\frac{2b}{{u_\infty}^2 c}\right) {u_A}^2 = 7,8 \times 10^{-2} f^{-0,7}(pr - 1)^2 \tag{4.8}$$

The development of the correlations for c_μ and c'_μ presented here is a means to determine approximately the components of C_μ: c_μ and c'_μ. In spite of known limitations and assumptions, it is assumed that a good compromise is achieved and the current procedure represents an alternative to other methods. The inherent errors are smaller than that resulting from measurements of a single fixed point at the slot exit. From this point, the actuator's operation points are determined by equations 4.4 and 4.8. For the present experiments the actuator's range of operation for c_μ and c'_μ are displayed by figure 4.8 using the derived correlations. As indicated by the arrow, increasing the actuation frequency decreases the jet pulsation amplitude, what damps the pulsating effect of the actuation system. That can be better visualised by the ratio between of the components of C_μ (c_μ and c'_μ) - presented in figure 4.9. It demonstrates how the jet oscillation is damped with the increasing of *f*, what suggests that the unsteady jet behaves more similar to a steady jet as the frequency is increased.

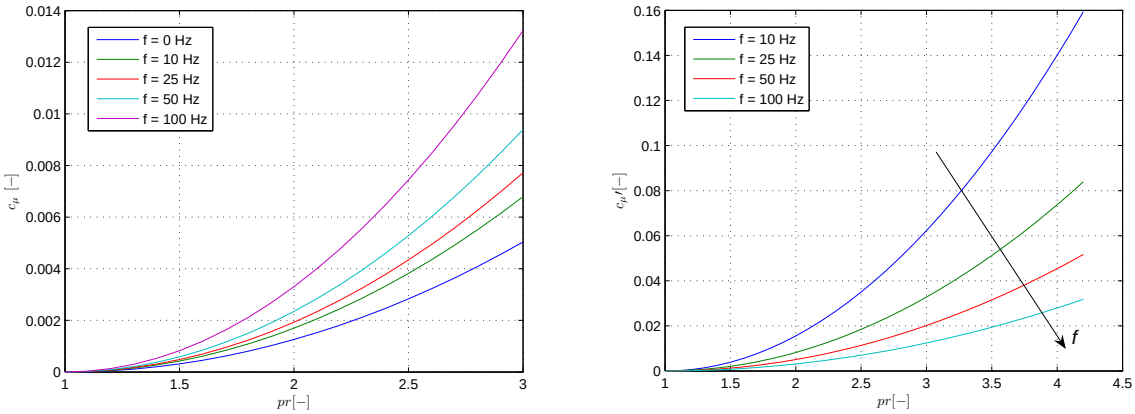

(a) (b)

Figure 4.8: c_μ *(a)* and c'_μ *(b)* as functions pr.

In the next chapter the results of experiments with the actuator system are presented and both c_μ and c'_μ are always provided to give a picture of the actuator system operating point.

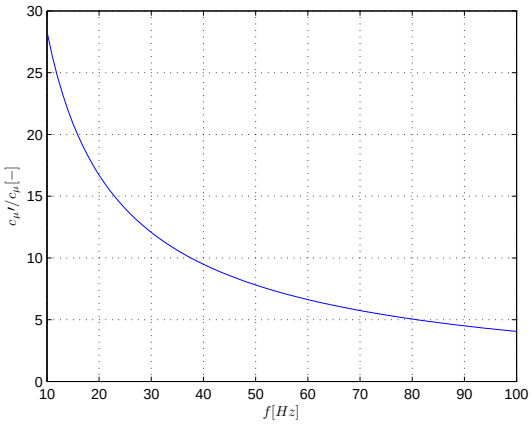

Figure 4.9: Ratio of c_μ and c'_μ as a function of f, derived from eqs. 4.4 and 4.8.

Chapter 5

Results

Attached and separated boundary-layers were investigated through measurements of pressure distribution, particle image velocimetry and hot-wire anemometry. The results are presented and discussed for the experiments conducted at $Re = 90.000$ with the airfoil at angles of attack in the range 4° to 22,5°.

The operating points of the actuation system were determined from the findings of other researchers, as cited in the literature review and from preliminary experimental tests. In the wind tunnel the use of cotton tufts placed over the suction surface of the airfoil permitted to visualise the flow reattachment as the amount of injected air was varied, i.e. according to the added momentum coefficient, as well as the actuation frequency was changed. This procedure allowed the identification of the most effective actuator settings. The selection of test points is described in the section 5.1.

The pressure distribution presented in the section 5.2 provided the first quantitative data, enabling the comparison of the flows around the airfoil without and with flow control. Based on these results, representative cases were selected to be further investigated in more detailed experiments with hot-wire anemometry and with PIV, which are presented in the section 5.3 and 5.4, respectively.

Hot-wire anemometry provided highly time and space resolved velocity fields ranging from the surface up to a few centimeters above it. Compared to the pressure distribution it describes more precisely the unsteady behaviour of the boundary-layer under the influence of pulsed jets. From the PIV measurements low spatially resolved velocity fields were obtained for the whole main flow.

5.1 Tests Conditions

The choice of an appropriate Reynolds number and the range of angle of attacks was the first step taken to set the test conditions, they had to represent the real flow of machines of interest. The second step was the definition of the active control parameters, f^+ and C_μ.

Relevant operational Reynolds numbers found in machines were considered first. According to Schreiber, compressor blades operate at high Re; in aero-engines from Re = 600.000 up to 1.200.000, while in industrial compressors it may range from 2.000.000 to 4.000.000 [**?**]. Wang adopted a NACA $63_3 - 018$ airfoil at Re = 300.000 to study the flow around compressor blades and showed that the Reynolds number range can be wider [7]. Low pressure turbines blades (LPT) play a central role in the efficiency of turbines, since their performance have the greatest impact on the machine [**?**] and they have typical Re between 80.000 and 300.000 (Schulte and Hodson, [**?**]). Remotely piloted vehicles, high-altitude vehicles, wind turbines and propellers are other examples where blades and airfoils operate under Re = 500.000 [**?**].

Considering the importance of components operating at low Reynolds numbers and looking for a compromise between the capability of the available test rig and airfoil size, it was decided to run the experiments at Re = 90.000. It yielded to an airfoil with 370 mm chord length, making high spatial resolution measurement possible. The angle of attack was varied in the range $4° \leq \alpha \leq 22{,}5°$ in the measurement of the static pressure distributions without active control. Based on the those measurements, two angles of attack were chosen to carry out more detailed experiments with PIV and with hot-wire anemometry. It was asserted that imminent boundary-layer separation takes place at 17,1° while complete separation occurs at 18,9°.

There is a strong divergence in the literature about the most effective dimensionless frequency (f^+), in the current work its influence was examinated within the range defined according to the suggestions of different authors. Smith [5] suggested $f^+ = 10$ as the most effective, while Seifert et al. [16] $1 \leq f^+ \leq 3$. Wang [7] asserted a correlation to determine the most efficient f^+, which for the current test conditions results in an optimal range between $1,6 \leq f^+ \leq 2,1$. Boundary-layers are very receptive to disturbances at the same frequency of the vortex street emanating from the respective body. To explore this fact, a hot-wire was traversed in the airfoil wake, distant one chord downstream of the trailing edge at $\alpha = 18,9°$, and the velocity magnitude was recorded. A Fast Fourier Transform

from this record is presented in figure 5.1. The strongest signal is found at 10 Hz (f^+ = 1), which corresponds to the most efficient f^+ suggested by Seifert et al.. In order to cover a wide range of actuation frequency, the following values were used: f^+ = 1, 2,5, 5,0 and 10,0 - they correspond to 10, 25, 50 and 100 Hz in the solenoid valve operating frequency.

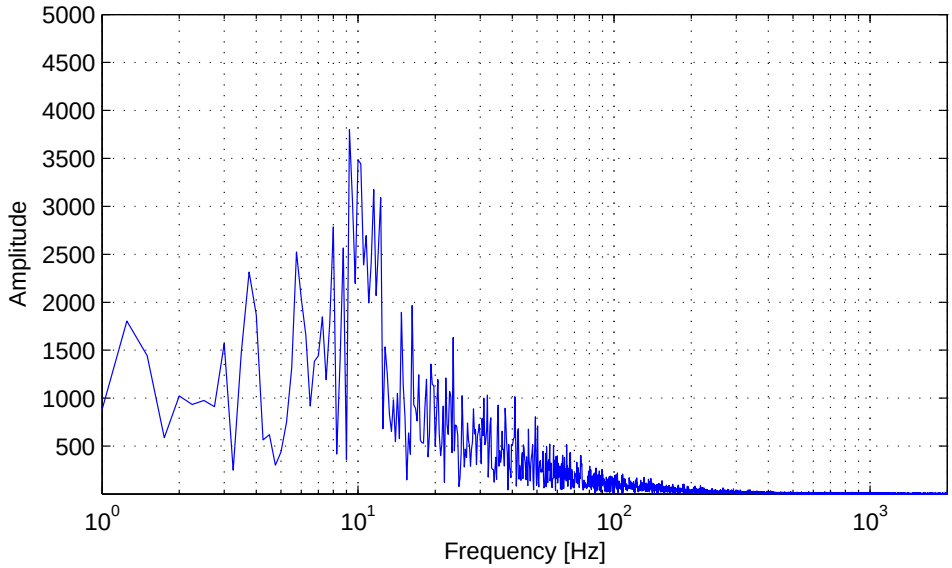

Figure 5.1: Frequency Spectrum in the wake of the airfoil at α=18,9°.

The proper range of momentum coefficient C_μ was determined through visual inspection of cotton tufts placed on the airfoil's surface. For each f^+ the mass flow was increased from zero until the tufts stopped to oscillate and the boundary-layer reattaches - the corresponding mass flow injected served as a reference for the lower value of C_μ range. To cover a significant range, the C_μ used started slightly below the values asserted by the tufts inspection and was increased in steps. The table 5.1 presents the range of C_μ, splitted in its components for each f^+ used.

Table 5.1: Range of active control parameters used in the tests.

f	f^+	c_μ	c'_μ
0 Hz	0	0,0001 - 0,0068	0
10 Hz	1	0,0002 - 0,0182	0,0018 - 0,1663
25 Hz	2,5	0,0047 - 0,0193	0,0198 - 0,0820
50 Hz	5,0	0,0027 - 0,0222	0,0058 - 0,0477
100 Hz	10,0	0,0070 - 0,0293	0,0066 - 0,0275

5.2 Static Pressure Distribution

The measurement of pressure distribution provided the first insight into the boundary-layer behaviour of the NACA $63_3 - 018$ airfoil and hence about the most relevant cases to be examined in detail with the application of active control. At $Re = 90.000$ the pressure distribution for the airfoil in the range from 4° to 22,5° is presented by the figure 5.2. The negative pressure peak increases gradually in the front portion of the airfoil, up to 20% of the chord, as the angle of attack is increased from $\alpha = 4°$ to 16°, (a) and (b) respectively.

The boundary-layer remained completely attached up to $\alpha = 16°$, at this angle a flat region at the rear part of the airfoil is an indicative of boundary-layer separation. The displacement of the separation from the trailing-edge in the upstream direction (*trailing-edge stall*) was also reported at a higher Reynolds number ($Re = 5,8 \times 10^6$) by McCullough and Gault using the same airfoil [**?**]. Further increase in the angle of attack resulted in a small increase of the pressure coefficient close to the leading edge and in the displacement of separation to an upstream position, from approximately 65% of chord at $\alpha = 16°$ to 55% at $\alpha = 17{,}1°$ (b). Above $\alpha = 18{,}9°$ the static pressure distribution was completely flat indicating massive separation of the boundary-layer.

Based on the airfoil performance given by the pressure distribution, the cases to be investigated in more detail were at $\alpha = 17{,}1°$ and $\alpha = 18{,}9°$. The first angle corresponds to a barely stalled airfoil, leading to an interesting investigation on how active excita-

tion affects an attached boundary-layer at imminent separation. The second angle, α = 18,9°, was a typical test case for active control, whereas the boundary-layer is completely separated but expected to be recovered.

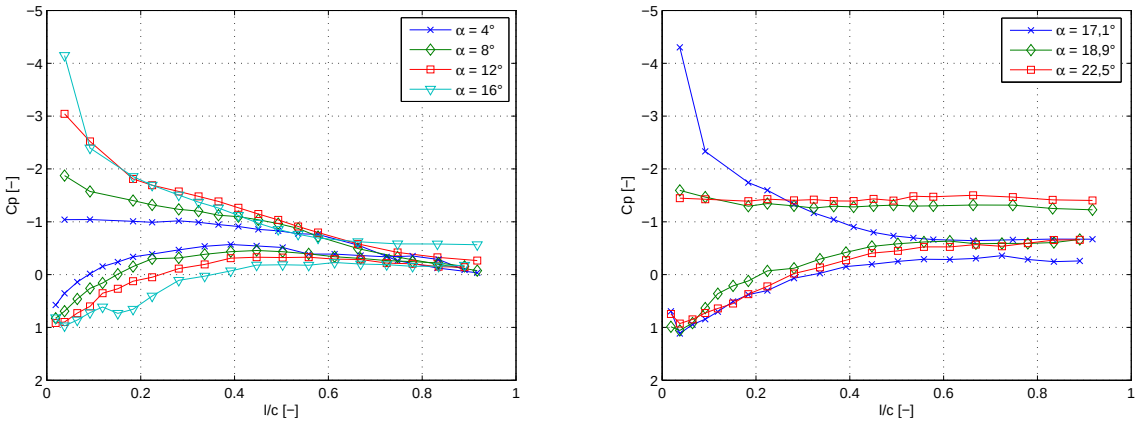

(a) (b)

Figure 5.2: Static pressure distribution without flow control at Re = 90.000.

5.2.1 Pressure Distribution - Active Control at α = 17,1°

The first operation of active control was made at the pre-stall angle of attack α = 17,1°. In the presentation of results (Fig. 5.3) the nondimensional frequency f^+ was chosen and the intensity of actuation varied, expressed by C_μ. The pressure distribution represents a mean value, since the relative fast pressure oscillation cannot be resolved by this measurement technique.

In the case of steady injection (a) one observes that the point of separation does not change even with high levels of momentum injected, i.e $C_\mu = c_\mu$ = 0,0327. The pressure peak is slightly increased in the attached region but not in a linear manner - since the increase of one order of magnitude in c_μ is not followed by the increase in C_p. An observation must be made regarding very low level of injection, represented by c_μ = 0,0010 at f^+=0: injection has to be made above a minimum level of C_μ, otherwise it deteriorates the flow and promotes premature boundary-layer separation. Culley et al. encountered the same issue injecting low momentum fluid in a stator row of an axial compressor [11].

Steady (a) and pulsed injection (b to e) (Fig. 5.3) do not present significative dif-

ferences, except that - in contrast with steady injection - pulsed injection of very low momentum flow is not prejudicial. As can be ascertained comparing unsteady injection at $c_\mu = 0{,}0002$ and f^+=1,0 with steady injection at $c_\mu = 0{,}0010$. Neither the variation of actuation level nor the nondimensional frequency displaced the boundary-layer separation downstream or has shown a reasonable performance improvement.

One may conclude that for attached boundary-layers air injection (either steady or pulsated) did not bring a gain at the ”pre-stall” condition but can be rather detrimental. In the next section the potential contribution of air injection is examined for a completely separated boundary-layer.

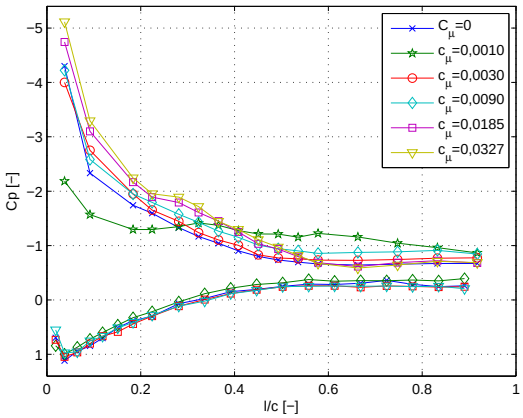

(a) $\alpha = 17{,}1°$, $f^+ = 0$.

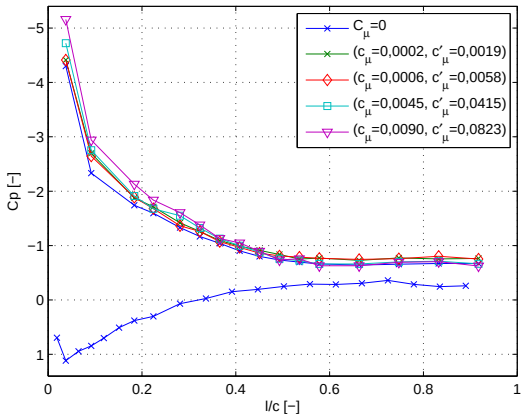

(b) $\alpha = 17{,}1°$, $f^+ = 1{,}0$.

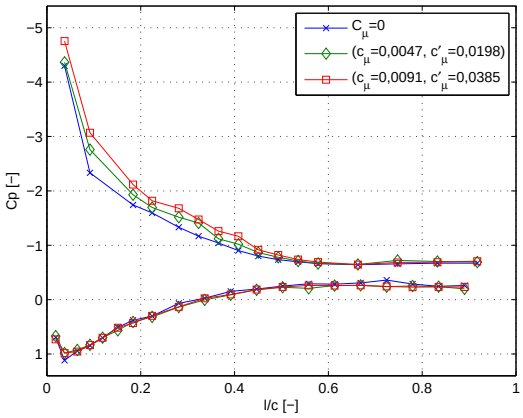

(c) $\alpha = 17{,}1°$, $f^+ = 2{,}5$.

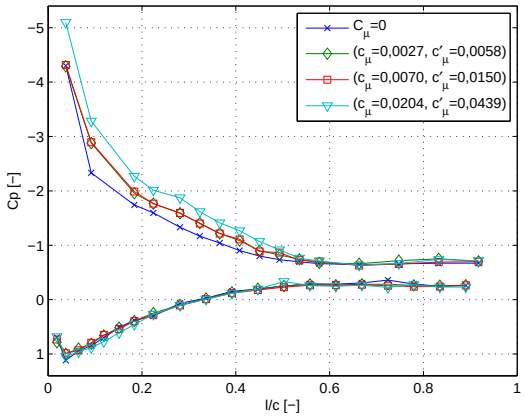

(d) $\alpha = 17{,}1°$, $f^+ = 5{,}0$.

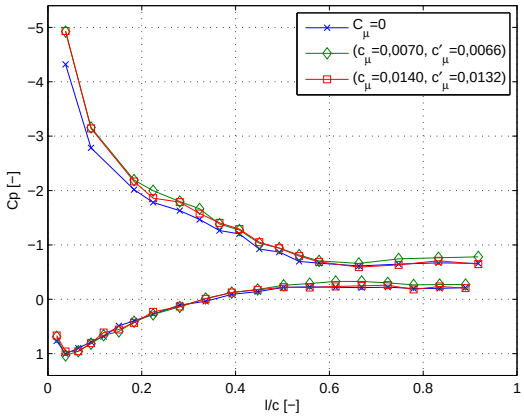

(e) $\alpha = 17{,}1°$, $f^+ = 10{,}0$.

Figure 5.3: Static pressure distribution using different f at $\alpha = 17{,}1°$

5.2.2 Pressure Distribution - Active Control at α = 18,9°

In opposition to the previous case, active control had significant impact on the fully separated flow found at α = 18,9°. Pressure distributions profiles are presented in the figure 5.4. Both steady (a) and pulsed air injection (b to e) had a global effect in the flow, which was not restricted to the suction side. This overall change resulted in lift increase, since the difference of pressure of both sides increased. At the suction side the flow was able to reattach the flow up to 45% of the chord regardless which type of injection was used.

The pressure distribution on the pressure side converged to a single profile, indicating a probable steady flow there and also the insensitiveness to the variation of the injection set-up. On the suction side however, one sees that the pressure peak increased for higher mass injection.

The results using pulsated injection (b to e) represent the mean value of the pressure distribution, a highly unsteady flow was expected for those cases, since the boundary-layer was originally completely separated. The reattachment extended to approximately 50% of the chord. To compare the effect of a fixed f^+, a equivalent C_μ was adopted: for f^+ = 0; 1; 2,5; 5,0 and 10,0 the chosen c_μ were c_μ = 0,00185; 0,0090; 0,0091; 0,0070 and 0,0071 respectively. No tendency could be related to the actuation frequency, only that the boundary-layer separates further downstream when steady injection was used and that for $f^+ = 10$ the behaviour was similar to that at $f^+ = 0$, which was due to the very low magnitude of the air jet oscillation produced at this frequency.

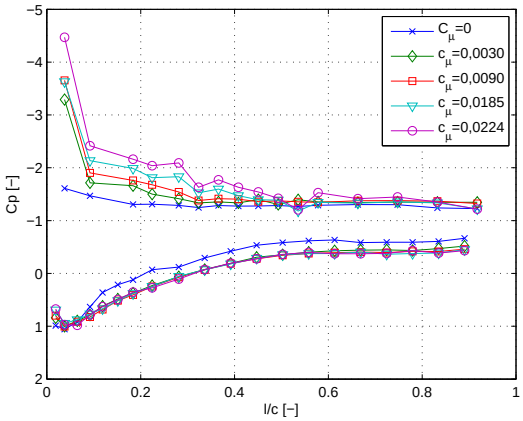

(a) $\alpha = 18{,}9°$, $f^+ = 0$.

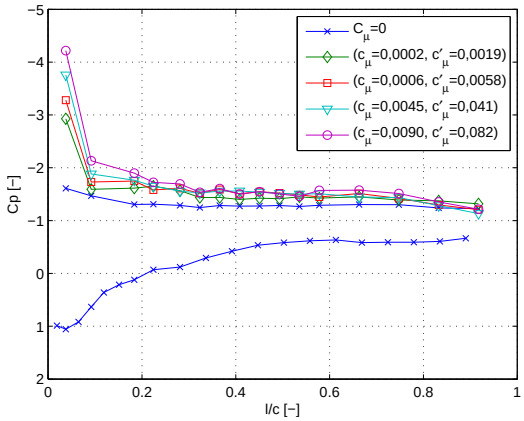

(b) $\alpha = 18{,}9°$, $f^+ = 1{,}0$.

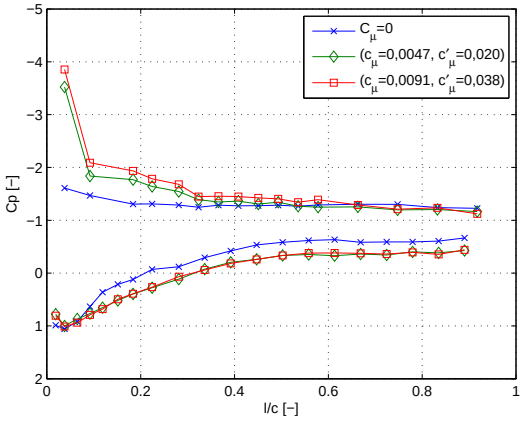

(c) $\alpha = 18{,}9°$, $f^+ = 2{,}5$.

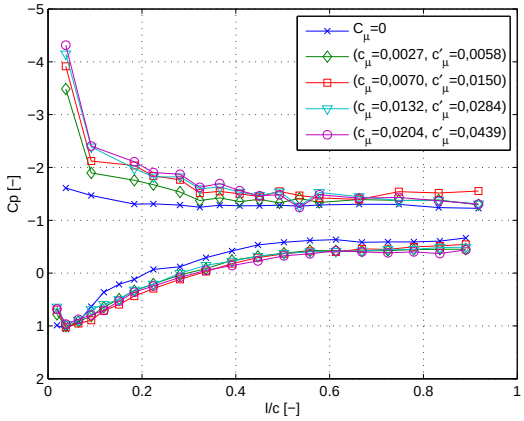

(d) $\alpha = 18{,}9°$, $f^+ = 5{,}0$.

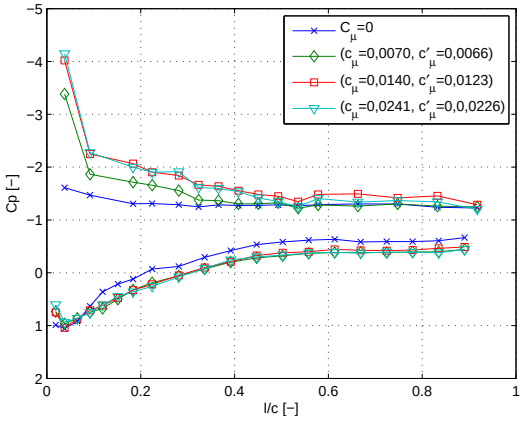

(e) $\alpha = 18{,}9°$, $f^+ = 10{,}0$.

Figure 5.4: Static pressure distribution using different f at $\alpha = 18{,}9°$

The conclusions asserted from the pressure distributions were first that for non-separated boundary-layers leading edge injections did not bring great improvement and could be detrimental when low momentum flow was injected, therefore a minimum level of C_μ had to be supplied. Second, as Bons et al. noticed in a low pressure turbine cascade [9], f^+ had no relevant influence on the flow. A question that arises is what restricts the influence of the steady and pulsated air injection - as observed, regardless of which combination of nondimensional frequency and momentum coefficient is used, the boundary-layer reattachment "converges" to a certain position, this is probably restricted by the pressure gradient. The PIV measurements in the next section shall help to clarify the mechanism of interaction between injection, mean flow and separated boundary-layer (shear layer).

5.3 Flow Field Measurements - PIV

Particle Image Velocitmetry supported quanlitative analysis of the flow fields, and in the present case captures the interaction between the air injection, the boundary-layer and the main flow. Considering the results from the pressure distribution measurement, it was asserted that the analysis of fewer cases would provide a representative view of this interaction.

The cases examined with PIV are presented in the table 5.2. They are focused in the angles of attack $\alpha = 17{,}1°$ and 18,9°, but since C_μ had a minor effect once a minimum level was reached or exceeded, it was decided to fix a single C_μ intensity for each f^+. The only exception was for the steady injection case, whereas three different injection magnitudes were used.

The data acquisition was triggered by the same function generator that controls the solenoid valve of the actuator. For pulsed jets, the acquisition was made at five time instants, normalized by the actuation period (T), resulting in t/T = 0, 0,2, 0,4, 0,6 and 0,8 relative to the trigger start signal. They describe chronologically the development of the flow within an actuation cycle. The unsteady jet was employed at f^+ = 1; 2,5; 5 and 10 for $\alpha = 17{,}1°$ and 18,9°.

Table 5.2: Test cases examined with PIV at angles of attack $\alpha = 17{,}1°$ and 18,9°.

f^+	$< \bar{c}_\mu; c'_\mu >$
normal flow	-
0	<0,0090; ->, <0,0224; ->, <0,0359; ->
1,0	<0,0045; 0,042>
2,5	<0,0047; 0,020>
5,0	<0,0027; 0,006>
10,0	<0,0070; 0,007>

Flow without active control α = 17,1°

The flow field captured with the PIV extends from the leading edge until approximately 60% of the chord. Though it does not capture the whole flow field, it records the main interactions within this frame. The figure 5.5 shows the flow around the airfoil set at α = 17,1°. From this picture one asserts that control would have to deal with a smooth separation taking place at approximately 25% of the chord. The next subsection shows how this smooth separation interacts with the air injection.

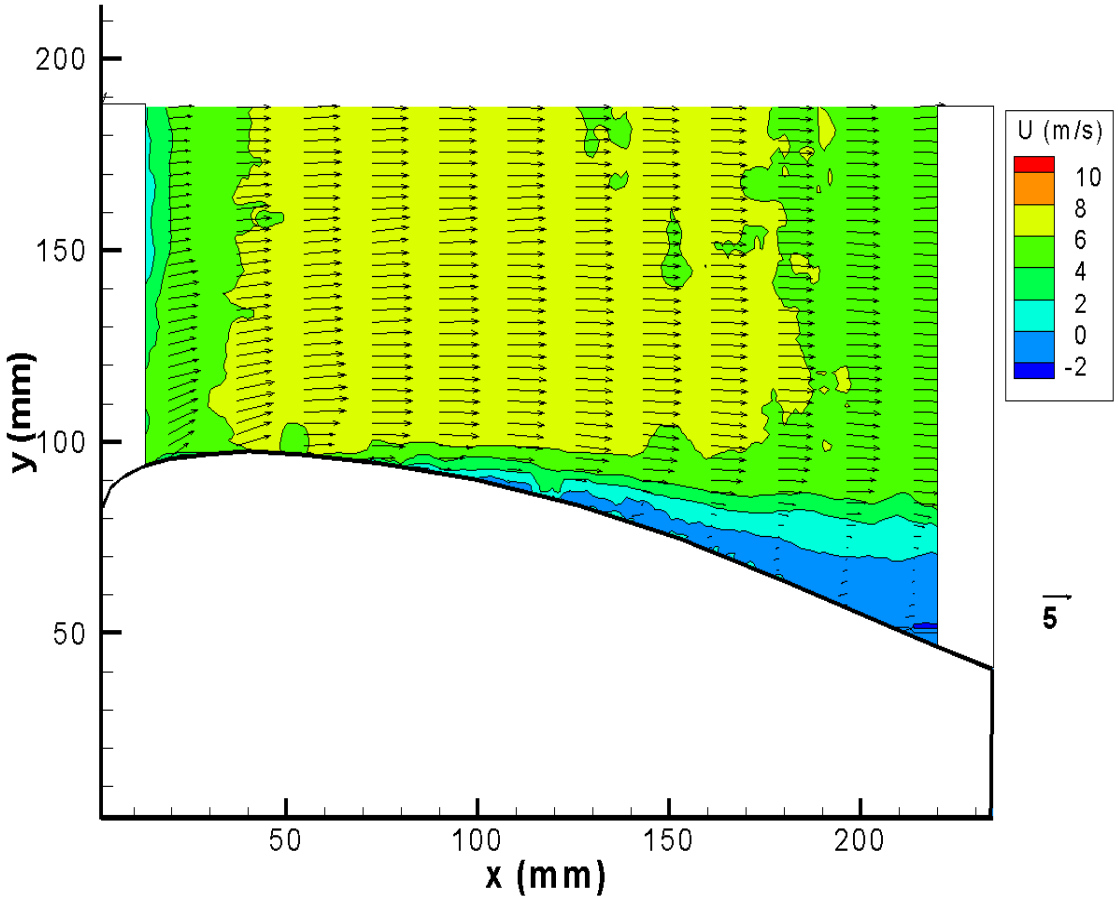

Figure 5.5: Flow field without active control at α=17,1°.

Steady Injection - α = 17,1°

The PIV measurements of steady jet injection at an angle of attack α = 17,1° correspond to the pressure distribution of figure 5.3 and are depicted in the figure 5.6. The steady

jet case serves as a benchmark for the unsteady jet tests. It is clear that the main flow is redirected to the surface in all cases and that separation is displaced downstream. However, even if the momentum coefficient is quadruplicated the separation is not displaced correspondently (see *a* and *c*). The key characteristic observed in the sequence is that a V-shaped region of high speed air flow is formed between the outer flow and the steady jet just above the surface. Moreover, the "V-region" remains practically unchanged with the increase of momentum, what explains why the pressure distribution remains almost unchanged. Apparently the pressure gradient tears the main flow and the injected air jet apart, so that after the "V" vertex the pressure experienced by the suction surface is the same of a separated flow.

Unsteady Injection - α = 17,1°

This section presents the results obtained with four different nondimensional frequencies: f^+ = 1,0; 2,5; 5,0 and 10,0, depicted in figures 5.7 to 5.10. In the figure 5.7 one sees the cyclic behaviour of low frequency actuation: the separation vanishes in the instants *e*, *a* and *b*, which correspond to the open time of the valve. While during the close time, the separation rises again. Similar behaviour was found at f^+ = 1,0 and 2,5, figures 5.8 and 5.9, respectively.

At the highest actuation frequency a steady behaviour is noticed and the overall picture is very similar to tat one of a steady jet. It corroborates the results obtained in the actuator system calibration that during the valve close-time the air inside the connections continues to flow out through the slots.

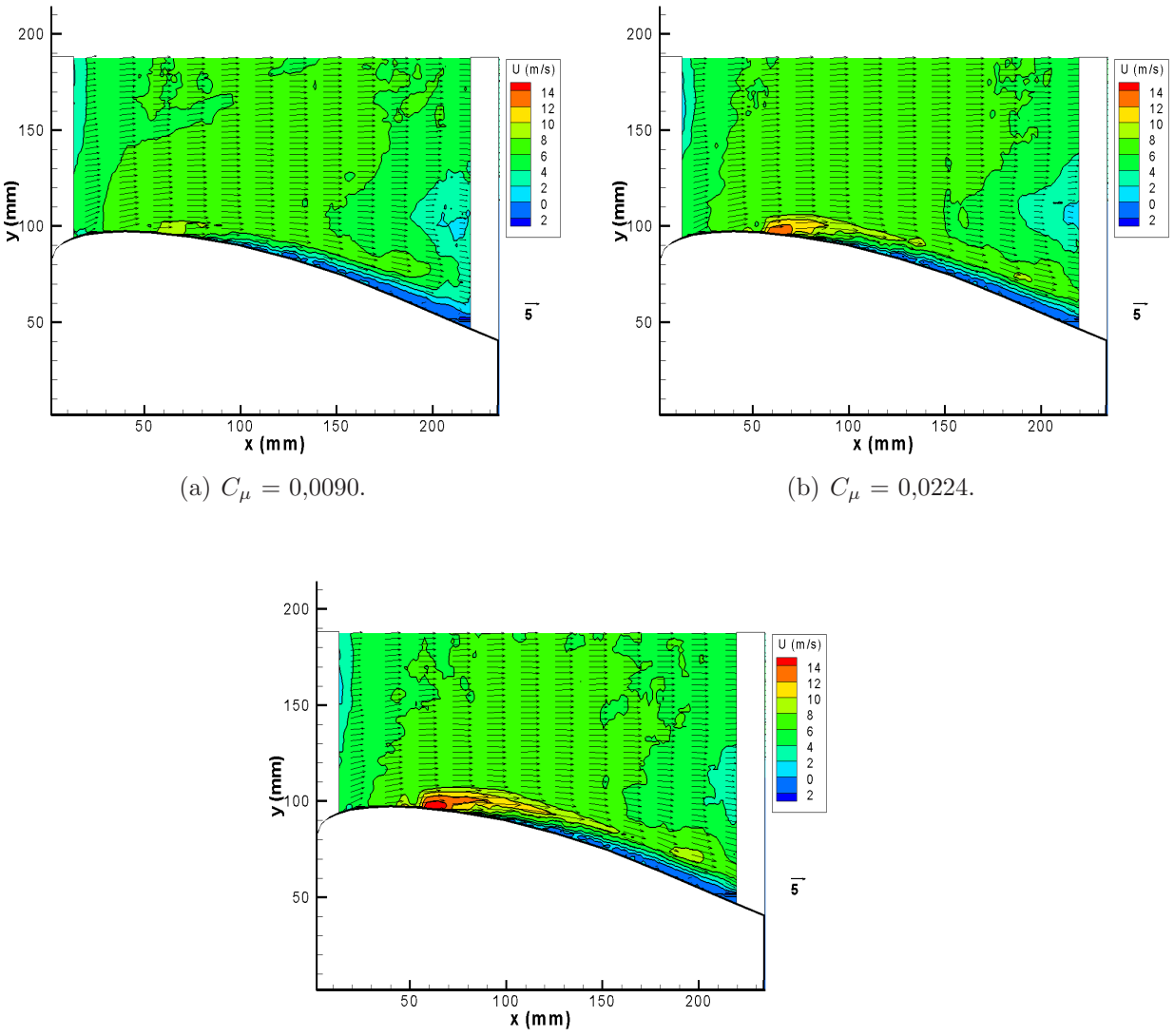

(a) $C_\mu = 0{,}0090$.

(b) $C_\mu = 0{,}0224$.

(c) $C_\mu = 0{,}0360$.

Figure 5.6: Constant injection at α=17,1°.

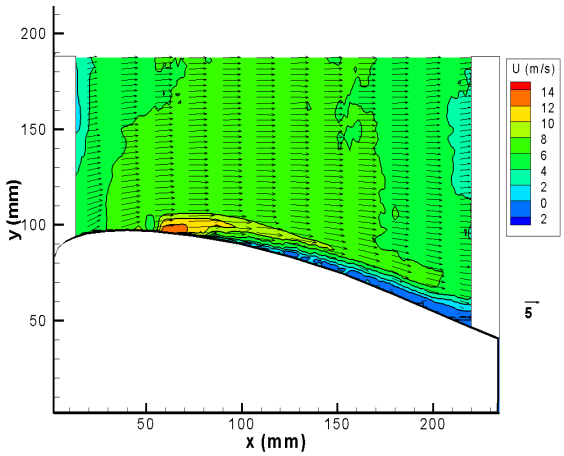

(a) t/T = 0.

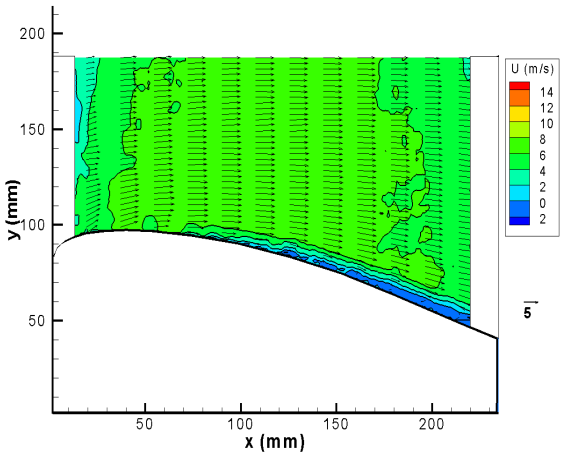

(b) t/T = 0,2.

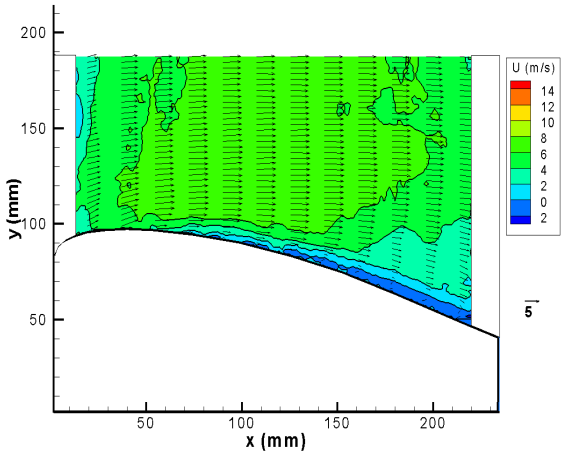

(c) t/T = 0,4.

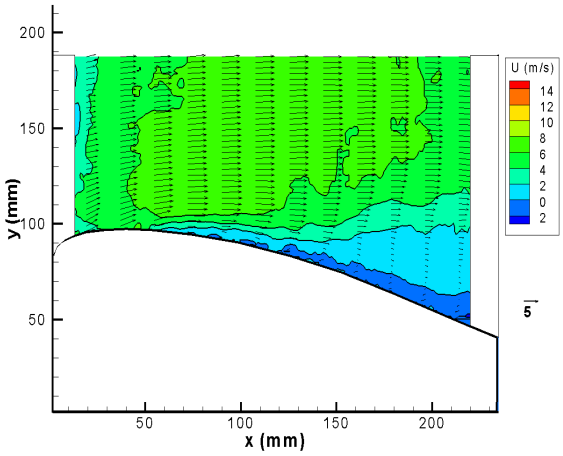

(d) t/T = 0,6.

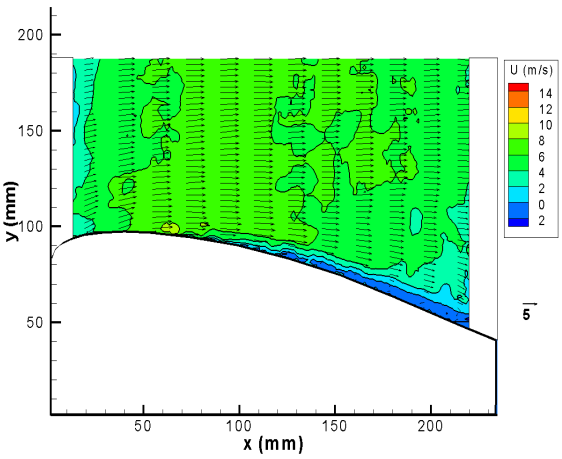

(e) t/T = 0,8.

Figure 5.7: Unsteady injection at α=17,1°, f^+ = 1,0, C_μ = <0,0045;0,0415>.

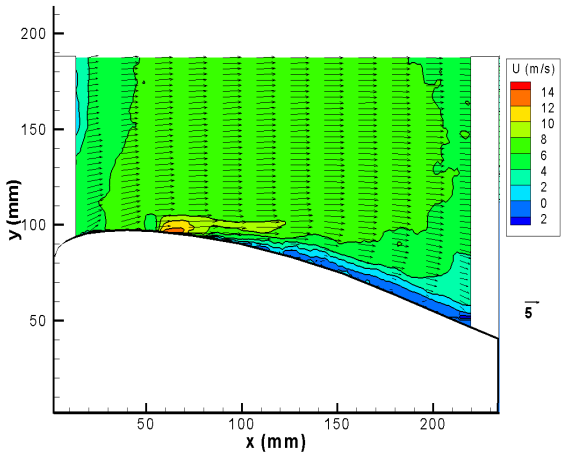

(a) t/T = 0.

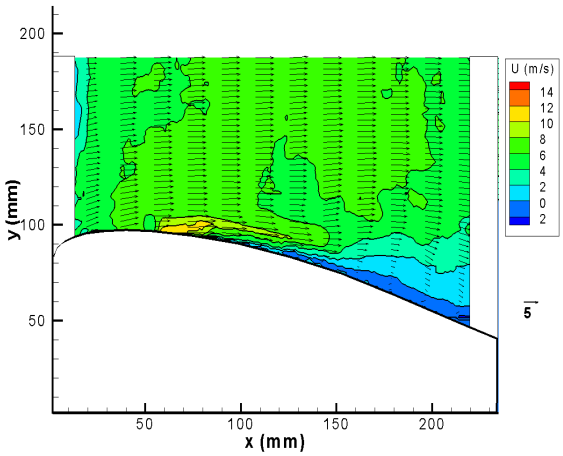

(b) t/T = 0,2.

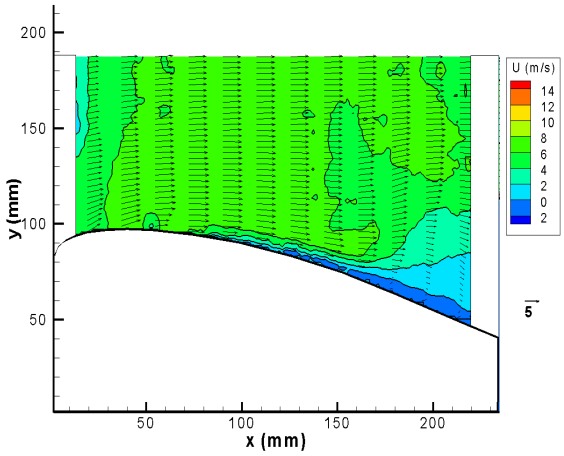

(c) t/T = 0,4.

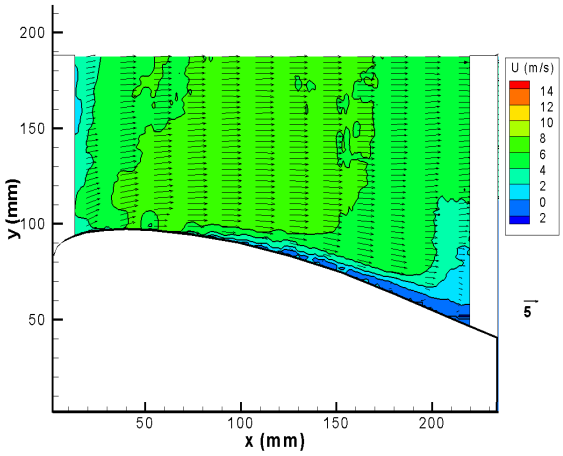

(d) t/T = 0,6.

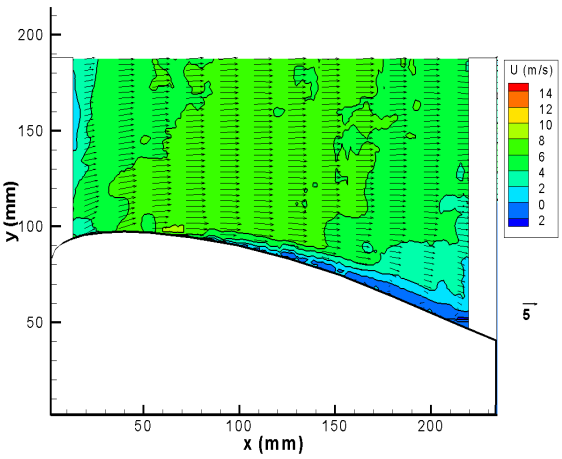

(e) t/T = 0,8.

Figure 5.8: Unsteady injection at α=17,1°, f^+ = 2,5, C_μ = <0,0047;0,0198>.

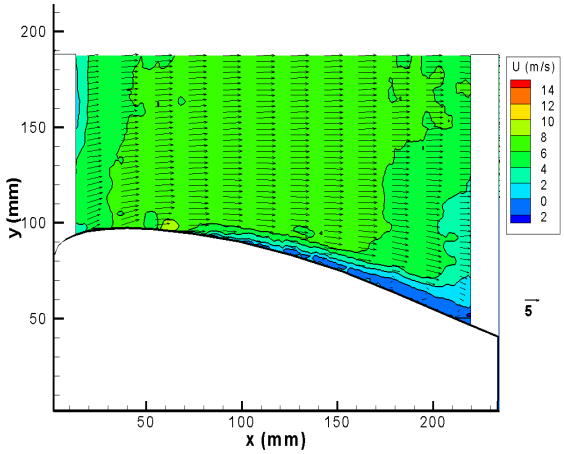

(a) t/T = 0.

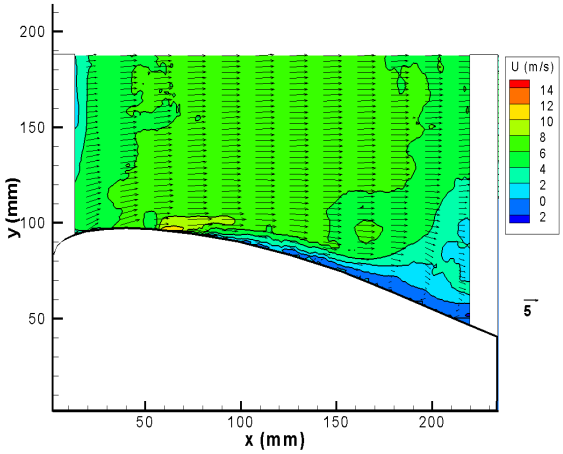

(b) t/T = 0,2.

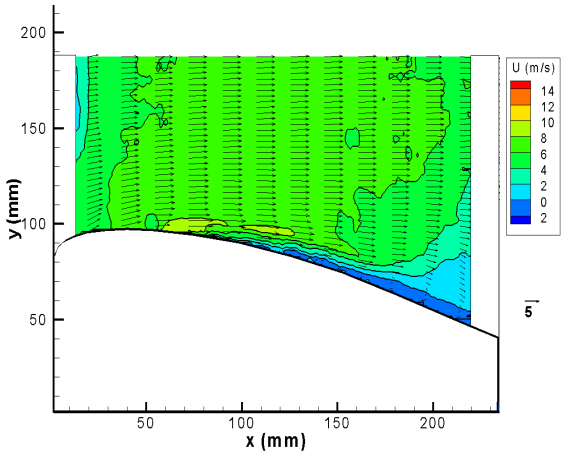

(c) t/T = 0,4.

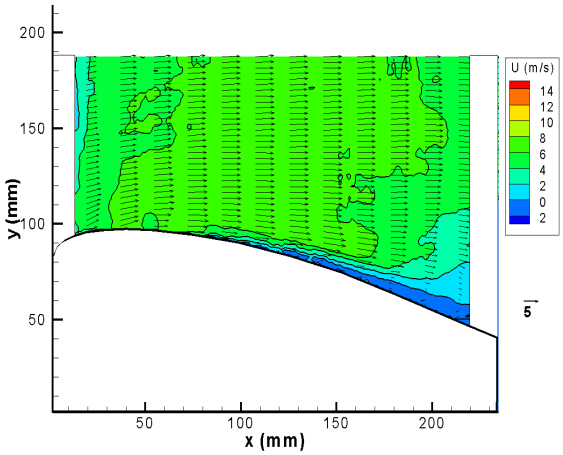

(d) t/T = 0,6.

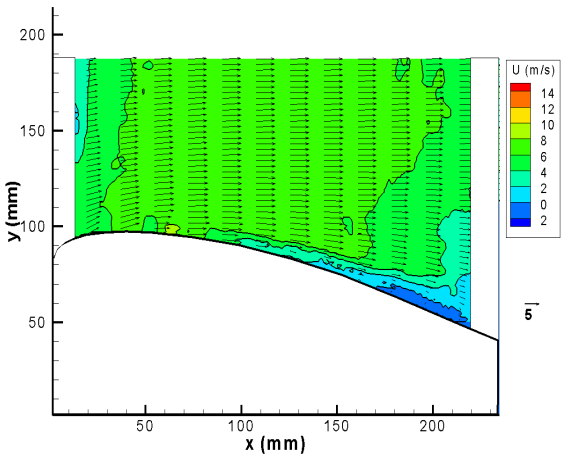

(e) t/T = 0,8.

Figure 5.9: Unsteady injection at α=17,1°, $f^+ = 5{,}0$, C_μ = <0,0027;0,0058>.

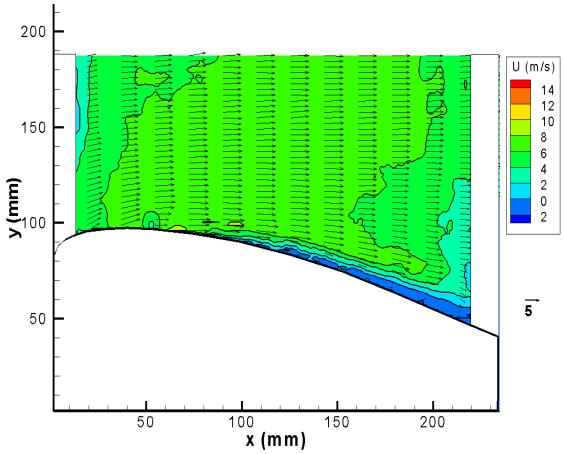

(a) t/T = 0.

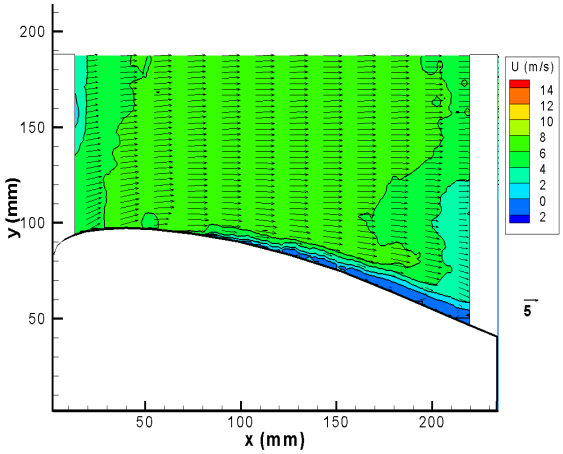

(b) t/T = 0,2.

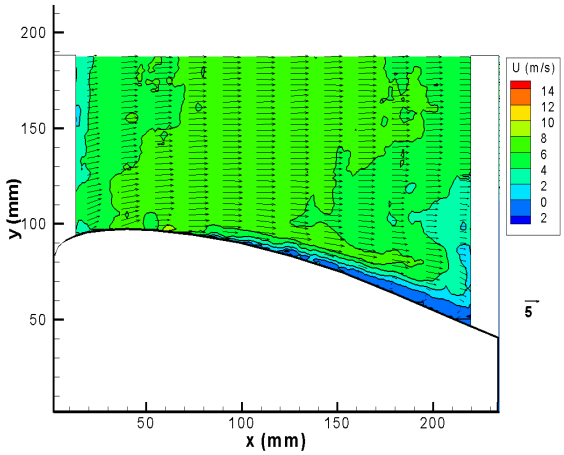

(c) t/T = 0,4.

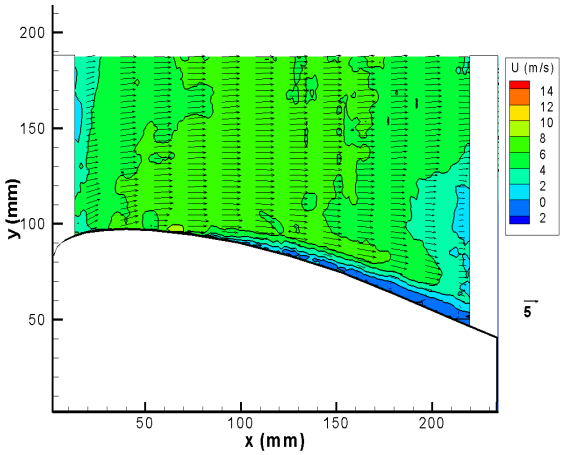

(d) t/T = 0,6.

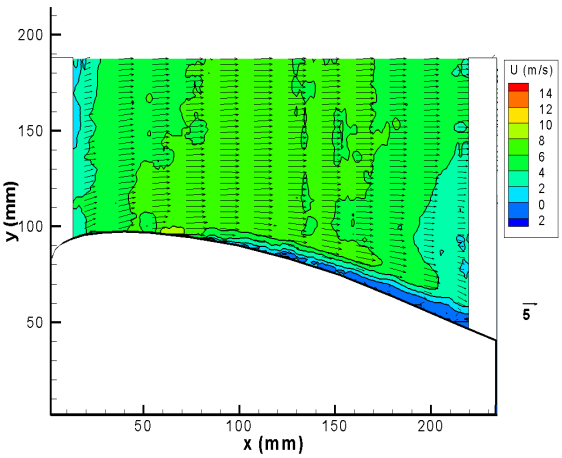

(e) t/T = 0,8.

Figure 5.10: Unsteady injection at α=17,1°, f^+ = 10,0, C_μ = <0,0070;0,0067>.

Flow without active control α = 18,9°

As observed in corresponding pressure distribution, Fig. 5.2, massive separation was expected at $Re_c = 90.000$ and $\alpha = 18{,}9°$. The separation took place close to the leading edge, at $c = 38$ mm without reattachment downstream (see Fig. 5.11). Though this measurement did not supply all information needed, falling back to the initial china clay visualisation it is very likely that separation is turbulent due to the presence of a small separation bubble close to the lading edge and the increase in the roughness of the surface covered with clay.

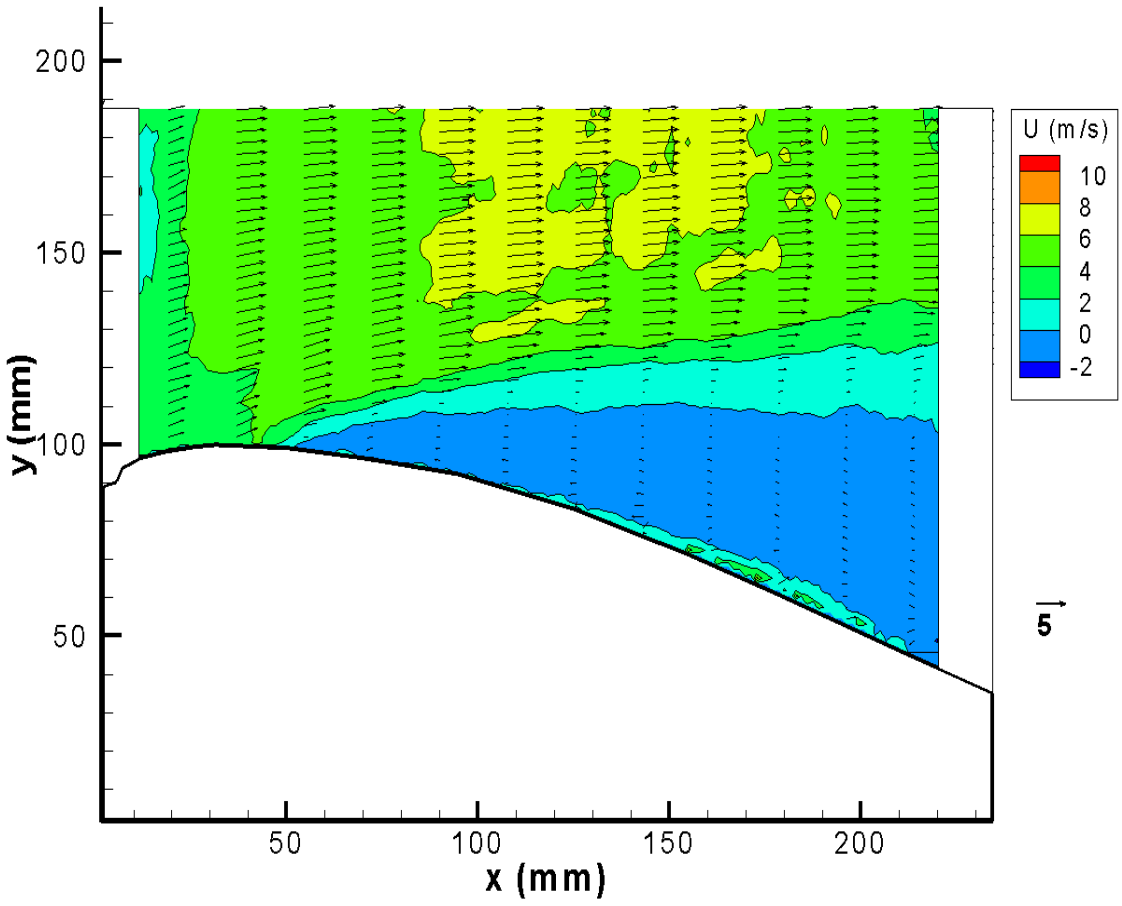

Figure 5.11: Flow field without active control at α=18,9°.

Steady Injection - α = 18,9°

Again the steady injection served as a benchmark. Experiments were conducted at three different momentum coefficient levels (see Tab. 5.2). The mean velocity field is depicted in figure 5.12. The V shaped flow arises again and opens the question if that represents a reattachment of the separated flow or if that represents the steady jet separating from the main flow forming this characteristic shape.

It is evident from the frames in the figure 5.12 that the vertex of the "V" lies significantly downstream of the original separation location in opposition to the $\alpha = 17{,}1°$ case, where the vertex of the "V" lies almost at the same position as the original separation point. That explains why the improvement is more significant at $\alpha = 18{,}9°$, if it is assumed that the effective reattachment obtained with the active control extends until the vertex. The attached flow is in fact the one that comes from the leading edge until the vertex, beacause downstream of the vertex the jet is separated from the main flow and does not have a significant effect on the pressure distribution.

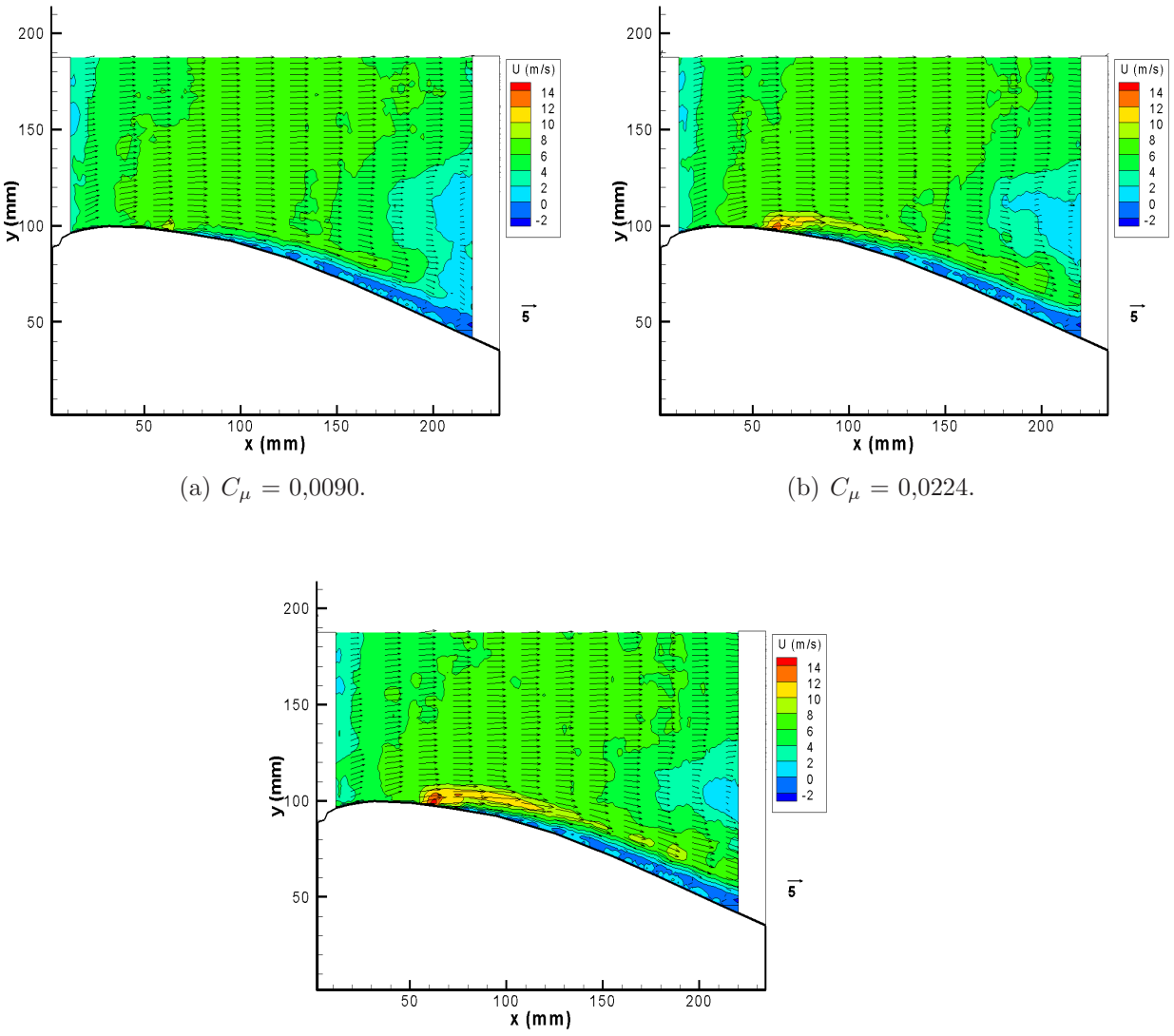

(a) $C_\mu = 0{,}0090$.

(b) $C_\mu = 0{,}0224$.

(c) $C_\mu = 0{,}0360$.

Figure 5.12: Steady injection at α=18,9°.

Unsteady Injection - α = 18,9°

For the following experiments at $\alpha = 18{,}9°$ the actuation system setting was kept the same as for the $\alpha = 17{,}1°$ case. At the lowest actuation frequency used, $f^+ = 1{,}0$, it became evident that the separation is not suppressed during the whole actuation cycle. The strong adverse pressure gradient overcame the added momentum and a strong oscillating flow was observed; the figures 5.13 *c* and *d* show the onset of a massive separation. Once the frequency is augmented to $f^+ = 2{,}5$ the flow around the profile presented an almost steady behavior. However, the attachment extends to a shorter length than when $f^+ = 1{,}0$ is used. At the frequencies $f^+ = 5{,}0$, figure 5.15, the results showed two main features: first, that the V shaped flow is not present as with $f^+ = 1{,}0$ and in a less extent with $f^+ = 2{,}5$. Moreover, the necessary momentum added to keep the boundary-layer attached was lower than those used with all other frequencies. The actuation system operating at $f^+ = 10{,}0$ shows a quasi-steady flow behaviour, while C_μ has to be increased to keep the flow attached (compared with the $f^+ = 5{,}0$ case) and the V shaped flow appears again. It all indicates a preferable dimensionless frequency in the range $f^+ = 5{,}0$ to be adopted.

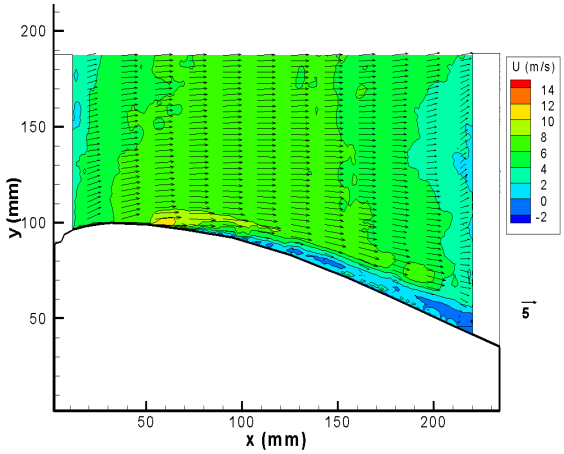

(a) t/T = 0.

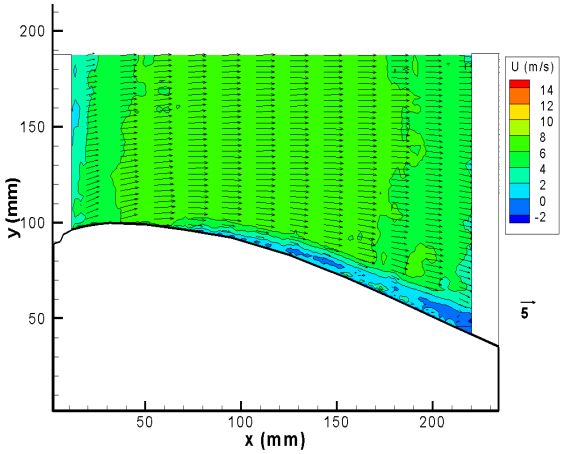

(b) t/T = 0,2.

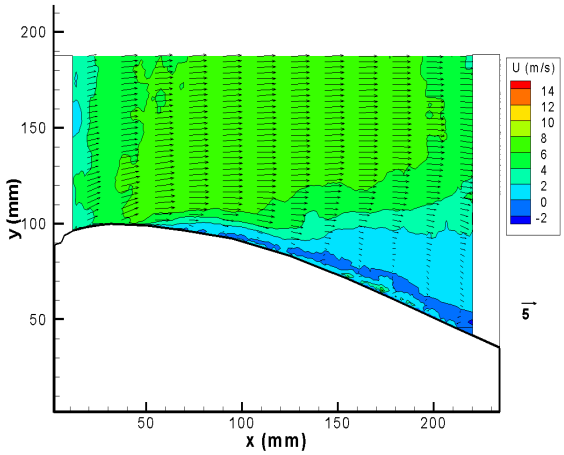

(c) t/T = 0,4.

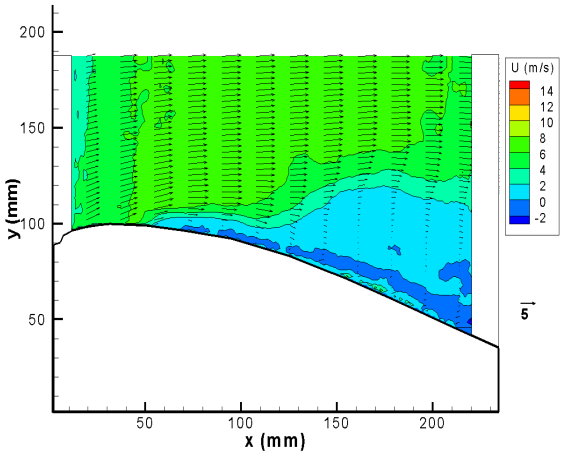

(d) t/T = 0,6.

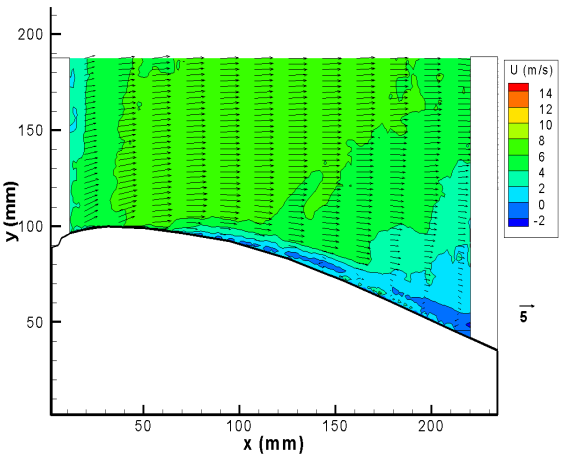

(e) t/T = 0,8.

Figure 5.13: Unsteady injection at α=18,9°, f^+ = 1,0, C_μ = <0,71;0,042>.

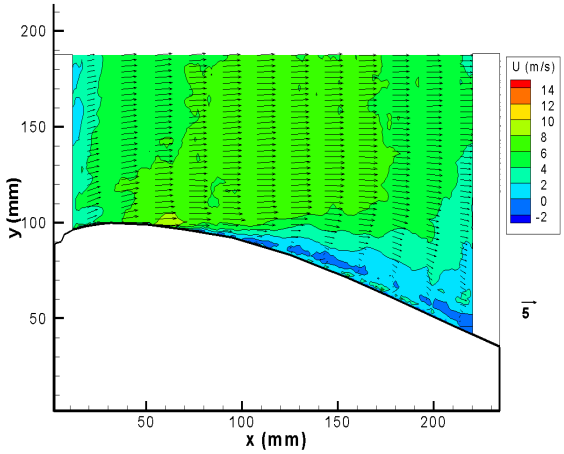

(a) t/T = 0.

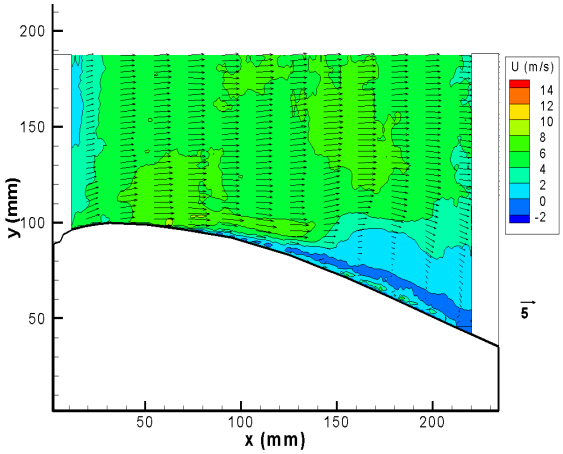

(b) t/T = 0,2.

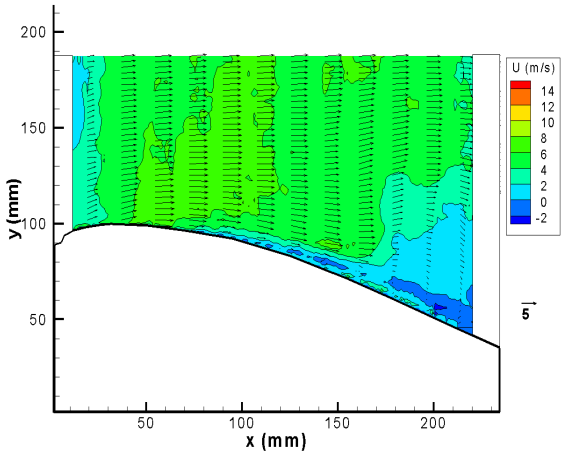

(c) t/T = 0,4.

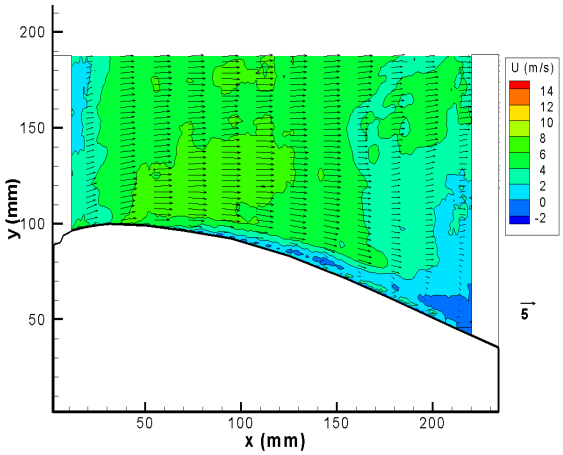

(d) t/T = 0,6.

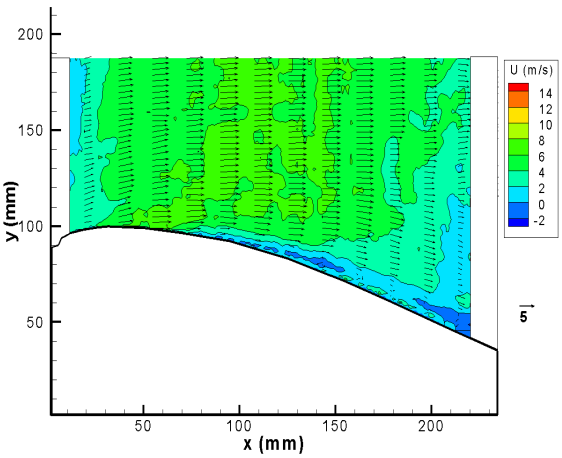

(e) t/T = 0,8.

Figure 5.14: Unsteady injection at α=18,9°, f^+ = 2,5, C_μ = <0,0047;0,020>.

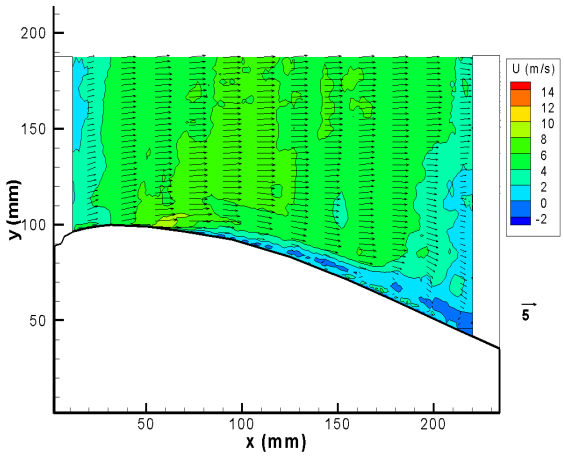

(a) t/T = 0.

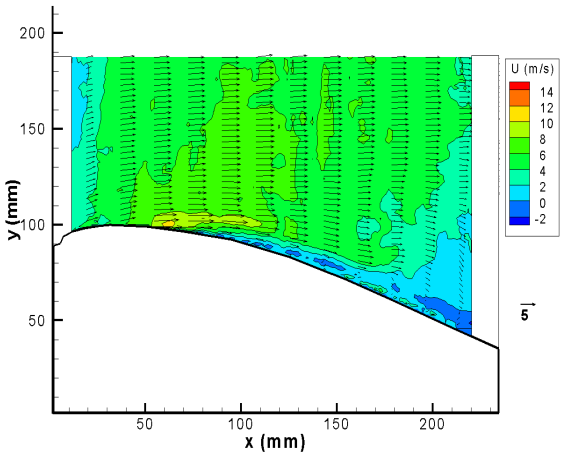

(b) t/T = 0,2.

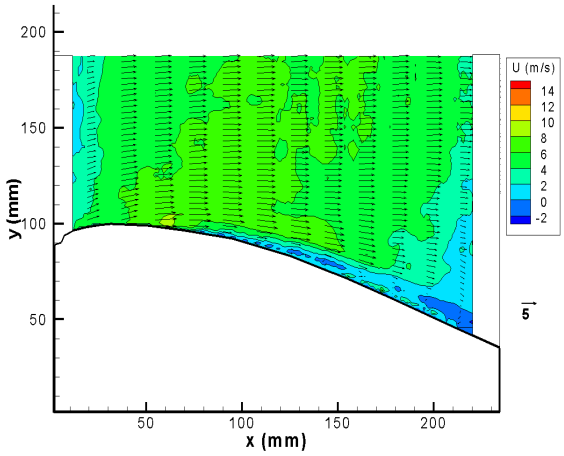

(c) t/T = 0,4.

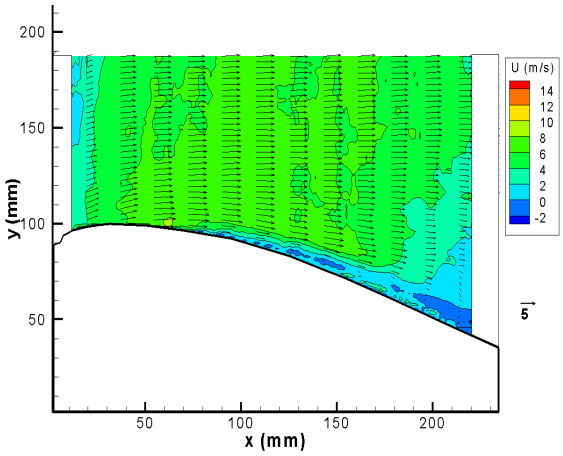

(d) t/T = 0,6.

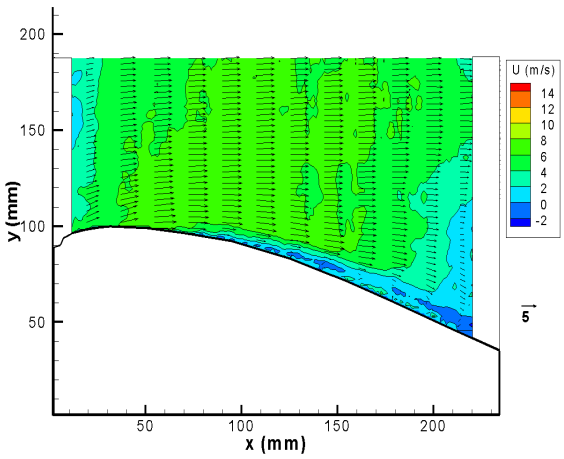

(e) t/T = 0,8.

Figure 5.15: Unsteady injection at α=18,9°, $f^+ = 5{,}0$, C_μ = <0,0027;0,0058>.

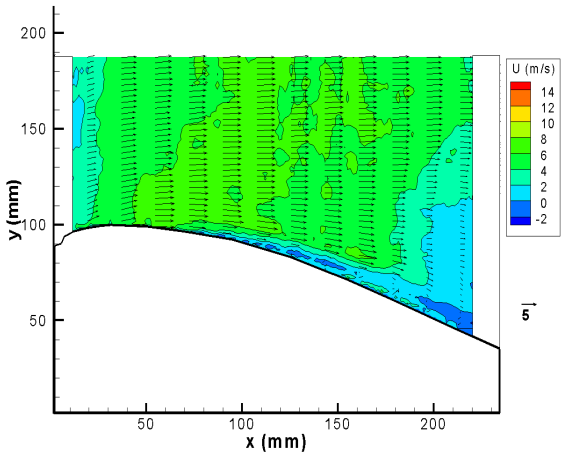

(a) t/T = 0.

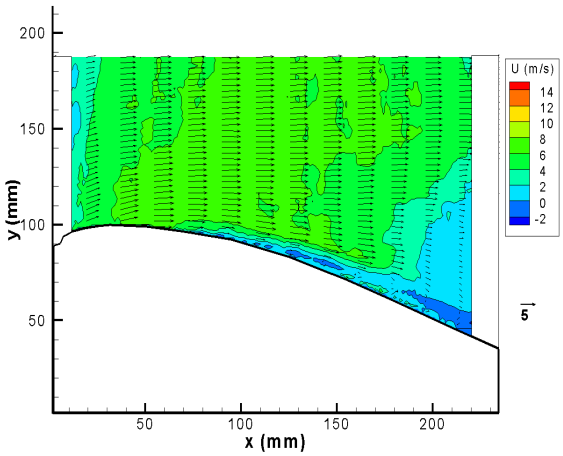

(b) t/T = 0,2.

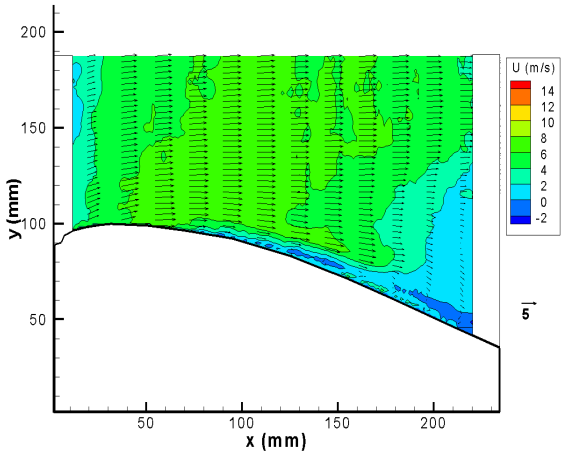

(c) t/T = 0,4.

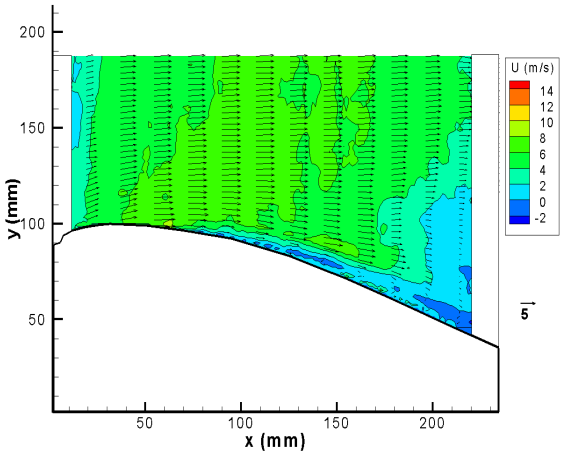

(d) t/T = 0,6.

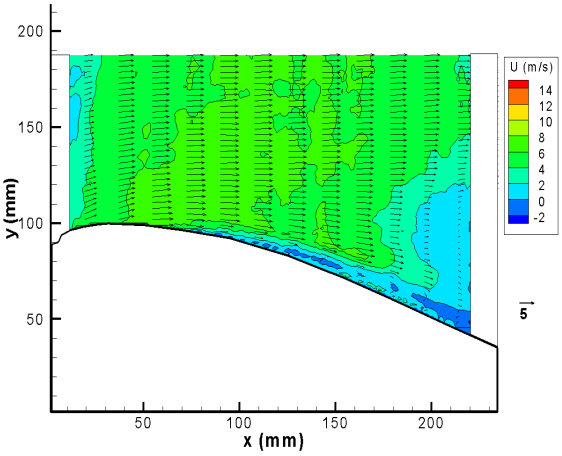

(e) t/T = 0,8.

Figure 5.16: Unsteady injection for α=18,9°, f^+ = 10,0, C_μ = <0,0070;0,0067>.

5.4 Boundary-Layer Measurements - Hot-Wire

Hot-wire anemometry was used to measure the mean velocity profiles and a high temporal resolved instantaneous velocity field within the boundary-layer as well. PIV can not provide information of the flow in this region without the proper caution due to the laser reflexion on the surface, resulting in an excessive number of outliners from cross-correlation algorithm.

This series of measurements was restricted to the case of severe separation at $\alpha = 18{,}9°$, whereas the strongest impact due to the active control is expected. The nondimensional frequency was limited to $f^+ = 0$, 1,0, 2,5 and 5,0 since the performance of active control at $f^+ = 10$ was not satisfactory. A single momentum coefficient C_μ value for each f^+ was used - asserted previously from pressure distribution and PIV measurements, high enough to reattach the boundary-layer (see table 5.3).

Table 5.3: Test cases examined with HW anemometry at $\alpha = 18{,}9°$.

f^+	$< \bar{c}_\mu; c'_\mu >$
0	<0,0090; ->
1,0	<0,0045; 0,042>
2,5	<0,0047; 0,020>
5,0	<0,0050; 0,011>

5.4.1 Time Averaged Velocity

Mean velocity profiles permits to compare non-disturbed boundary layers and those with steady active control as well as with unsteady active control. Furthermore, it permits to assert the vertical extension of the injected jets.

The measurements were taken at eight stations on the suction side, located at 3,8%, 6,5%, 9,2%, 11,9%, 15,1%, 22,4%, 32,4% and 40,8% of the chord length - these positions correspond to the location of the pressure taps 3, 4, 5, 6, 7, 11 and 13, respectively. The

closest point to the surface was located at 0,1 mm from the surface and the smallest steps during the vertical scanning was set to 0,1 mm. No hot-wire correction was applied to account for heat transfer from the wire to the surface, however during calibration the sensor was placed very close to the surface and the output for zero velocity was recorded - it is assumed to be a reasonable compensation for the present case, because the surface material is poor heat transfer material what minimizes the importance of the surface effect over the hot-wire.

Steady Injection

The figure 5.17 compares the mean velocity profiles without active control and with steady injection. At the first measurement station, at 3,8% of the chord, the velocity profile of the normal flow presents a typical separated flow profile. At this point the shear layer lies 2,5 mm above the surface and displaces continuously away from the surface in the downstream direction. The flow within the region formed by the surface and the shear layer has a very low velocity.

Active flow control is also presented (the FC profiles in the figure), here steady injection is presented with a single configuration: $f^+ = 0$ and $C_\mu = <0{,}0090; ->$, which was chosen from the previous experiments with PIV. At the first observation the separation seems to be suppressed in all stations measured. However, the FC profile at 3,8% shows a "nose" shape, which is a clear indication of the true direction of the jet. The injection is directed away from the surface but due to viscous effects pulls the low momentum flow below and above it, hence the new mean velocity profiles acquire a rounded shape. As the injected jet travels downstream the added high momentum mass diffuses and the "nose" shape is minimized. From about 15,1% of the chord a double curved velocity profile develops almost vanishing at 40,8% of the chord. That is the "V" noticed with the PIV, caused by the separation of the injected air and the main air stream outside of the boundary-layer.

Unsteady Injection

The following mean velocity profiles were obtained with pulsed injection, for each nondimensional frequency only a single momentum coefficient was adopted - keeping the mean C_μ equivalent. The profiles are plotted together with the mean velocity profiles from the case without flow control. Figure 5.18 presents the case using $f^+ = 1{,}0$. The mean velocity profiles are similar to the steady injection case, what means that the unsteady nature

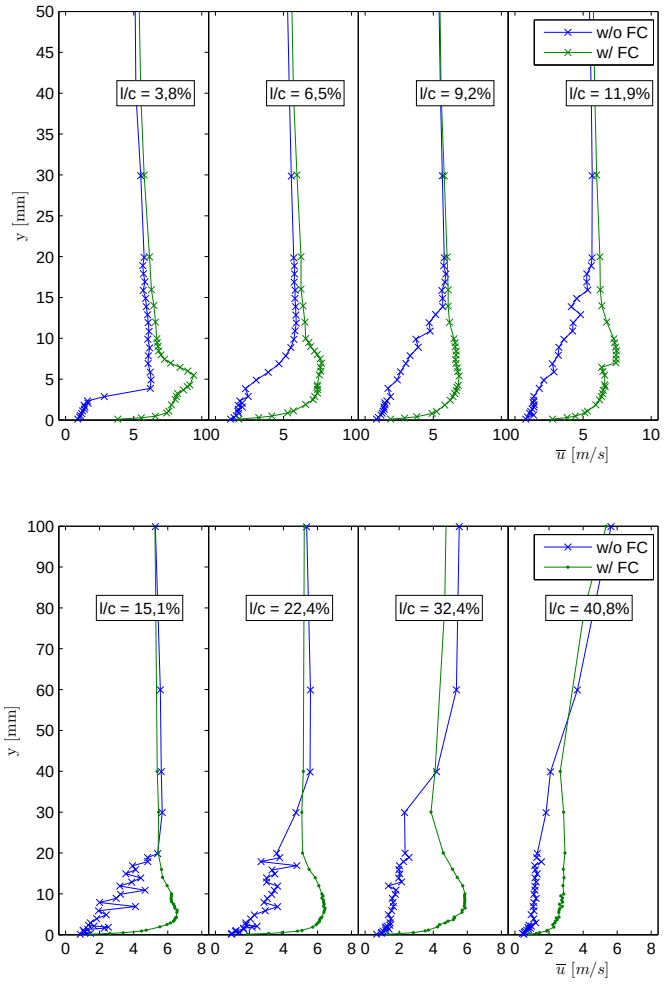

Figure 5.17: $\bar{u}$ profiles at α=18,9°, control at $f^+ = 0$, C_μ = <0,0090; ->.

of this flow is not captured by this measurement.

Observing the sequence of profiles for the higher actuation frequencies, i.e $f^+ = 2{,}5$ and 5, one realizes that the injected jet becomes more diffuse in the boundary-layer as the frequency is increased (figures 5.19 and 5.20). It is interesting because when observing only the PIV results, one could conclude that both steady injection and high frequency actuation feature almost the same flow, while in fact at high frequency the injected flow is much more diffuse. The profiles obtained at $f^+ = 5{,}0$, figure 5.20, present a very smooth shape indicating that the added momentum spread to the main flow. It avoids the break-up between the injected flow and main flow (the V shape found in the PIV measurements), the comparison between $f^+ = 1{,}0$ and $f^+ = 5{,}0$ - figure 5.18 at 32,9% and figure 5.20 at the same position illustrates how the imminent break-up is suppressed.

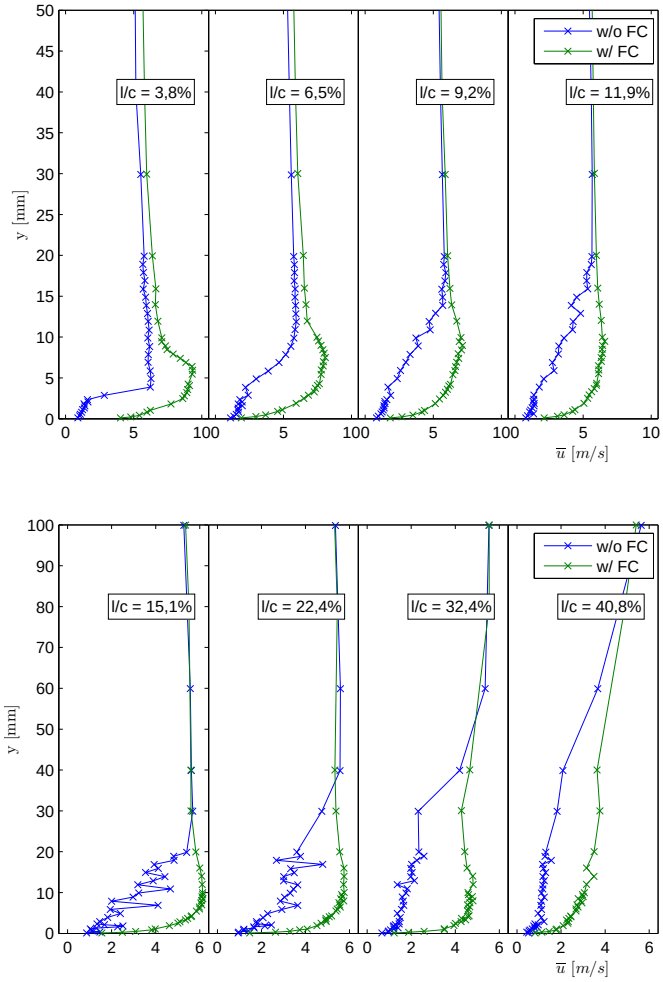

Figure 5.18: $\bar{u}$ profiles at α=18,9°, control at $f^+ = 1{,}0$ and C_μ = <0,0045; 0,042>.

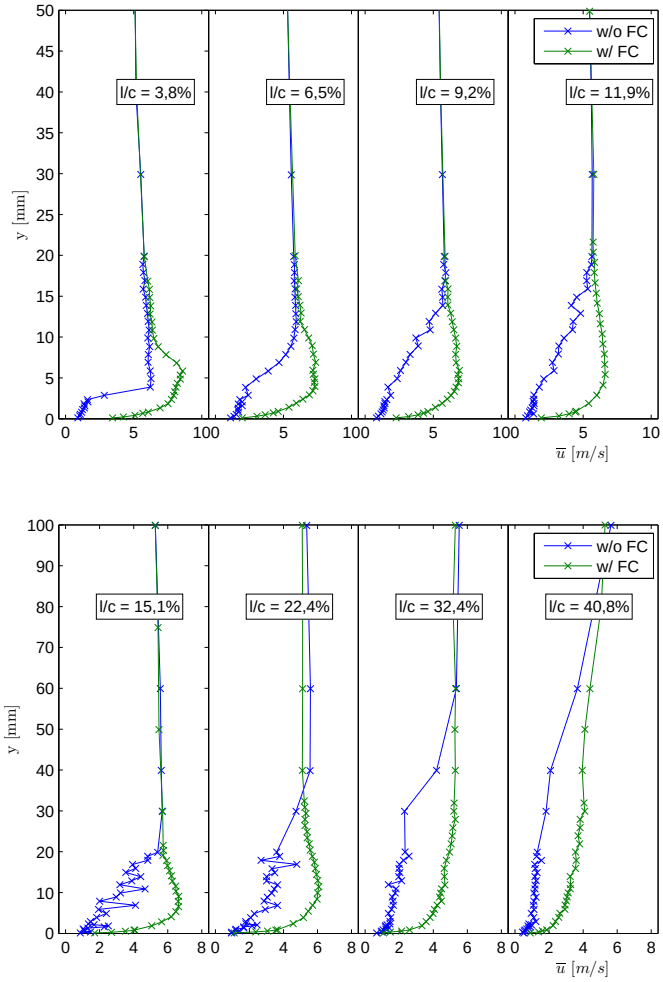

Figure 5.19: $\bar{u}$ profiles at α=18,9°, control at $f^+ = 2{,}5$ and C_μ = <0,0047; 0,020>.

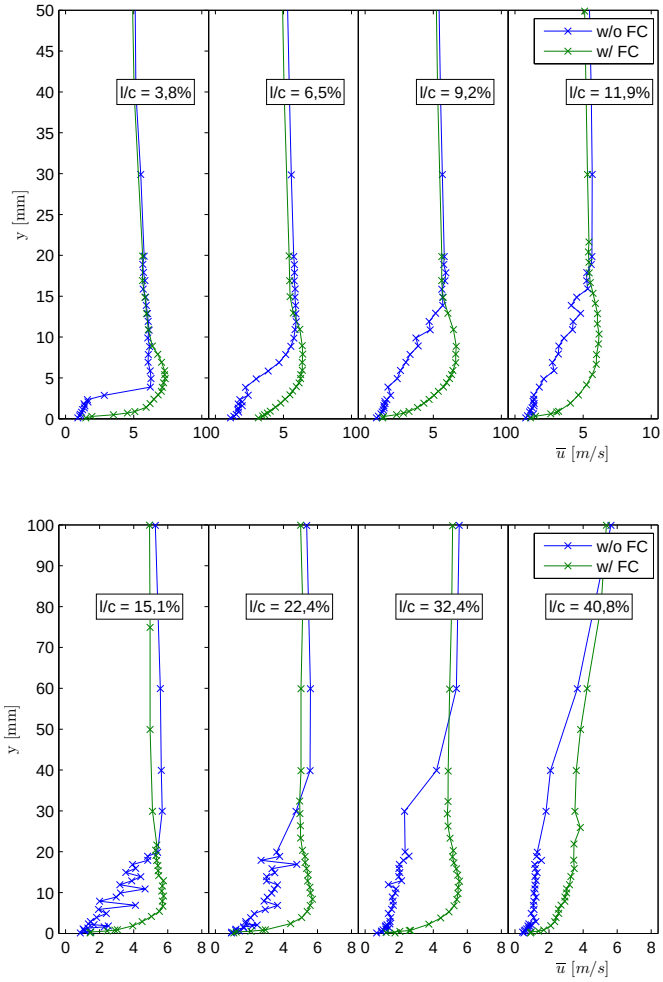

Figure 5.20: $\bar{u}$ profiles at α=18,9°, control at $f^+ = 5{,}0$ and C_μ = <0,0050; 0,011>.

Chapter 6

Conclusion

A boundary-layer active control method was designed, implemented and examined in this work. Its operation principle is to provide extra momentum through a pulsed (unsteady) air jet to the boundary-layer. Three considerations were taken into account during the design phase: which type of air passage should be used, where is the most apropriate location for the air injection and last, what are the most efficient frequency and amplitude ranges that the unsteady jet should operate in order to find its most effective operating point.

The design of the actuator started considering previous works [7, 22] and was refined using a "mock-up" - a test box that allowed to investigate forms to optimize the flow coming out from the slot. Once the actuation system was complete and installed in a NACA 63_3-018 airfoil, cotton tufts visualisation supported the definition of the ranges of frequency and amplitude that influenced the boundary-layer separation. The actuation system was calibrated to provide information about its behaviour and to garantee that a specific operating point could be reproduced.

Once the range was defined, three measurement methods were employed: static pressure distribution, particle image visualisation and hot-wire anemometry. They complemented each other and they provided an detailed view of what happens with the flow when interacting with the air injections.

The conclusions that can be asserted from the experiments are:

- for low actuation frequencies, i.e. $f^+ = 1{,}0$ and $2{,}5$ unsteady effects are very strong. The boundary-layer reattaches and separates within the actuation cycle;
- for higher frequencies, i.e $f^+ = 10{,}0$, the receptivity to the unsteady jets was similar

to the steady air injection. This is due to the fact that the unsteady component of the air injection is damped as the actuating frequency is increased.

- injection of low momentum flow deteriorates the performance of an aerodynamic body, hence it is necessary to performe a careful investigation before such solution is implemented in a real machine, because it may not only be inefficient but rather detrimental to aerodynamic characteristics.

- excessive amplitude of air injection, i.e. high levels of C_μ results in energy waste. There is an upper limit to the benefits one may acchive by increasing C_μ. Once this limit is reached the flow will separate in a fixed region, causing a "V" shaped flow - it means that the injected air will not be able to stick with the main flow and that the pressure gradient tears the injected from the main flow.

- no preferential frequency of actuation could be detected. The explanation for that is related to the effective mechanism of control resulting from the Active Control System. For the current type of AFC (fluidic type) separation can be affected by three mechanisms: 1) Mixing of high-momentum flow with boundary-layer or with shear layer 2) Energization of boundary-layer and 3)Incitement of boundary-layer/ shear layer transition. From the mean velocity profiles and PIV flow fields, it is recognizable that the boundary-layer was *energized* and that no coherent structure brought momentum to the boundary-layer, what would be the mechanism 1 above. The mechanism 1 requires that the perturbation caused by the injected jets should be directed to the flow, *out of the boundary-layer* in order to interact with coherent structures. The incitement to transition (mechanism 3) should be efficient when a laminar separation occours but in the present case the separation is turbulent as indicated by visualisation. From that we conclude that the only mechanism present, energization of boundary layer, is the less susceptible to the frequency of perturbation and hence no favorable frequency could be identified. From this conclusion we assert that most appropriated frequency will be closely related to the application of the AFC and less to the receptivity of the boundary-layer. If it will be used in a turbomachinery environment, the frequency should be related to the wake frequency in order to impose a constant calmed region once the pulsating frequency matches that of the wakes.

Suggestions for future works:

- instead of a particular aerodynamic body, a flat geometry should be used in order to eliminate the effect of particular characteristics such as the leading edge;
- to use a flexible wall attached to the inner upper wall of the wind tunnel, its adjustment permits to impose different pressure gradients in the flat plate, which can simulate the boundary-layer of different airfoils and blades;
- in a flat plate one can easily place the slot in different positions to perform a comprehensive study of the influence of the slot position on the separation control;
- measurement technics and body modifications also profit from flated surface shape. Hot-wires and Laser beams can be easier referenced to a flat surface than to a curved one. A flat plate also permits to easily change the position of the actuator;
- an actuation system should be designed to keep the ratio of c'_μ/c_μ constant. Only in this way one can be sure that the frequency is playing a role and not the ratio between those components.
- in the wind tunnel of TU-Darmstadt it is possible to couple the AFC in with impingent wakes generated in a rotating "cage". Experiments should be performed to check the possibility to increase the load over blades through the combination of the effects;
- the duty-cycle can be varied: in the literature there is the indication that reduced duty-cycle ($\tau = 0{,}1$) may be as efficient as the current $\tau = 0{,}5$. It opens the possibility to reduce the amount of injected air flow.

Bibliography

[1] Lord, W. K. ; MacMartin, D. G. ; Tillman, T. G.: Flow Control Opportunities in Gas Turbines Engines. In: *Fluids 2000 Conference and Exhibit*. Denver, Colorado, USA, 19–22 June 2000

[2] Riegels, F. W.: *Aerodynamische Profile*. 1°. München : R. Oldenbourg, 1958

[3] Hsiao, F. B. ; Liu, C. F. ; Shyu, J. Y.: Control of Wall-Separated Flow by Internal Acoustic Excitation. In: *AIAA Journal* (1990)

[4] Chang, R. C. ; Hsiao, F. B. ; Shyu, J. Y.: Forcing level effects of internal acoustic excitation on the improvement of airfoil performance. In: *Journal of Aircraft* 29 (1992), Sept.–Oct., Nr. 5, S. 823–829

[5] Smith, D. R. ; Amitay, M. ; Kibens, V. ; Parakh, D. ; Glezer, A.: Modification of Lifting Body Aerodynamics using Synthetic Jet Actuators. In: *AIAA 98-0209* (1998)

[6] McCormick, D. C.: Boundary Layer Separation Control with Directed Synthetic Jets. In: *38th Aerospace Sciences Meeting and Exhibit* AIAA, 2000

[7] Wang, Z.: *Numerical Analysis of Massive Separation Control on Turbomachine Blades Using Synthetic Jet*, Technische Universität Darmstadt, Diss., 2003

[8] Volino, R. J.: Separation Control on Low-Pressure Turbine Airfoils Using Synthetic Vortex Generator Jets. In: *Journal of Turbomachinery* 125 (2003), January, S. 765–777

[9] P. Bons, Jeffrey ; Sondergaard, Rolf ; B. Rivir, Richard: Turbine Separation Control Using Pulsed Vortex Generator Jets. In: *Journal of Turbomachinery* 123 (2001), April, S. 198–206

[10] P. Bons, Jeffrey ; Sondergaard, Rolf ; B. Rivir, Richard: The Fluid Dynamics of LPT Blade Separation Control using Synthetic Jets. In: *Journal of Turbomachinery* 124 (2002), January, S. 77–85

[11] Culley, Dennis E. ; Bright, Michelle M. ; Prasht, Patricia S. ; Strazisar, Anthony J.: Active Flow Separation Control of a Stator Vane Using Embedded Injection in a Multistage Compressor Experiment. In: *Journal of Turbomachinery* 126 (2004), January, S. 24–34

[12] Culley, Dennis E. ; Braunscheidel, Edward P. ; Bright, Michelle M.: Impulsive Injection for Compressor Stator Separation Control / NASA. 2005. – Forschungsbericht. – Prepared for the 41th Joint Propulsion Conference and Exhibit

[13] McAuliffe, Brian R. ; Sjolander, Steen A.: Active Flow Control Using Steady Blowing for a Low-Pressure Turbine Cascade. In: *Journal of Turbomachinery* 126 (2004), October, S. 560–569

[14] Hsiao, F-B ; Liu, C-F. ; Tang, Z.: Aerodynamic Performance and Flow Structure Studies of a Low Reynolds Number Airfoil. In: *AIAA Journal* 27 (1989), February, Nr. 2, S. 129–137

[15] Bar-Sever, A.: Separation Control on an Airfoil by Periodic Forcing. In: *AIAA Journal* 27 (1989), June, Nr. 6, S. 820–821

[16] Seifert, A. ; Bachar, T. ; I., Wygnanski ; Koss, D. ; Shepshelovich, M.: Oscillatory Blowing: A Tool to Delay Boundary Layer Separation. In: *AIAA Journal* 31 (1993), Sept.–Oct., Nr. 11, S. 2052–2060

[17] Culley, Dennis E. ; Prahst, Patricia S. ; Strazisar, Anthony J.: Active Flow Separation Control of a Stator Vane Using Surface Injection in a Multistage Compressor Experiment / NASA. 2003. – Forschungsbericht. – NASA/TM—2003-212356

[18] Xin-qian, Z. ; Xiao-bo, Z. ; Sheng, Z.: Investigation on a Type of Flow Control to Weaken Unsteady Separated Flows by Unsteady Separated Flows by Unsteady Excitation in Axial Flow Compressors. In: *Journal of Turbomachinery* 127 (2005), July, S. 489–497

[19] Yarusevysch, S. ; Sullivan, P. E. ; Kawall, J. G.: Airfoil Boundary Layer Separation and Control at Low Reynolds Number. In: *Experiments in Fluids* 38 (2005), S. 545–547

[20] Ortmanns, J. ; Kähler, C. J.: Investigation of Pulsed Actuators for Active Flow Control Using Phase Locked Stereoscopic Particle Image Velocimetry. In: *12th International Symposium - Applications of Laser Techniques in Fluid Mechanics*. Lisbon, Portugal, 12–15 July 2004

[21] King, R. (Hrsg.): *Active Flow Control*. 1. Edition. Springer Verlag, 2007

[22] Werden, S.: *Grenzschichtverhalten am Kreiszylinder bei instationärer aktiver Anregung durch Wandöffunungen*, Technische Hochschule Darmstadt, Diss., 1998

[23] White, F.: *Viscous Flow*. Second Edition. McGraw Hill, Inc, 1974

[24] Chang, P. K.: *Separation of Flow*. Bd. 1. New York : Pergamon Press, 1970

[25] Brendel, M. ; Mueller, T. J.: Boundary Layer Measurements on an Airfoil at a Low Reynolds Number in an Oscillating Freestream. In: *AIAA Journal* 26 (1988), March, Nr. 3, S. 257–263

[26] S., Schmidt G. ; Mueller, T. J.: Analysis of Low Reynolds Number Separation Bubble Using Semiempirical Methods. In: *AIAA Journal* 27 (1989), August, Nr. 8, S. 993–1001

[27] Hak, M. Gad-el: *Flow Control: Passive, Active, and Reactive Flow Management*. First Edition. Cambridge University Press, 2000

[28] Horton, H. P.: A Semi-Empirical Theory for the Growth and Bursting of Laminar Separation Bubbles. 1967. – Forschungsbericht. – ARC CP 1073

[29] Redford, J. A. ; Johnson, M. W.: Predicting Transitional Separation Bubbles. In: *Journal of Turbomachinery* 127 (2005), July, S. 497–501

[30] Simpson, R. L.: REVIEW - A Review of Some Phenomena in Turbulent Flow Separation. In: *Journal of Fluids Engineerung* 103 (1981), December, S. 520–533

[31] Simpson, R. L. ; Chew, Y.-T. ; Shivaprasad, B.G.: The Structure of a Separating Turbunlent Boundary Layer. Part 1. Mean Flow and Reynolds Stresses. In: *Journal of Fluid Mechanics* 113 (1981), S. 23–51

[32] Simpson, R. L. ; Chew, Y.-T. ; Shivaprasad, B.G.: The Structure of a Separating Turbunlent Boundary Layer. Part 2. Higher-order Turbulence Results. In: *Journal of Fluid Mechanics* 113 (1981), S. 53–73

[33] Simpson, R. L.: Aspects of Turbulent Boundary-Layer Separation. In: *Prog. Aerospace Sci.* 32 (1996), S. 457–521

[34] Kline, S. J. ; Bardina, J. G. ; Strawn, R. C.: Correlation of the Detachment of Two-Dimensional Turbulent Boundary Layers. In: *AIAA Journal* 21 (1983), S. 68–73

[35] Castillo, L. ; Xia, W. ; George, W. K.: Separation Criterion for Turbulent Boundary Layers Via Similarity Analysis. In: *Journal of Fluids Engineering* 126 (2004), May, S. 297–304

[36] Houtermans, R. ; Coton, T. ; Arts, T.: Aerodynamic Performance of a Very High Lift Low Pressure Turbine Blade with Emphasis on Separation Prediction. In: *Journal of Turbomachinery* 126 (2004), July, S. 406–413

[37] McCullough, G. B. ; Gault, D. E.: Examples of Three Representative Types of Airfoil-Section Stall at Low Speed / NACA. 1951. – Forschungsbericht. – Technical Note 2502

[38] Fernholz, H. H.: Management and Control of Turbulent Shear Flows. In: *ZAMM - Journal of Applied Mathematics and Mechanics* 73 (1992), November, Nr. 11, S. 287–294

[39] D., Taylor H.: Design Criteria for and Applications of the Vortex Generator Mixing Principle / United Aircraft Department. 1948. – Forschungsbericht. – Research Department Concluding Report No. M-15038-1

[40] H., Pearcey H. ; V., Lachmann G. (Hrsg.): *Shock Induced Separation and Its Prevention by Design and Boundary Layer Control*. Bd. 2. Oxford, Great Britain : Pergamon Press, 1958

[41] Grundmann, S. ; Tropea, C.: Experimental Transition Delay Using Glow-discharge Plasma Actuators. In: *Experiments in Fluids* 42 (2007), February, S. 653–657

[42] Seifert, A. ; Greenblatt, D. ; Wygnanski, I. J.: Active separation Control: an overview of Reynolds and Mach Numbers Effects. In: *Aerospace Science and Technology* 8 (2004), S. 569–582

[43] Greenblatt, D. ; Wygnanski, I. J.: The Control of Separation by Periodic Excitation. In: *Progress in Aerospace Sciences* 36 (2000), S. 487–545

[44] Schröder, T.: *Entwicklung des instationären Nachlaufs hinter quer zur Strömungsrichtung bewegten Zylindern und dessen Einfluß auf das Umschlagverhalten von ebenen Grenzschichten stromabwärts angeordneter Versuchskörper*, Technische Hochschule Darmstadt, Diss., 1985

[45] Pfeil, H. ; Orth, U.: Boundary-Layer Transition on a Cylinder with and without Separation Bubbles. In: *Experiments in Fluids* 10 (1990), S. 23–32

[46] Orth, U.: *Untersuchung des Umschlagevorganges von Platten- und Zylindergrenzschichten bei ungestörter und stationär oder periodisch gestörter Zuströmung*, Technische Hochschule Darmstadt, Diss., 1991

[47] Bruun, H. H.: *How-Wire Anemometry: Pinciples and Signal Analysis*. First Edition. Oxford University Press, 1995

[48] Gibbings, J. C. ; Madadnia, J. ; Yousif, A. H.: The Wall Correction of the Hot-Wire Anemometer. In: *Flow Measurement Instrumentation* 6 (1995), Nr. 2, S. 127–136

[49] Nitsche, W. ; Brunn, A.: *Strömungsmesstechnik*. 2. Auflage. Springer Verlag, 2005

[50] Jensen, K. D.: Flow Measurements. In: *Journal of the Brazilian Society of Mechanical Sciences and Engineering* 26 (2004), October-December, S. 400–419

[51] Pope, A.: *Wind-Tunnel Testing*. Second Edition. John Wiley & Sons, Inc, 1950

[52] Doebelin, E. O.: *Measurement Systems - Application and Design*. Second Edition. McGraw Hill, Inc, 1982

[53] Stern, F. ; Muste, M. ; Beninati, M.-L. ; Eichinger, W. E.: Summary of Experimental Uncertainty Assessment Methodology with Exemple / University of Iowa, USA. 1999. – Forschungsbericht. – IIHR Technical Report No. 406

[54] Kline, S. J. ; McClintock, F. A.: Describing Uncertainties in Single-Sample Experiments. In: *Mechanical Engineering* 75 (1953), S. 3–8

[55] König, S.: *Untersuchung des Einflusses überlagerter Stator- und Rotornachläufe auf den Clocking-Effekt an einer 1.5-stufigen axialen Gasturbine*, Technische Universität Darmstadt, Diss., 2006

[56] Schreiber, H.-A. ; Steinert, W. ; Küsters, B.: Effects of Reynolds Number and Free-Stream Turbulence on Boundary Layer Transition in a Compressor Cascade. In: *Journal of Turbomachinery* 124 (2002), January, S. 1–9

[57] Howell, R. J. ; Ramesh, O. N. ; Hodson, H. P. ; Harvey, N. W. ; Schulte, V.: High Lift and Aft-Loaded Profiles. In: *Journal of Turbomachinery* 123 (2001), April, S. 181–188

[58] Schulte, V. ; Hodson, H. P.: Prediction of the Becalmed Region for LP Turbine Profile Design. In: *Journal of Turbomachinery* 120 (1998), October, S. 839–846

Curriculum Vitae

09.09.1976	Born in São Paulo, Brazil
Dezember 1994	Conclusion of High School at Pueri Domus, São Paulo
Januar - Dezember 1995	Preparatory Course at Anglo, São Paulo
Januar 1996 - Dezember 2001	Study of Mechanical Engineering at Escola de Engenharia Mauá, São Caetano do Sul
Februar 2002 - April 2004	Master of Science at Instituto Tecnológico de Aeronáutica, São José dos Campos
October 2004 - March 2005	German Language Course at Goethe Institut, Mannheim
April 2005 - March 2008	Doktorand at Technische Universität Darmstadt
Since April 2008	Employee at Petrobras S.A., Brazil